



IEEE

November, 2010 Vol. 1

IEEE CASCOM POSTGRADUATE STUDENT PAPER CONFERENCE 2010

PROCEEDINGS
IEEE CASCOM PGSPC 2010



**IEEE CIRCUITS AND
SYSTEMS SOCIETY**
Calcutta Chapter



**IEEE
COMMUNICATIONS
SOCIETY**
Calcutta Chapter



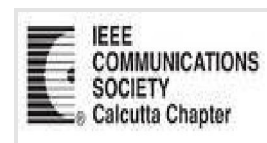
**IEEE CASCOM
POST GRADUATE STUDENT PAPER CONFERENCE 2010
Nov. 27, 2010**

Jadavpur University
Kolkata – 700 032. India.

PROCEEDINGS
IEEE CASCOM PGSPC 2010, Vol. 1

<http://ewh.ieee.org/r10/calcutta/cas/>
<http://ewh.ieee.org/r10/calcutta/comsoc/>

Jointly Organized by:



Editors:

P. Venkateswaran

Secretary, IEEE CAS Calcutta Chapter

Dr. Swarup Mandal

Chairman, IEEE ComSoc Calcutta Chapter

Prof. Rabindranath Nandi

Chairman, IEEE CAS Calcutta Chapter

CONTENTS

Page #

Track: Communication Engineering

1. **Generation and Performance Analysis of a New Type of Orthogonal Gold Code in CDMA System** - *A. Chandra and S. Chattopadhyay* 1
2. **Error Probability of Alamouti Coded MIMO Systems with Multibranch Switch-and-Examine Combining** - *G. Maiti and A. Chandra* 5
3. **Analysis of Multidimensional-TCM Based MB-OFDM UWB System with Pilot-Aided Channel Estimation for High-Rate IEEE 802.15.3a WPANs** - *M. K. Chowdhury and C. Bose* 9
4. **Performance Analysis of WiMAX PHY** - *S.M. Lalan Chowdhury and P. Venkateswaran* 13
5. **Effectiveness Of Vocal Tract Information For Automatic Speaker Identification Based On Mel Frequency Cepstral Coefficients** - *K.Mohanty, M.Mohanty and S.K.Sanyal* 17
6. **Propagation Characteristics of FSO Link Using Partially Coherent Gaussian Optical Beam** - *S. M. Kale and A. Kar* 21
7. **An Optimized Sensor Node Deployment Scheme for WSN based Flood-Forecasting Systems** - *R. Jana, S. K. Mitra, S. Maity, A. Raha and M. K. Naskar* 25
8. **Comparative Study of Discrete radio model and First order radio model for data gathering in Wireless Sensor Network** - *S. K. Mitra, J. Banerjee and M. K. Naskar* 30

Track: Microwave Engineering

9. **MLSAR Analysis in a Realistic Grounded Human Head Model for a Dipole Antenna using FDTD method at 930 MHz** - *M. F. Ali, S. Mondal and S. Ray* 34
10. **A Brief Review of Energy Absorption in the Human Body and its Effects** - *S. Dhar, A. Das and S. Das* 38
11. **Design of Lowpass Filter using Defected Microstrip Structure (DMS)** - *T. Moyra, L. Murmu, S. Das and S. K. Parui* 43
12. **Performance Studies of Microstrip Patch Antenna with EBG Structure at the Ground Plane** - *C. K. Ghosh, S. Datta, A. Mitra and S. K. Parui* 46
13. **Design and Development of a Wearable Antenna for HiperLAN/2 Applications** - *S. Sankaralingam and S. Dhar* 49
14. **Design and Development of Microstrip Directional Coupler** – *B. C. Mandi* 54

Track: Computer Science and Engineering

15. **Text Extraction and Segmentation from Multiskewed Business Card Images for Mobile Devices** - *A. F. Mollah, S. Basu and M. Nasipuri* 57
16. **Image Secret Sharing Scheme Using a Novel Secret Sharing Technique with Steganography** - *P. K. Naskar, A. Chaudhuri and Atal Chaudhuri* 62
17. **Authorship Identification Using Stylometry Analysis: A CRF Based Approach** – *T. Chakraborty and S. Bandyopadhyay* 66
18. **Analysis of Data Retrieval Time for Filter-based Data Fusion Management Scheme** - *B. Bhattacharya, S. Bhattacharjee and D. D. Majumder* 70

Track: Electron Device

19. **Unified Drain Current Model for Independently Driven Double Gate MOSFETs** – *B. Syamal, C. K. Sarkar, P. Dutta and N. Mohankumar* 74

Generation and Performance Analysis of a New Type of Orthogonal Gold Code in CDMA System

Abhijit Chandra

Department of Electronics & Telecommunication
Engineering
Bengal Engineering & Science University, Shibpur
Howrah, India
abhijit922@yahoo.co.in

Sudipta Chattopadhyay

Department of Electronics & Telecommunication
Engineering
Jadavpur University
Kolkata, India
sudiptachat@yahoo.com

Abstract— Code Division Multiple Access (CDMA) technique has been the most recent advancement in the field of modern wireless communication system. The performance of any CDMA system is largely determined by the choice of the spreading codes which are used as a signature code for the users in such a system. However, depending upon the system requirement, the selection of spreading code has been the most important task on which a proper attention is required by the spreading code designer. In this paper, a new type of orthogonal spreading code suitable for use in a CDMA system has been proposed. The proposed code of a particular length can serve a significantly large number of users in a multi-user CDMA environment as compared to the existing orthogonal codes of similar length. The algorithm for the generation of the proposed code has been developed and presented in this paper. Finally, the proposed code has been used as a spreading code in a multi-user CDMA system. The resulting Bit Error Rate (BER) performance of the proposed code has been depicted graphically for different values of Signal to Noise Ratio (SNR). The corresponding BER performance of two other existing orthogonal codes, namely Walsh and Orthogonal Gold code has also been presented for the purpose of comparison.

Keywords-BER; CDMA; Orthogonal Gold code;SNR; Walsh code.

I. INTRODUCTION

Walsh code has been the most popularly used orthogonal spreading code in a synchronous or downlink CDMA system, where the communication is maintained from the base station to the mobile user only [1]-[4]. As the members of the Walsh code family are mutually orthogonal to each other, this type of code is particularly suitable for use in a forward or synchronous CDMA environment. However, the performance of Walsh code has been found to be quite inferior to that of non-orthogonal Gold code in case of uplink multi-user environment, where the transmitted signal propagates from each individual user and combines asynchronously at the base station [5].

A new set of Walsh-like non-linear phase binary orthogonal user code for asynchronous and synchronous

multi-user spread spectrum communications has been proposed in [6]. It has been observed that the proposed binary user code family outperforms the Walsh code significantly and its performance closely matches with that of near orthogonal Gold code in case of asynchronous communication in Additive White Gaussian Noise (AWGN) channel. It has also been indicated that the performance of all the binary codes are comparable to each other under Rayleigh flat fading channel.

A novel systematic method of generating orthogonal sets of sequences with good correlation properties has been described in [7]. This method is capable of generating $N \times (N-1)$ number of distinct code sequence, each of length N . The zero-shift peak cross-correlation value between any two distinct code members has been calculated and presented for different set size. The maximum cross-correlation value tends to improve for set size 32 and above as the value becomes less than half the sequence length.

Small set Kasami sequence has been utilized in order to generate a new family of orthogonal code sets that can be employed as a spreading sequence in a DS-SS-CDMA communication system [8]. SIMULINK based downlink CDMA system model has been employed to study the BER performance of the generated code and that of the existing orthogonal codes under different channel and user conditions. The performance of the proposed code has been found to be satisfactory as compared to the other codes under those circumstances.

In this paper, a new type of orthogonal spreading code has been generated by using pseudo-noise sequence as the basic sequence. The corresponding code generation algorithm has been developed in MATLAB 7.0 and presented by means of one flow-chart. One comparative study on the characteristics of various orthogonal spreading codes, including the existing ones and the proposed code, has been summarized in a tabular form. The proposed code has been exploited as a signature code in a SIMULINK based downlink CDMA model and the corresponding BER values of such a system have been plotted under different channel conditions. The resultant BER values for two other existing orthogonal codes, namely Walsh and

Orthogonal Gold code, have also been presented for the purpose of comparison.

II. OVERVIEW OF EXISTING ORTHOGONAL SPREADING CODES

A. Walsh code

Practical synchronous CDMA system normally employs orthogonal Walsh code as a signature code since all of its members are purely orthogonal to each other. It is the most popular binary code because of its ease of implementation and simplicity [4]. This type of spreading code is generated by means of an algorithm, known as Walsh-Hadamard transform. The individual codes are identified as the rows of a matrix, known as Walsh-Hadamard matrix, provided by the transform. The algorithm is capable of producing Walsh code of any length $N=2^R$, for any integer R. Another attractive feature associated with this algorithm is that it always follows a recursive rule. Thus it is very easy to construct a code member of higher length from its counterpart of lower length. This can be depicted mathematically as follows [4]:

$$W_{2N} = \begin{bmatrix} W_N & W_N \\ W_N & \overline{W_N} \end{bmatrix}$$

$$, \text{ with } W_2 = \begin{bmatrix} 0 & 0 \\ 0 & 1 \end{bmatrix} \text{ and } W_4 = \begin{bmatrix} 0 & 0 & 0 & 0 \\ 0 & 1 & 0 & 1 \\ 0 & 0 & 1 & 1 \\ 0 & 1 & 1 & 0 \end{bmatrix}$$

, where W_{2N} and W_N represent the Walsh-Hadamard matrix of size $2N$ and N respectively and overscore implies the binary complement of corresponding bits in the matrix.

Since Walsh matrix is a square matrix, an N length Walsh code family can provide at most N number of distinct members and thus serve N different users in a practical CDMA system. But in order to support a high capacity system, Walsh code does not seem to be an attractive choice.

B. Orthogonal Gold code

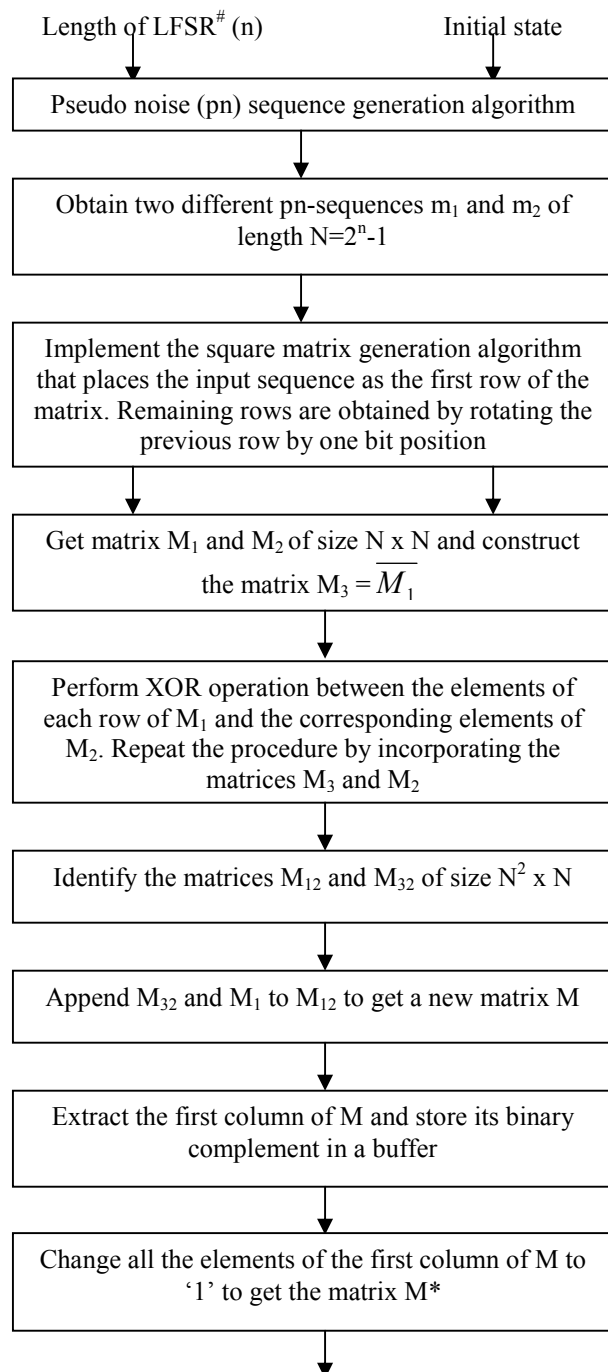
In order to meet the stringent demand of the users in a practical CDMA system, Orthogonal Gold code can be very much effective [7]. It can be generated by means of a very fundamental sequence i.e. pseudo noise (pn) sequence. Actually, the entire set of Orthogonal Gold code consists of a number of orthogonal code sets. Each of these sets comprises as many numbers of orthogonal members as the length of the code. Using any two different pn-sequences of length $(N-1)$, an Orthogonal Gold code set contains altogether $(N-1)$ number of orthogonal code sets, each containing N members of length N . Thus, an Orthogonal Gold code set of length N can provide $N \times (N-1)$ number of distinct code members, divided in $(N-1)$ orthogonal code sets.

Although the members of a particular orthogonal code set are purely orthogonal to each other, the member of one such set may not be orthogonal to another member of some other

set. This leads to non-zero value of cross-correlation amongst the members of Orthogonal Gold code family and consequently leads to a significant BER in a downlink CDMA system. It has been observed that the zero-shift peak cross correlation value amongst the members of this code family of length N has been $2\sqrt{N}$ for N to be a perfect square number.

III. FLOW CHART REPRESENTATION OF THE PROPOSED CODE GENERATION ALGORITHM

The proposed code generation algorithm has been developed by using MATLAB 7.0 and presented by means of one flow-chart, as described next.



Append the buffer contents to the matrix M^* and finally obtain the matrix M_{FINAL} of size $(2N^2+N) \times (N+1)$

Identify each row of the matrix M_{FINAL} as a single code member of the proposed code set

LFSR: Linear Feedback Shift Register

IV. PERFORMANCE ANALYSIS OF THE PROPOSED CODE

A. Performance in regard to characteristics of the code

The CDMA spreading code, proposed in this paper, is an extension of already existing orthogonal spreading code, namely Orthogonal Gold code. The most attractive feature of the proposed code is that it can produce an enormous number of distinct code members of any particular length, as compared to Walsh or Orthogonal Gold code. More specifically, the proposed code set of length $(N+1)$ can offer as many as $(2N^2+N)$ number of distinct members. So in a practical CDMA system, it can support a huge amount of user that would not be possible if Walsh or Orthogonal Gold code is used as a signature code. However, due to the presence of large number of code members, zero-shift peak cross-correlation value for this code family also increases. TABLE I shows a comparative study amongst three orthogonal spreading codes, in terms of the number of distinct code members produced and zero-shift peak cross-correlation value.

TABLE I. CHARACTERISTICS OF DIFFERENT ORTHOGONAL CODES

Type of code	Length of code	Number of distinct members	Absolute value of zero-shift peak cross correlation
Walsh	8	8	0
	16	16	0
	32	32	0
Orthogonal Gold	8	56	4
	16	240	8
	32	992	16
Proposed new type of Orthogonal Gold	8	105	6
	16	465	14
	32	1953	30

As all the members of Walsh code family are mutually orthogonal to each other, the zero-shift peak cross-correlation value for Walsh code has been absolutely zero, irrespective of the length of the code. Orthogonal Gold code set, on the other hand, results non-zero value for zero-shift peak cross-correlation. When the length of the code is less than or equal to 32, this value is half the sequence length as indicated in TABLE I. However, proposed new type of Orthogonal Gold code set yields a higher value of cross-correlation than the other two orthogonal codes.

B. Performance in regard to BER value

Proposed new type of Orthogonal Gold code has been used as a spreading code in a SIMULINK based multi-user downlink CDMA system model and the resulting BER values have been plotted for different values of channel SNR. The corresponding error performances of Walsh and Orthogonal Gold code have also been calculated for the purpose of comparison. Fig. 1 and Fig. 2 display the BER performances of 16-length Walsh, Orthogonal Gold and the proposed code for synchronous communication in an AWGN channel under four and eight user scenario respectively.

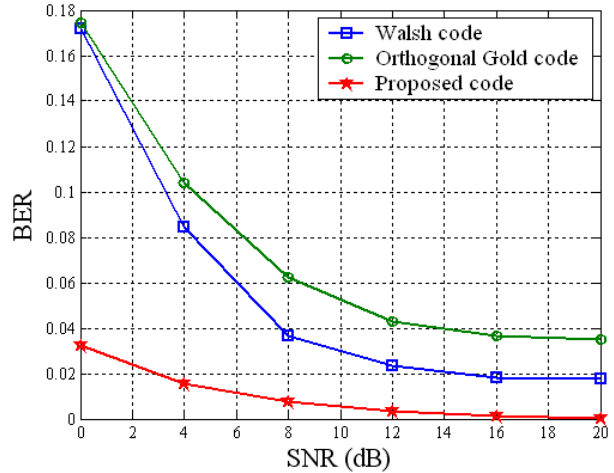


Figure 1. Comparison of BER performances in a downlink CDMA system under four-user scenario in an AWGN channel

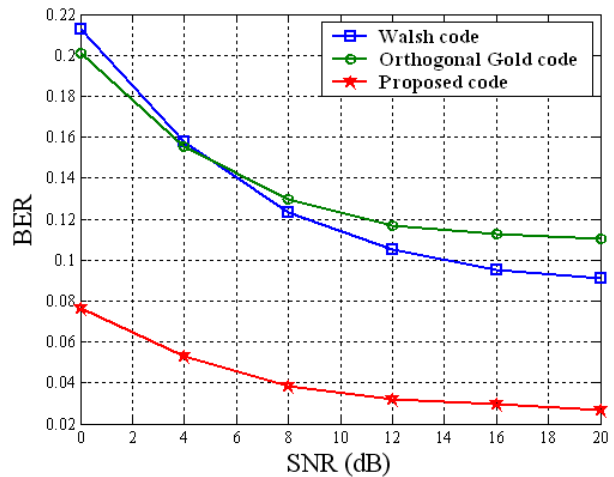


Figure 2. Comparison of BER performance in a downlink CDMA system under eight-user scenario in an AWGN channel

From the BER comparison graphs, one important observation can be made regarding the nature of the proposed new type of Orthogonal Gold code as a spreading code. It can be clearly seen that irrespective of the number of users in a CDMA system, the proposed code outperforms the other two orthogonal codes under every channel conditions. However,

the error performance of Walsh code is superior to that of Orthogonal Gold code almost always.

Even if zero-shift peak cross-correlation value for the proposed code is more than that of other two existing codes, the adverse effect of high cross-correlation has not been reflected in the comparative analysis of BER values. This behaviour can be justified through the detailed analysis of the cross-correlation value amongst different code members of any particular code set. As for example, when the length of the code is 16, the non-zero value of cross-correlation amongst a pair of distinct members of Orthogonal Gold code set can take only three values, more explicitly ± 4 and 8. Thus the minimum non-zero cross-correlation value can be inspected as one-fourth of the code length for Orthogonal Gold code set. However, the proposed code of similar length can provide a minimum non-zero cross-correlation value as small as ± 2 , i.e. one-eighth of its length. When this particular pair of code members is assigned as spreading codes to different users, they will cause less inter-user interference and consequently result in fewer errors in the transmitted bit stream.

V. CONCLUSIONS

The selection of the spreading code in a CDMA system has been going to be very crucial task for the spreading code designers. Whenever any attempt is made to enhance the number of codes in order to support a high capacity CDMA system, this will have the undesirable effect of higher cross-correlation value between the code members. So, the code designers are in search of some new type of spreading code that can serve both the purpose of capacity and efficiency of spread spectrum system simultaneously. This paper presents one algorithm for the generation of a new type of orthogonal code set which is capable to offer a significantly large number of codes in comparison to other existing orthogonal codes.

Moreover, the BER performance of the proposed code looks very much affirmative irrespective of the channel and user conditions. It can be thought of as a promising solution for the future CDMA networks.

ACKNOWLEDGMENT

The authors would like to place their sincere thanks to Prof. S.K. Sanyal, Professor, Department of Electronics & Telecommunication Engineering, Jadavpur University, for his technical support and constant motivation. This work could not be completed without his continuous encouragement.

REFERENCES

- [1] J. L. Walsh, "A closed set of normal orthogonal functions", *Amer. J. Math.*, vol. 55, pp. 5–24, 1923.
- [2] T.K. Woo, "Orthogonal code design for quasi-synchronous CDMA", *Electronics Letters*, vol. 36, no. 19, pp. 1632-1633, September 2000.
- [3] S. Ulukus and R. Yates, "Iterative construction of optimum signature sequence sets in synchronous CDMA systems," *IEEE Trans. Inf. Theory*, vol. 47, no. 5, pp. 1989–1998, Jul. 2001.
- [4] E. H. Dinan and B. Jabbari, "Spreading codes for direct sequence CDMA and wideband CDMA cellular networks", *IEEE Communication Magazine*, vol. 36, no. 9, pp. 48-54, September 1998.
- [5] R. Poluri and A. N. Akansu, "Short length CDMA codes for wireless sensor networks", *IEEE Sarnoff Symposium*, 2007.
- [6] A.N. Akansu and R. Poluri, "Walsh-like nonlinear phase orthogonal codes for direct sequence CDMA communications", *IEEE Trans. Signal Processing*, vol. 55, no.7, pp. 3800-3806, July 2007.
- [7] H. Donelan and T.O' Farrell, "Methods for generating sets of orthogonal sequences", *Electronics Letters*, vol. 35, no. 18, pp. 1537-1538, September 1999.
- [8] A. Chandra and S. Chattopadhyay, "Small set orthogonal Kasami codes for CDMA system", in *Proc. Computers and Devices for Communication (CODEC-2009)*, Kolkata, December 2009.

Error Probability of Alamouti Coded MIMO Systems with Multibranch Switch-and-Examine Combining

Gourab Maiti and Aniruddha Chandra

Department of Electronics and Communication Engineering
 National Institute of Technology, Durgapur, India
 {gourab_maiti@sify.com, aniruddha.chandra@ieee.org}

Abstract—The closed-form error probability expression for bit error rate (BER) of binary-phase shift keying (BPSK) modulation in Rayleigh fading channel, using Alamouti transmission scheme with multi-branch switch-and-examine combining (SEC), is derived for different numbers of receive antennas (L) and are plotted. The BER plots show that SEC gives better performance than the traditional switch-and-stay combining (SSC).

Keywords—Alamouti code; switched combining; BER; Rayleigh fading; BPSK

I. INTRODUCTION

Multiple-input multiple-output (MIMO) capability has been standardized in major fourth generation (4G) wireless technologies (e.g. WiMax and LTE [1]). For a power and bandwidth constrained random time-varying wireless channel, the MIMO feature is of particular interest as it can provide additional diversity/ multiplexing/ array gain, enhance capacity, and improve error performance. Space time codes (STC) are prevalently used in MIMO systems to realize transmit diversity, while the traditional combining schemes may be used to realize diversity at the receiver. Alamouti coding [2] belongs to the general class of space time block codes (STBC), and is often the preferred choice for its simplicity. The redundancy is applied to space and not in time/frequency, so there is no expansion of bandwidth. Also Alamouti code is linear in the transmitted symbols, i.e. we can expand the code matrix as a linear combination of transmitted symbols and their complex conjugates, which greatly simplifies the analysis and receiver design.

In this paper, we examined BER performance of a MIMO system using 2 transmit (Tx) and L receive (Rx) antennas. To realize diversity at both ends of the channel, Alamouti coding and SEC had been used at the transmitter and receiver respectively. Further, a slow flat Rayleigh fading channel is assumed and BPSK is used for modulating the transmitted symbols over the channel. The analysis presented here is a direct extension of the work done by Li and Beulieu [3] who considered maximal ratio combining (MRC), selection combining (SC), and SSC under similar constraints. Although MRC performance is optimal, from the implementation point of view SC or SSC is better, especially when non-coherent detection is employed. Again, if all the channels are equi-correlated or equally affected, then MRC performs similar to

SC. In SC the receiver needs to monitor all the branches for all the time to select the *best* (in terms of instantaneous signal-to-noise-ratio or SNR) branch and thus requires a dedicated receiver in each branch. Furthermore, the receiver switches frequently in order to find the best branch and thereby introduces undesired switching transients. In SSC these problems are alleviated by switching to a second branch only when the SNR in the current branch falls below a given threshold SNR. However, as only two paths are involved in switching decisions, SSC cannot provide any additional benefit when $L > 2$. In contrast, for SEC, if current path is not of acceptable quality, then switching-examining process is continued until an acceptable path is found or all available diversity paths have been examined [4].

The remainder of this paper is organized as follows. We present the system model under study in Section II and using the model derive the BER for multi-branch SEC in Section III. In Section IV, the derived BER expressions are plotted which show excellent agreement with simulated values. Finally some conclusions are drawn in Section V.

II. SYSTEM DESCRIPTION

The system model with 2 Tx and L Rx antennas is shown in Fig. 1. Let s_1 and s_2 denote the equivalent baseband signals (for BPSK $\{s_1, s_2\}$ are either $+\sqrt{E}$ or $-\sqrt{E}$, where E is the bit energy) corresponding to two successive information bits which are sent using a 2×1 Alamouti code [2]. For a slow fading channel it may be assumed that the channel transfer function remains constant over two consecutive bit intervals, and accordingly the received signals on n th branch in these two intervals can be expressed as

$$r_{1n} = h_{1n}s_1 + h_{2n}s_2 + n_{1n} \quad (1a)$$

$$r_{2n} = -h_{1n}s_2^* + h_{2n}s_1^* + n_{2n} \quad (1b)$$

where $\{s_1^*, s_2^*\}$ are the complex conjugates of $\{s_1, s_2\}$, $h_{mn} = \alpha_{mn} \exp(j\theta_{mn})$; $m \in \{1, 2\}$, $n \in \{1, 2, \dots, L\}$ is the complex channel gain between the m th Tx antenna and the n th Rx antenna with α and θ being the random amplitude and phase variation respectively, and the additive noise n_{mn} is a zero-mean circularly symmetric complex Gaussian random variable (RV) having a variance N_0 .

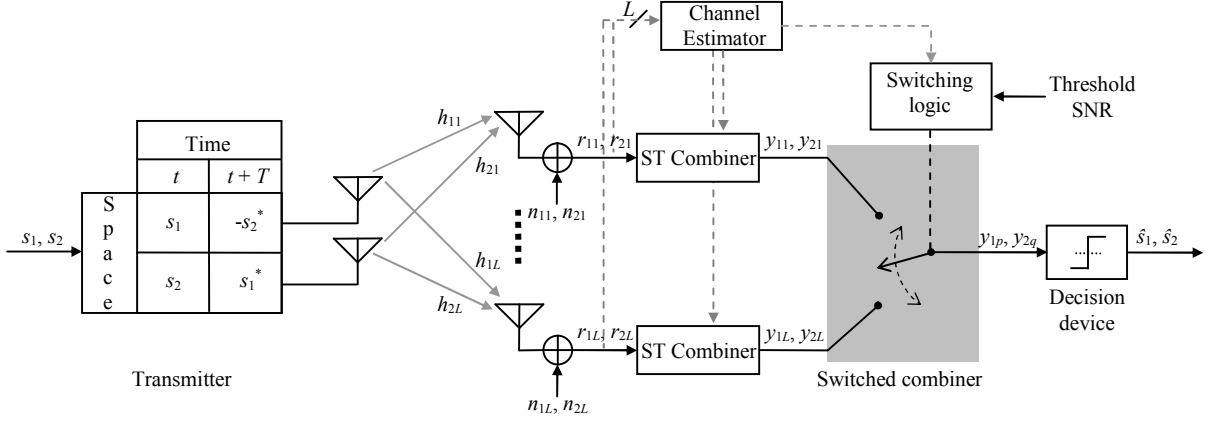


Figure 1. Transmission model of a 2xL MIMO system employing Alamouti code at transmitter and pre-detection switch and examine combining at receiver.

At the receiver, the space time (ST) combiners attached to each branch process the signal to produce an output pair $\{y_{1n}, y_{2n}\}$ given by

$$y_{1n} = \hat{h}_{1n}^* r_{1n} + \hat{h}_{2n} r_{2n}^* \quad (2a)$$

$$y_{2n} = -\hat{h}_{1n} r_{2n}^* + \hat{h}_{2n}^* r_{1n} \quad (2b)$$

where \hat{h}_{mn} is an estimate of h_{mn} . If the channel estimator produces perfect channel state information (CSI), it can be shown that

$$y_{mn} = (\alpha_{1n}^2 + \alpha_{2n}^2) s_m + w_{mn} \quad ; \quad m \in \{1, 2\} \quad (3)$$

by substituting (1) in (2) and using the definition of h_{mn} . The corresponding noise components $\{w_{1n}, w_{2n}\}$ are

$$w_{1n} = \hat{h}_{1n}^* n_{1n} + \hat{h}_{2n} n_{2n}^* \quad (4a)$$

$$w_{2n} = -\hat{h}_{1n} n_{2n}^* + \hat{h}_{2n}^* n_{1n} \quad (4b)$$

As the RV w_{mn} has a variance of $2N_0$, the instantaneous SNR available at the ST combiner output would be

$$\gamma_n = \frac{E}{2N_0} (\alpha_{1n}^2 + \alpha_{2n}^2) \quad ; \quad n \in \{1, 2, \dots, L\} \quad (5)$$

For a Rayleigh fading channel, the distribution of $\{\alpha\}_{m=1, n=1}^{2,L}$ is

$$f_\alpha(\alpha) = \frac{2\alpha}{\Omega} \exp\left(-\frac{\alpha^2}{\Omega}\right) \quad ; \quad E\{\alpha^2\} = \Omega, \quad \alpha \geq 0 \quad (6)$$

Accordingly, the probability density function (PDF) of γ_n will follow a central chi-square distribution with four degrees of freedom

$$f_\gamma(\gamma_n) = \frac{4\gamma_n}{\bar{\gamma}_n^2} \exp\left(-\frac{2\gamma_n}{\bar{\gamma}_n}\right) \quad ; \quad E\{\gamma_n\} = \bar{\gamma}_n, \quad \gamma_n \geq 0 \quad (7)$$

and the corresponding cumulative density function (CDF) would be

$$F_\gamma(\gamma_n) = 1 - \left(1 + \frac{2\gamma_n}{\bar{\gamma}_n}\right) \exp\left(-\frac{2\gamma_n}{\bar{\gamma}_n}\right) \quad ; \quad \gamma_n \geq 0 \quad (8)$$

which can be derived by expressing the CDF with an incomplete gamma function [5, (8.350.1)], and further reducing the same with [5, (8.352.1)].

The diversity combiner operates in discrete time fashion, i.e. the branch switching occurs at time $t = uT$, where u is any integer. As the ST combiners give out the pair $\{y_{1n}, y_{2n}\}$ after every $2T$ amount of time, a parallel to serial conversion (not shown in Fig. 1) is necessary before the output can be fed to the combiner. The channel estimator estimates the current SNR in different branches at every $t = uT$. Using the information, the switching logic block triggers the selector to switch from the current branch to the next branch if SNR in current branch falls below some threshold value (generally found from a table that stores the optimum thresholds for different SNR).

Let the p th and q th branches are selected during the two signalling intervals of interest. The output of the combiner $\{y_{1p}, y_{2q}\}$ is then hard-decoded

$$\{\hat{s}_1, \hat{s}_2\} = \sqrt{E} \operatorname{sgn}(\Re\{y_{1p}, y_{2q}\}) \quad (9)$$

to produce an estimate of the original signal pair $\{s_1, s_2\}$.

III. ANALYSIS OF BER

A. Multi-branch Switch and Examine Combining

With the assumption of statistical independence between fading and noise, the average BER (P_e) can be calculated by averaging the non-fading error probability $P_e(\gamma)$ over the underlying fading random variable (γ) as

$$P_e = \int_0^{\infty} P_e(\gamma) f_{\gamma, SEC}(\gamma) d\gamma \quad (10)$$

where $P_e(\gamma) = Q(\sqrt{2\gamma})$ is simply the conditional error probability of BPSK in AWGN channel [6] and γ is instantaneous SNR per bit at the combiner output. The Q function, also known as Gaussian probability integral, is defined as $Q(z) = \frac{1}{\sqrt{2\pi}} \int_z^{\infty} \exp(-u^2/2) du$. Further, assuming independent and identical (IID) fading, the PDF for SEC, $f_{\gamma, SEC}(\gamma)$, is given by [4, (9.341)]

$$f_{\gamma, SEC}(\gamma) = \begin{cases} f_{\gamma}(\gamma) [F_{\gamma}(\gamma_{th})]^{L-1} & ; \gamma < \gamma_{th} \\ f_{\gamma}(\gamma) \sum_{j=0}^{L-1} [F_{\gamma}(\gamma_{th})]^j & ; \gamma \geq \gamma_{th} \end{cases} \quad (11)$$

where γ_{th} is the switching threshold, and $f_{\gamma}(\gamma)$, $F_{\gamma}(\gamma)$ are the PDF and CDF given by (7) and (8).

Inserting (11) in (10) we obtain

$$\begin{aligned} P_e &= [F_{\gamma}(\gamma_{th})]^{L-1} \int_0^{\gamma_{th}} \mathfrak{v}(\gamma) d\gamma + \sum_{j=0}^{L-1} [F_{\gamma}(\gamma_{th})]^j \int_{\gamma_{th}}^{\infty} \mathfrak{v}(\gamma) d\gamma \\ &= [F_{\gamma}(\gamma_{th})]^{L-1} \int_0^{\gamma_{th}} \mathfrak{v}(\gamma) d\gamma + \sum_{j=0}^{L-1} [F_{\gamma}(\gamma_{th})]^j \int_{\gamma_{th}}^{\infty} \mathfrak{v}(\gamma) d\gamma \end{aligned} \quad (12)$$

where $\mathfrak{v}(\gamma) = P_e(\gamma) f_{\gamma}(\gamma)$. Substituting the expressions of $P_e(\gamma)$ and $f_{\gamma}(\gamma)$, the first integral may be solved through integration by parts

$$\begin{aligned} I_1 &= \int_0^{\gamma_{th}} \mathfrak{v}(\gamma) d\gamma = \frac{4}{\bar{\gamma}^2} \int_0^{\gamma_{th}} \gamma Q(\sqrt{2\gamma}) \exp\left(-\frac{2\gamma}{\bar{\gamma}}\right) d\gamma \\ &= \frac{1}{2} \left[1 - \sqrt{\frac{\bar{\gamma}}{\bar{\gamma}+2}} \left(\frac{\bar{\gamma}+3}{\bar{\gamma}+2} \right) \right] \end{aligned} \quad (13)$$

Similarly the second integral

$$I_2 = \int_{\gamma_{th}}^{\infty} \mathfrak{v}(\gamma) d\gamma = \frac{4}{\bar{\gamma}^2} \int_{\gamma_{th}}^{\infty} \gamma Q(\sqrt{2\gamma}) \exp\left(-\frac{2\gamma}{\bar{\gamma}}\right) d\gamma \quad (14)$$

can be solved as

$$\begin{aligned} I_2 &= \left(1 + \frac{2\gamma_{th}}{\bar{\gamma}} \right) \exp\left(-\frac{2\gamma_{th}}{\bar{\gamma}}\right) Q(\sqrt{2\gamma_{th}}) \\ &\quad - \sqrt{\frac{\bar{\gamma}}{\bar{\gamma}+2}} \left(\frac{\bar{\gamma}+3}{\bar{\gamma}+2} \right) Q\left[\sqrt{2\gamma_{th}} \left(\frac{\bar{\gamma}+2}{\bar{\gamma}} \right) \right] \\ &\quad - \frac{1}{\bar{\gamma}+2} \sqrt{\frac{\gamma_{th}}{\pi}} \exp\left[-\gamma_{th} \left(\frac{\bar{\gamma}+2}{\bar{\gamma}} \right) \right] \end{aligned} \quad (15)$$

where the integral is solved through integration by parts, and [7, (6.5.16)], [7, (6.5.22)] have been used for further simplification.

Putting (13) and (15) in (12), the final BER expression is

$$\begin{aligned} P_e &= \frac{1}{2} [F_{\gamma}(\gamma_{th})]^{L-1} [1 - \Theta(\bar{\gamma})] + \sum_{j=0}^{L-1} [F_{\gamma}(\gamma_{th})]^j \times \\ &\quad \left[\{1 - F_{\gamma}(\gamma_{th})\} Q(\sqrt{2\gamma_{th}}) - \Theta(\bar{\gamma}) Q(\sqrt{2\xi(\gamma_{th})}) \right. \\ &\quad \left. - \frac{1}{\bar{\gamma}+2} \sqrt{\frac{\gamma_{th}}{\pi}} \exp\{-\xi(\gamma_{th})\} \right] \end{aligned} \quad (16)$$

where,

$$F_{\gamma}(\gamma_{th}) = 1 - \left(1 + \frac{2\gamma_{th}}{\bar{\gamma}} \right) \exp\left(-\frac{2\gamma_{th}}{\bar{\gamma}}\right) \quad (17)$$

$$\Theta(\bar{\gamma}) = \sqrt{\frac{\bar{\gamma}}{\bar{\gamma}+2}} \left(\frac{\bar{\gamma}+3}{\bar{\gamma}+2} \right) \quad (18)$$

$$\xi(\gamma_{th}) = \gamma_{th} \left(\frac{\bar{\gamma}+2}{\bar{\gamma}} \right) \quad (19)$$

B. Dual-branch Switch and Stay Combining

In (16), substituting $L=2$, we get the BER expression of Alamouti based SSC scheme as given by

$$\begin{aligned} P_e &= \frac{1}{2} [F_{\gamma}(\gamma_{th})] [1 - \Theta(\bar{\gamma})] + \left[\{1 - F_{\gamma}(\gamma_{th})\} Q(\sqrt{2\gamma_{th}}) - \right. \\ &\quad \left. \Theta(\bar{\gamma}) Q(\sqrt{2\xi(\gamma_{th})}) - \frac{1}{\bar{\gamma}+2} \sqrt{\frac{\gamma_{th}}{\pi}} \exp\{-\xi(\gamma_{th})\} \right] \end{aligned} \quad (20)$$

where, $F_{\gamma}(\gamma_{th})$, $\Theta(\bar{\gamma})$ and $\xi(\gamma_{th})$ are given by equation (17), (18) and (19).

After a bit of algebraic manipulation it can be shown that (20) is alternate form of [3, (21)].

IV. RESULTS AND DISCUSSIONS

Fig. 2 shows the BER performance of Alamouti based multi-branch switch-and-examine combining scheme using BPSK modulation in Rayleigh fading channel for a fixed threshold of $\gamma_{th} = 3$ dB. The theoretical values (represented by solid lines) show excellent match with the Monte Carlo simulations (represented by black dots). The improvement in BER is visible only when $\bar{\gamma}$ lies in the vicinity of the threshold SNR γ_{th} .

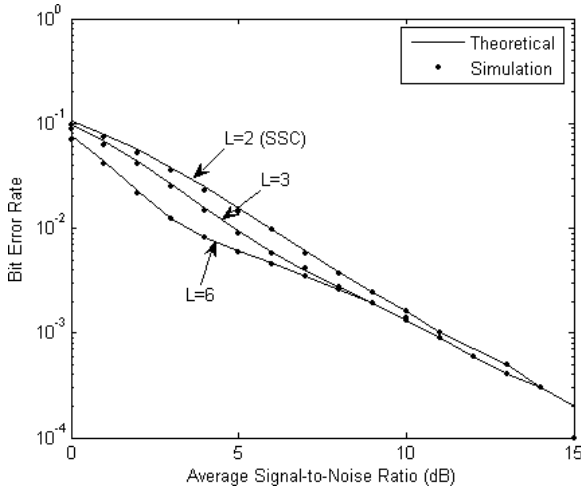


Figure 2. BER versus average SNR curves for Alamouti based SEC scheme with different numbers of Rx antennas. The threshold is set at $\gamma_{th} = 3$ dB in each antenna.

The BER may be substantially improved if the combiner operates with optimum threshold (γ_{th}^*) which may be found by differentiating (16) with respect to γ_{th} , and setting the result to zero, i.e. $\partial P_e / \partial \gamma_{th} |_{\gamma_{th}=\gamma_{th}^*} = 0$. A closed-form expression for γ_{th}^* is, however, unattainable and numerical minimization technique was used to tabulate γ_{th}^* for each value of average channel SNR $\bar{\gamma}$.

TABLE I
OPTIMUM SWITCHING THRESHOLD AS A FUNCTION OF INCREASING AVERAGE SNR PER BRANCH FOR DIFFERENT RX ANTENNAS

$\bar{\gamma}$ (dB)	Optimum common switching threshold		
	$L=2$ (SSC)	$L=3$	$L=6$
0	-1.43	-0.62	0.57
1	-0.62	0.20	1.43
2	0.16	1.00	2.24
3	0.90	1.77	3.05
4	1.60	2.50	3.80
5	2.30	3.20	4.54
6	2.92	3.86	5.25
7	3.52	4.50	5.93
8	4.08	5.09	6.60
9	4.60	5.65	7.20
10	5.09	6.19	7.79
11	5.55	6.69	8.35
12	5.98	7.16	8.89
13	6.38	7.60	9.40
14	6.75	8.04	9.90
15	7.10	8.44	10.4

The corresponding BER plot, for both theoretical and simulated values is given in Fig. 3. The results show that BER values decrease with additional Rx antennas throughout the SNR range. Note that for $L=2$, the BER is identical with the SSC scenario.

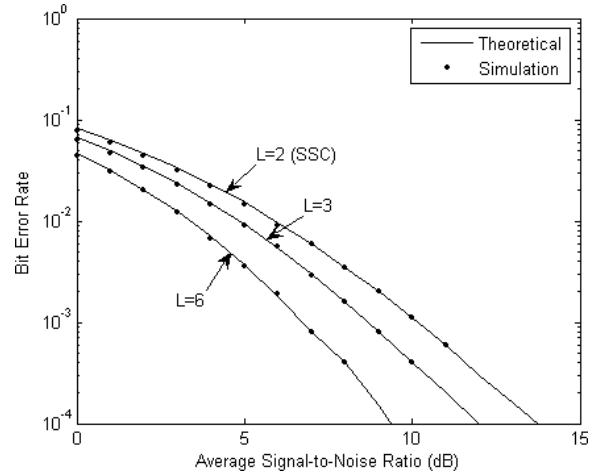


Figure 3. BER versus average SNR curves for Alamouti based SEC scheme with different numbers of Rx antennas. The threshold γ_{th} is set at the optimum value as found from Table I.

V. CONCLUSIONS

In this paper, instead of developing a general $2 \times L$ STBC, we used a 2×1 Alamouti code for each of the receiver antenna and combined the signals to improve the reliability of transmission. A closed-form BER expression of BPSK with SEC over IID Rayleigh fading channel using Alamouti code has been derived through direct PDF based approach. Currently, some efforts to deduce other performance metrics like outage probability and capacity are in progress and will be reported in a future publication.

REFERENCES

- [1] A. Q. Li, G. Li, W. Lee, M. Lee, D. Mazzaresse, B. Clerckx, and Z. Li, "MIMO techniques in WiMAX and LTE: A feature overview," *IEEE Commun. Magz.*, vol. 48, no. 5, pp. 86-92, May 2010.
- [2] S. M. Alamouti, "A simple transmit diversity technique for wireless communications," *IEEE J. Select. Areas Commun.*, vol. 16, no. 8, pp. 1451-1458, Oct. 1998.
- [3] W. Li and N. C. Beaulieu, "Effects of channel errors on receiver selection-combining schemes for Alamouti MIMO systems with BPSK," *IEEE Trans. Commun.*, vol. 54, no. 1, pp. 169-178, Jan. 2006.
- [4] M. K. Simon and M. S. Alouini, *Digital Communication over Fading Channels*, NJ, NY: Wiley-Interscience, 2nd ed., 2005.
- [5] I. S. Gradshteyn and I. M. Ryzhik, *Table of Integrals, Series, and Products*, 7th ed. New York: Academic, 2007.
- [6] J. G. Proakis, *Digital Communications*, NY: McGraw-Hill, 4th ed., 2000.
- [7] M. Abramowitz and I. A. Stegun, *Handbook of Mathematical Functions with Formulas, Graphs, and Mathematical Tables*, NY: Dover, 9th ed., 1970.

Analysis of Multidimensional-TCM Based MB-OFDM UWB System with Pilot-Aided Channel Estimation for High-Rate IEEE 802.15.3a WPANs

Moloy Kumar Chowdhury
ECE Dept.,
Heritage Institute of Technology
Kolkata, India
moloy.futurz@gmail.com

Dr. Chayanika Bose, SMIEEE
ETCE Dept.,
Jadavpur University
Kolkata, India
chayanikab@ieee.org

Abstract—Ultra Wideband is a high data rate, low cost, small size and short range wireless technology that has attracted an avid interest in both the academia and industry, as a high speed alternative to existing wireless technologies such as IEEE 802.11 WLAN, Bluetooth, HiperLAN and HomeRF. This paper presents Multidimensional Trellis Coded Modulation (MD-TCM) based Multi-Band Orthogonal Frequency Division Multiplexing (MB-OFDM) UWB communication system with Pilot-aided channel estimation as a means of achieving higher throughput, range improvement, precise channel estimation, and strong resistance to ICI (Inter carrier Interference) over realistic indoor multipath-fading environments as specified by the IEEE 802.15.3a channel models. The results are verified through extensive Monte Carlo simulations.

Keywords—Multi-Band Orthogonal Frequency Division Multiplexing (MB-OFDM), Multidimensional Trellis Coded Modulation (MD-TCM), Ultra Wideband (UWB), Wireless Personal Area Network (WPAN).

I. INTRODUCTION

Ultra Wideband (UWB) is an exciting new technology that creates a world of opportunities for new wireless applications to be deployed in person-centric area networks such as Wireless Personal Area Networks (WPANs). WPANs have to be designed from a multimedia perspective in order to provide the consumers with the multitude of high quality services as demanded — higher data rates, low-power usage at moderate distances within the personal operating space of the user. As such, UWB is poised to become a widely adopted radio solution for future 4G wireless home-networking technology that serves to facilitate seamless operation among devices and systems at home and SOHO (Small Office Home Office) scenarios. The U.S. Federal Communications Commission (FCC) ruling in February 2002 approved the limited use of unlicensed UWB wireless systems that transmit high-speed data across a broad portion (7.5 GHz) of the UWB spectrum for enterprise and commercial applications [1]. The IEEE 802.15 High Rate Alternative PHY Task Group (TG3a) for WPANs is working on a project to provide a higher speed PHY enhancement amendment to 802.15.3 for applications

involving imaging and multimedia and currently several proposals are being debated. Among the proposals received during the standardization activity, the two major contenders are Multi-Band Orthogonal Frequency Division Multiplexing (MB-OFDM), and DS-UWB (Direct Sequence Spread Spectrum).

MB-OFDM UWB with Quadri-Phase Shift Keying (QPSK) as the modulation technique is one of the two approaches [2-3]. In this paper, the performance of Multidimensional Trellis Coded Modulation (MD-TCM) MB-OFDM system is analyzed using the modified Saleh-Valenzuela (S-V) radio-channel model as proposed by IEEE 802.15.3a for indoor networking in terms of the bit error rate (BER) and packet error rate (PER) as a function of Signal-to-Noise Ratio (SNR) and Distance (d).

II. REVIEW OF ULTRA WIDEBAND

The FCC defines a UWB device as one where the fractional bandwidth is greater than 25% of its center frequency, or occupies 1.5 GHz, whichever is less [1-2]. The UWB spectrum occupies the 3.1–10.6 GHz unlicensed band with a minimum channel bandwidth of 500 MHz, and the spectral mask of -41.3 dBm/MHz, as shown in Fig. 1. Technical standards and operational restrictions regulated by FCC are intended to enable the co-existence of UWB with existing radio

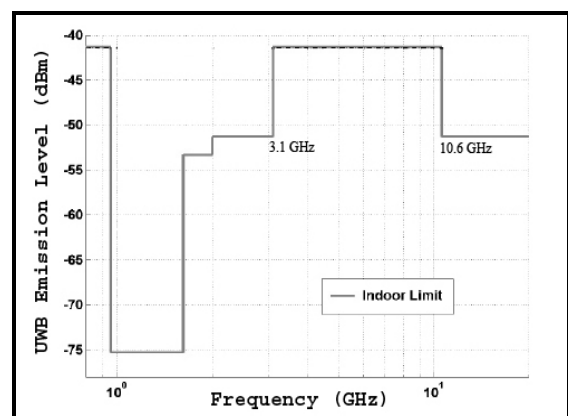


Figure 1. Spectral Mask of UWB.

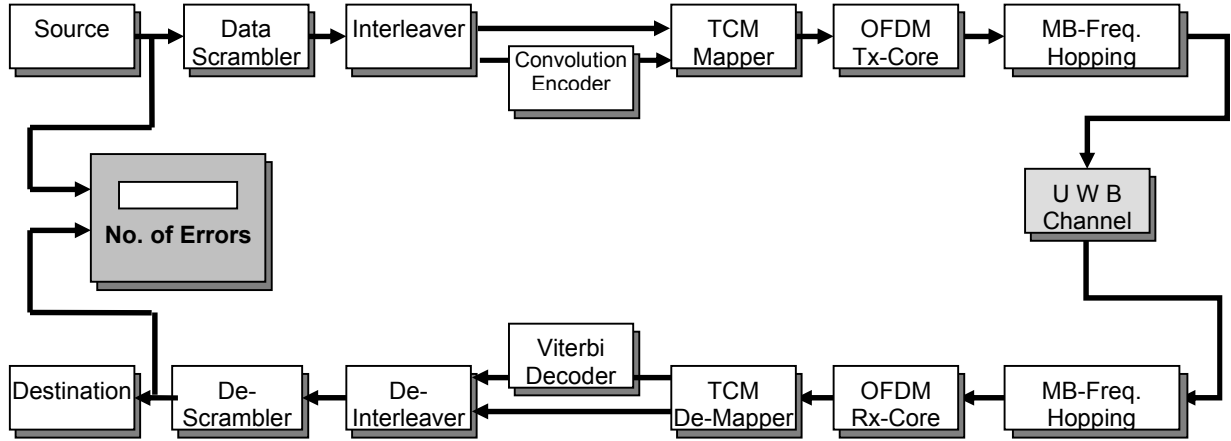


Figure 2. Architecture of MD-TCM MB-OFDM UWB System.

technologies such as IEEE 802.11 (Wi-Fi), HomeRF, and HiperLAN.

III. SYSTEM ARCHITECTURE OF MD-TCM BASED MB-OFDM UWB

This section explains the main components of the MB-OFDM MD-TCM transceiver architecture as shown in Fig. 2.

At the transmitter section, the data bits from the information source are first whitened by the scrambler and then time interleaved to utilize the spectral diversity in improving the reliability of transmission. The convolution encoder thereby encodes a part of the interleaved bits to obtain the desired data rates. The resulting bit sequences of coded and uncoded bits are mapped into constellation symbols using TCM with 8-PSK and the output is converted to OFDM symbols. The channel estimation (CE) is a vital part of MB-OFDM systems in order to equalize the channel precisely. For this purpose, pre-defined Pilot symbols $X_p[k]$ are then multiplexed with the data symbols. The spectrum is sub-divided into several bands of 528 MHz each and in order to exploit time frequency diversity and combat multipath fading, the system operates in one sub-band and then switches over to another sub-band after a short time. The output is thereby mapped into blocks of N symbols $x[0], x[1], x[2], \dots, x[N-1]$ by the serial-to-parallel converter. These N symbols are then converted to OFDM symbols $X[0], X[1], X[2], \dots, X[N-1]$ and transmitted on the N subcarriers by the unitary inverse Fast Fourier Transform (IFFT) as given by:

$$X[n] = (1/\sqrt{N}) \times \sum_{k=0}^{N-1} x[k] \exp(j2\pi nk/N) \quad (1)$$

The transmitted symbols are expressed as:

$$X(n) = X(mL + l) = \begin{cases} X_p(m), l = 0 \\ data, l = 1, 2, \dots, L-1 \end{cases} \quad (2)$$

where L is the interval between the adjacent pilots and $X_p(m)$ is the m^{th} pilot. Cyclic prefix is added to eliminate ISI caused by multipath propagation.

In the receiver, the cyclic prefix is removed and the FFT is performed on the remaining N symbols and the received symbol on subcarrier k can be modeled with complex baseband representation as:

$$y_k = H_k x_k + \eta_k \quad (3)$$

where x_k is the transmitted 8-PSK symbol, H_k is the channel response for the k^{th} carrier and η_k is the additive white Gaussian noise component.

Once the demapping and decoding process is completed at the destination, the received bit sequences are then de-scrambled to acquire back the original information bits.

IV. IEEE 802.15.3A MULTIPATH INDOOR UWB CHANNEL

Among the proposals considered in order to evaluate different PHY layer proposals [4], the IEEE 802.15.3 Working Group for WPANs decided to use the modified S-V model as a reference UWB channel model based on the clustering event to simulate realistic UWB indoor environments [5]. An independent fading method is assumed for each cluster and for each ray associated to the respective cluster. In the S-V models, Poisson processes model both the cluster and ray arrival times independently. The baseband multipath channel impulse response is mathematically modeled as:

$$h(t) = \sum_{l=0}^L \chi_l \sum_{m=0}^M \alpha_{m,l} \delta(t - T_l - \tau_{m,l}) \quad (4)$$

where $\alpha_{m,l}$ is the multipath gain coefficient for cluster l and ray k . The T_l is the arrival time of the l^{th} cluster, $\tau_{m,l}$ is the arrival time of the m^{th} multipath component (ray) in the l^{th} cluster, and χ represents the lognormal shadowing. It is to be noted that $T_l \in [0, \beta]$ and $\chi_{0,l} = 0$ (Assuming) that the respective cluster and ray arrival times are denoted as Λ and λ , the distribution of cluster and ray arrival time is given by:

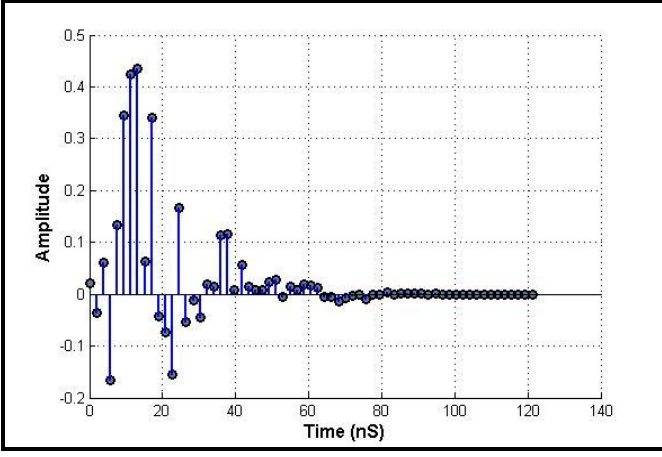


Figure 3. Typical Impulse Response Realization of CM 2.

$$p(T_l / T_{l-1}) = \Lambda e^{-\Lambda(T_l - T_{l-1})}$$

$$p(\tau_{m,l} / \tau_{m-1,l}) = \lambda e^{-\lambda(\tau_{m,l} - \tau_{m-1,l})} \quad (5)$$

The multipath gain coefficient $a_{m,l}$ is a product of $p_{m,l} = \pm 1$ that models signal inversions due to reflections, ξ_l related to l^{th} cluster fading and $\beta_{m,l}$ related to fading of m^{th} ray of l^{th} cluster. The small-scale fading coefficient $\xi_l \beta_{m,l}$ is expressed as log-normal random variable:

$$20 \log_{10}(\xi_l \beta_{m,l}) = \text{Normal}(\mu_{m,l}, \sigma_1^2 + \sigma_2^2) \quad (6)$$

where σ_1^2 and σ_2^2 represents the cluster fading and ray fading respectively. The large scale fading coefficient is also modeled as log-normal random variable:

$$20 \log_{10}(X) = \text{Normal}(0, \sigma_x^2) \quad (7)$$

As the log-normal shadowing of the total multipath energy is captured by the factor X , the total energy contained in the terms $a_{m,l}$ is normalized to unity for each realization and for each channel type. The IEEE 802.15.3a working group suggested four different channel implementations for UWB indoor model, namely, CM1, CM2, CM3 and CM4, which are based on the average distance between transmitter and receiver, and whether a LOS component is present or not. The four channel models (CM 1 to 4) and their parameters are listed in [4].

V. SIMULATION RESULTS

The proposed MD-TCM based MB-OFDM UWB PHY layer model is based on Mode-1 band group (3.1 to 4.684 GHz) and implemented using MATLAB. Assuming a quasi-stationary UWB channel in the simulations, data rate is set at 200 Mbps, and punctured convolution codes are considered with coding rate 5/8, pilot-aided channel estimation and a path-loss exponent of two are assumed for all channel types. As such, the average transmission power is set at $P_{TX} = -10.3$ dBm,

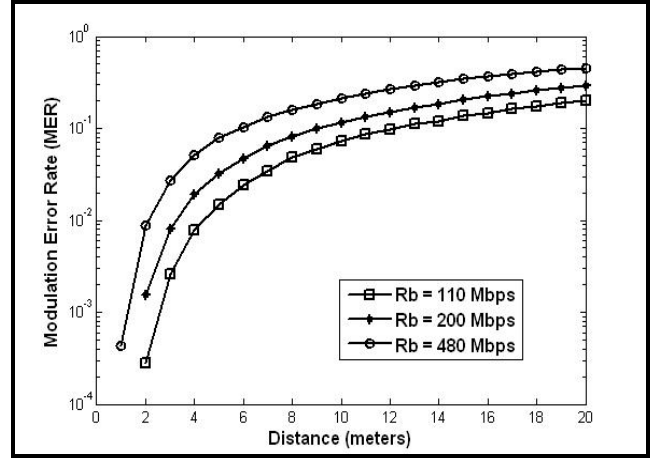


Figure 4. MER as a function of Distance in CM 2 Environment.

8-PSK modulation is used for constellation mapping, and the OFDM FFT/IFFT size is fixed at $N=128$.

The CM2 channel is rich in multipath and its NLOS nature, and short TX — RX separation of 0-4 m makes it ideal for indoor communication such as in office environments. The typical CM2 impulse response is shown in Fig.3. The modulation error rate (MER) as a function of distance against various data rate modes such as $R_b = 110, 200$ and 480 Mbps, is plotted in Fig.4. MER is lowest for small data rates and the error increases as the data rate becomes higher. Monte Carlo simulation results are extensively conducted in both AWGN and multipath indoor channel environments to verify the performance of the proposed MD-TCM MB-OFDM system, and the set of results are presented in Fig.5-6 and listed in Table I. $\alpha + \beta = \chi$. (1) (1)

TABLE I. SYSTEM PERFORMANCE IN CM-2 CHANNEL ENVIRONMENT

Sl. No.	BER Vs. SNR: CM-2		
	Parameters	QPSK	MD-TCM
1	BER=10 ⁻³	SNR=18.8 dB	SNR=14.4 dB
2	$\alpha + \beta = \chi$. (1) SNR=15 dB	BER=0.0063	BER=0.0052
Sl. No.	BER Vs. Distance(d): CM-2		
	Parameters	QPSK	MD-TCM
1	BER=10 ⁻³	d=4.3m	d=7.1m
2	d=10m	BER=0.03	BER=0.015
Sl. No.	PER Vs. SNR: CM-2		
	Parameters	QPSK	MD-TCM
1	PER=10 ⁻¹	SNR=21.8 dB	SNR=17.2 dB
2	SNR=18 dB	PER=.865	PER=0.03
Sl. No.	PER Vs. Distance(d): CM-2		
	Parameters	QPSK	MD-TCM
1	PER=10 ⁻¹	d=3.1m	d=5.3m
2	d=5m	PER=.975	PER=.065

A typical result from computer simulations for the CM-2 channel (presented in Table I) indicates that MD-TCM UWB outperforms QPSK-UWB by ~4 dB, which implies TCM MB-

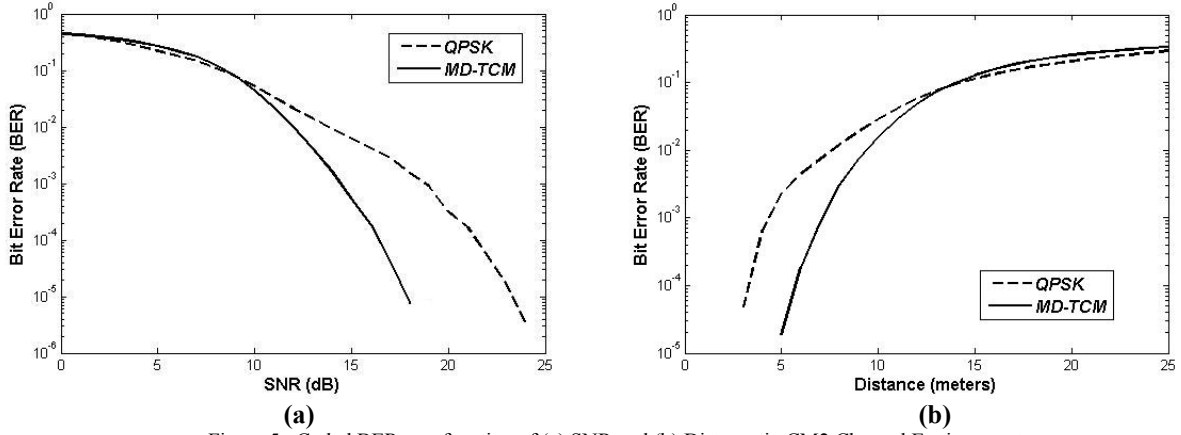


Figure 5. Coded BER as a function of (a) SNR and (b) Distance in CM2 Channel Environment.

OFDM system offers higher reliability over multipath channels and requires lower power consumption that translates to more battery lifetime. Further, the simulation results exhibit that MD-TCM-UWB can operate at a longer range than QPSK-UWB by almost 3 meters. This implies a longer operational range for M-PSK TCM MB-OFDM UWB system.

VI. SUMMARY AND CONCLUSION

In this paper we studied the performance of MD-TCM based MB-OFDM systems and the practical considerations of system design in the IEEE 802.15.3a modified S-V channel environment. The simulated results thus show a dramatic improvement in performance of MD-TCM MB-OFDM UWB over the QPSK-UWB both in terms of performance and distance, and thus, help to conclude that MD-TCM MB-OFDM is a promising technique for highly reliable, low power

wideband transmission. However, this improvement comes at the cost of increased hardware complexity.

REFERENCES

- [1] Federal Communication Commissions, "First report and order 02-48," 2002.
- [2] A. Batra, J. Balakrishnan and A. Dabak, "Multiband OFDM: a new approach for UWB," Internat. Symp. on Circuits Systems, May 2004.
- [3] A. Batra, J. Balakrishnan, A. Dabak and et al., "Multiband-OFDM Physical Layer Proposal for IEEE 802.15 Task Group 3a," IEEE P802.15-03/268r3, March 2004.
- [4] J. R. Foerster, et al., "Channel Modeling Subcommittee Report Final," IEEE P802.15-02/490r1-SG3a, February 2003.
- [5] A. Saleh and R. Valenzuela, "A Statistical Model for Indoor Multipath Propagation," IEEE JSAC, Vol. SAC-5, pp. 128-137, Feb. 1987..
- [6] Simon Haykins, "Digital Communications".

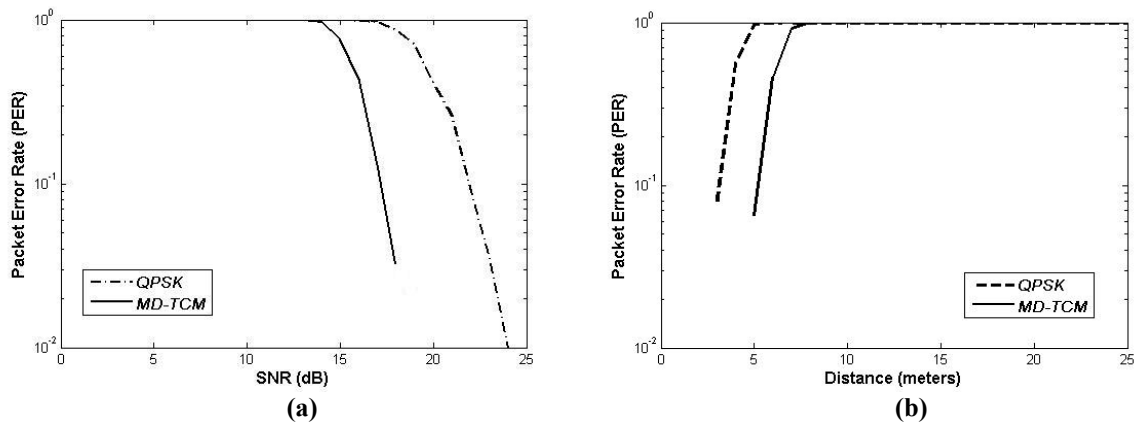


Figure 6. Link PER as a function of (a) SNR and (b) Distance in CM2 Channel Environment.

Performance Analysis of WiMAX PHY

S. M. Lalan Chowdhury¹, P. Venkateswaran²

Dept. of Electronics & Tele-Communication Engg., Jadavpur University, Kolkata – 700 032, INDIA

Email: engg.lalan@yahoo.com¹, pvwn@ieee.org²

Abstract—The development of 802.16 standards for Broadband Wireless Access (BWA) technologies was motivated by the rapidly growing need for high-speed, ubiquitous and cost-effective access. The IEEE 802.16 Standard specifies the air interface for fixed BWA systems in the frequency ranges 10-66 GHz. In this paper, we present a performance analysis model for the WiMAX PHY under different channel conditions and modulation schemes. The performance parameters are given in terms of packet loss and bit loss.

Keywords—WiMAX, OFDM, AWGN, Rayleigh Fading channel, Rician Fading channel.

I. INTRODUCTION

Wireless communications has permeated nearly all facets of human life e.g. home, office, car etc. with the future goal being broadband access and services being available seamlessly virtually everywhere. From a user perspective, this trend of increased use of wireless technology is going to continue because of the convenience, flexibility, and enhanced productivity they offer. From a technical perspective, the trend is towards higher and higher data rates with continued need for higher quality of services.

Worldwide Interoperability for Microwaves Access (WiMAX) which is based upon IEEE 802.16 standard [1]-[2] for Wireless Metropolitan Area Network (WMAN) [2]. In 2004, the IEEE 802.16d standard was published for Fixed Wireless Access (FWA) applications. In December 2005 the IEEE ratified the 802.16e [2] amendment, which aimed to support Mobile Wireless Access (MWA) with seamless network coverage. This standard is now receiving considerable industrial attention. Later the standard extended its operation through different PHY (Physical Layer) specification to 2-11 GHz frequency band enabling Non Line of Sight (NLOS) connections, which require techniques that efficiently mitigate the impairment of fading and multipath [3]. Taking the advantage of OFDM (Orthogonal Frequency Division Multiplexing) technique the PHY layer is able to provide robust broadband service in hostile wireless channel.

The OFDM based physical layer of the IEEE 802.16 standard has been standardized in close cooperation with the European Telecommunications Standards Institute (ETSI) High performance Metropolitan Area Network (HiperMAN) [4]. Thus, the HiperMAN standard and the OFDM based physical layer of IEEE 802.16 are nearly identical. Both OFDM based physical layers shall comply with each other and a global OFDM system should emerge [3]. The WiMAX forum certified products for BWA comply with the both standards.

Recently researchers have started investigating the PHY layer using a simulation model. The authors in [5] propose a

Simulink model for performance analysis of OFDM PHY in terms of BER. However the study focused only on AWGN channel which is not an accurate model for IEEE 802.16e mobile WiMAX systems. The authors in [6] provide a model that studies affect of different modulation schemes on the BER of the system. The proposed model is quite simple and they have also considered only AWGN channel like [5]. The works done in [7] is similar to [4]-[5] with the inclusion of channel estimation and Equalization sub-blocks.

In this paper, we investigate the OFDM PHY layer WiMAX networks under varying channel conditions. This study is carried in conformance with both IEEE 802.16d and 802.16e standards in supporting of both fixed or residential and mobile subscribers.

The rest of the paper has been organized as follows. In section II, all the sub blocks of the Simulink model of WiMAX PHY has been provided. The simulation results has been given in section III and conclusion is given in section IV.

II. WiMAX Model

The Simulink model of WiMAX PHY developed for the study is as shown in Fig. 1, the model consists of transmitter and receiver section linked by the Channel sub systems. In our study the channel subsystem in the model is replaced for different channel models.

A. Channel Coding

Channel coding can be described as the transforming of signals to improve communications performance by increasing the robustness against channel impairments such as noise, interference and fading. The coding is carried out on the data sequences by altering the characteristics of the sequences. The converted sequences then have structured redundancy which enables decision process, by a transmitter or a receiver, less subject to errors. Channel Coding can be described as a three phase process including Randomization, Forward Error Correction and Interleaving.

B. Randomization

Randomization is the first process carried out in the physical layer after the data packet is received from the higher layers. Each burst in Downlink and Uplink is randomized. Randomizer operates on a bit by bit basis. The purpose of the scrambled data is to convert long sequences of 0's or 1's in a random sequence to improve the coding performance. The main component of the data randomization is a Pseudo Random Binary Sequence generator which is implemented using Linear Feedback Shift Register. The generator defined for the randomizer is given by Equation (1) below:

$$1 + x^{14} + x^{15} \quad (1)$$

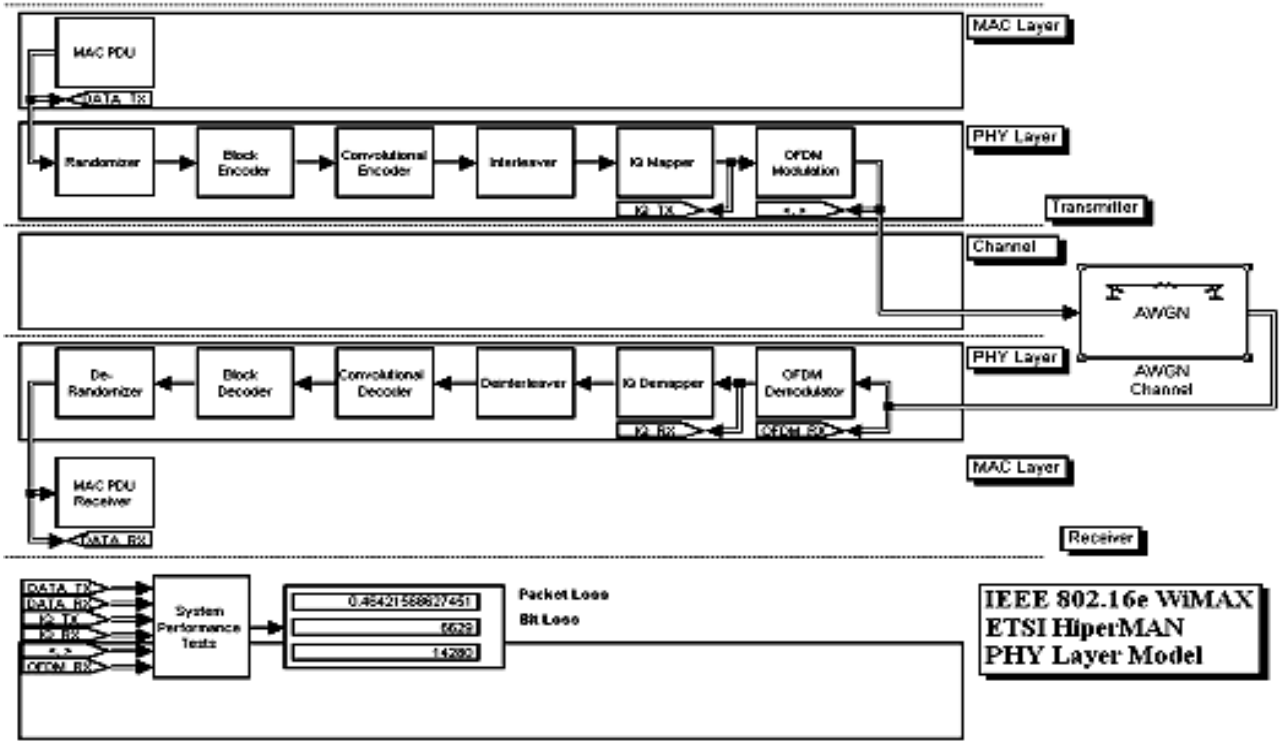


Figure 1. MATLAB Simulink WiMAX OFDM Transceiver

C. Forward Error Correction (FEC)

Forward Error Correction is done on both the Uplink and the Downlink bursts and consists of concatenation of Reed-Solomon Outer Code and a rate compatible Convolutional Inner Code.

D. Reed Solomon Encoding

The purpose of using Reed-Solomon code to the data is to add redundancy to the data sequence. This redundancy addition helps in correcting block errors that occur during transmission of the signal. After randomizer data is passed onto the Reed Solomon Encoder. The encoding process for RS encoder is based on Galois Field Computations to do the calculations of the redundant bits. Galois Field is widely used to represent data in error control coding and is denoted by $GF(2^m)$.

WiMAX uses a fixed RS Encoding technique based on $GF(2^8)$ which is denoted as:

- RS (N = 255, K = 239, T = 8)
- Where:
- N = Number of Bytes after encoding
- K = Data Bytes before encoding
- T = Number of bytes that can be corrected

Eight tail bits are added to the data just before it is presented to the Reed Solomon Encoder stage. This stage requires two polynomials for its operation called code generator polynomial $g(x)$ and field generator polynomial $p(x)$. The code generator polynomial is used for generating the Galois Field Array whereas the field generator polynomial is used to calculate the redundant information bits which are appended at the start of the output data.

These polynomials are defined by the standard [8] as below:

Code Generator Polynomial:

$$g(x) = (x + \lambda^0)(x + \lambda^1)(x + \lambda^2)(x + \lambda^3) \dots (x + \lambda^{2T-1}) \quad (2)$$

Field Generator Polynomial:

$$p(x) = x^8 + x^4 + x^3 + x^2 + 1 \quad (3)$$

E. Convolutional Encoding

Convolutional codes are used to correct the random errors in the data transmission. A convolutional code is a type of FEC code that is specified by CC (m, n, k), in which each in-bit information symbol to be encoded is transformed into an n-bit symbol, where m/n is the code rate (n > m) and the transformation is a function of the last k information symbols, where k is the constraint length of the code. To encode data, start with k memory registers, each holding 1 input bit. All memory registers start with a value of 0. The encoder has n modulo-2 adders, and n generator polynomials, one for each adder.

In WiMAX Physical Layer each RS block is encoded by the binary convolutional encoder, which has a code rate of 7/2 and a constraint length equal to 7. This encoder has two binary adders X and Y and uses two generator polynomials, A and B. These generator polynomial codes are:

$$A = 171 \text{ octal} = 1111001 \text{ binary for X} \quad (4)$$

$$B = 133 \text{ octal} = 1011011 \text{ binary for Y} \quad (5)$$

The output of the convolutional encoder is then punctured to remove the additional bits from the encoded stream. The number of bits removed is dependent on the code rate used.

F. Interleaving

Interleaving is done by spreading the coded symbols in time before transmission. The incoming data into the

interleaver is randomized in two permutations. First permutation ensures that adjacent bits are mapped onto non-adjacent subcarriers. The second permutation maps the adjacent coded bits onto less or more significant bits of constellation thus avoiding long runs of less reliable bits. The block interleaver interleaves all encoded data bits with a block size corresponding to the number of coded bits per OFDM symbol. The number of coded bits depends on the modulation technique used in the Physical layer.

G. Modulation

The interleaver reorders the data and sends the data frame to the IQ mapper. The function of the IQ mapper is to map the incoming bits of data from interleaver onto a constellation. In the modulation phase the coded bits are mapped to the IQ constellation, starting with carrier number -100 on up to carrier number + 100. To simplify transmitter and receiver designs, all symbols in the FCH and DL data bursts are transmitted with equal power by using a normalization factor.

The constellation-mapped data is subsequently modulated onto all allocated data carriers in order of increasing frequency offset index.

III. SIMULATION RESULTS

For performance analysis of the PHY model, simulation is performed by considering the standard test vectors specified in the WiMAX standard document[2]. Several test cases and test vectors for each component are provided in hexadecimal format below:

Data Payload from the MAC Layer (29 bytes frame)

45 29 C4 79 AD 0F 55 28 AD 87 B5 76 1A 9C 80 50 45 IB
9F D9 2A 88 95 EB AE B5 2E 03 4F 09 14 69 58 0A 5D

Data Frame after Randomization Stage (35 bytes frame)

D4 BA A1 12 F2 74 96 30 27 D4 88 9C 96 E3 A9 52 B3 15
AB FD 92 53 07 32 C0 62 48 F0 19 22 E0 91 62 1A C1

Data Frame after Reed-Solomon Encoding (40 bytes frame)

49 31 40 BF D4 BA A1 12 F2 74 96 30 27 D4 88 9C 96 E3
A9 52 B3 15 AB FD 92 53 07 32 C0 62 48 F0 19 22 E0 91
62 1A C1 00

Data Frame after Convolutional Encoding (48 bytes frame)

3A 5E E7 AE 49 9E 6F 1C 6F C1 28 BC BD AB 57 CD BC
CD E3 A7 92 CA 92 C2 4D BC 8D 78 32 FB BF DF 23 ED
8A 94 16 27 A5 65 CF 7D 16 7A 45 B8 09 CC

Data Frame after Interleaving (48 bytes frame)

77 FA 4F 17 4E 3E E6 70 E8 CD 3F 76 90 C4 2C DB F9 B7
FB 43 6C F1 9A BD ED 0A 1C D8 IB EC 9B 30 15 BA DA
31 F5 50 49 7D 56 ED B4 88 CC 72 FC 5C

The following subsections presents the simulation results using the model in Fig. 1, for AWGN channel, Rayleigh fading channel and Rician fading channel respectively.

A. AWGN Channel Simulation by using QPSK & 16-QAM Model

Parameters Considered:

Mode: Signal to Noise Ratio (SNR)
SNR (dB): 5, 10, 15, 20, 25, 30.
Input Signal Power (Watts): 0.01W

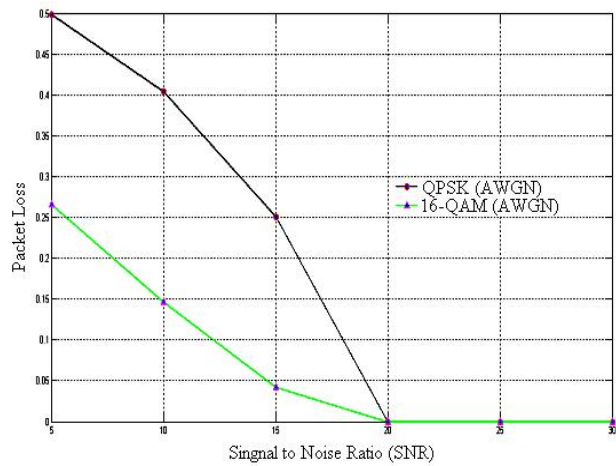


Figure 2. Comparison of Packet Loss between QPSK & 16-QAM in AWGN Channel

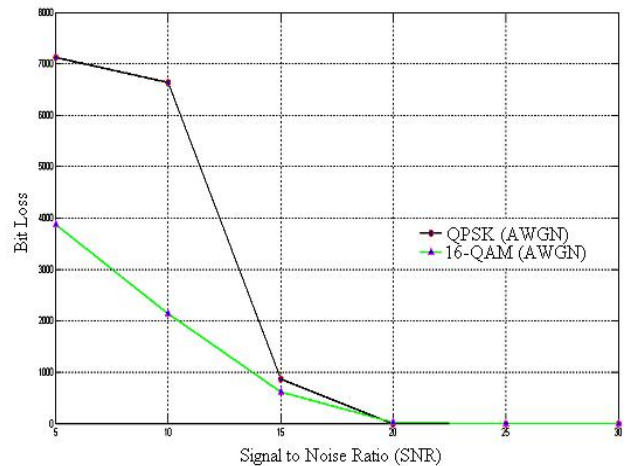


Figure 3. Comparison of Bit Loss between QPSK & 16-QAM in AWGN Channel

B. Rayleigh Fading Channel Simulation by using QPSK & 16-QAM Model

Parameters Considered:

Maximum Doppler Shift (Hz): 5, 10, 15,20,25,30.
 Input Signal Power (Watts): 0.01W

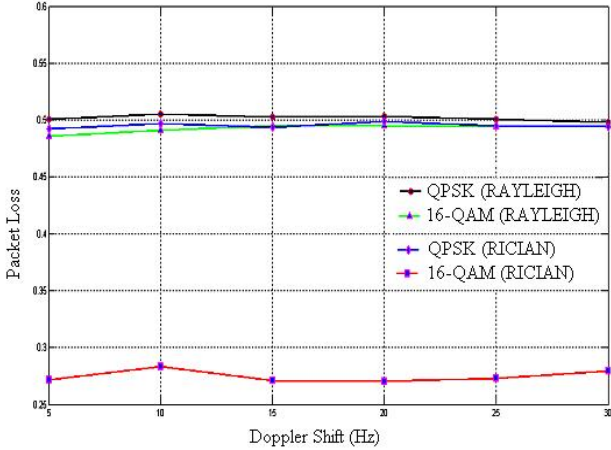


Figure 4. Comparison of Packet Loss between QPSK & 16-QAM in Rayleigh and Rician Fading Channel

C. Rician Fading Channel Simulation by using QPSK & 16-QAM Model

Parameters Considered:

Maximum Diffuse Doppler Shift (Hz): 5, 10, 15, 20, 25, 30.
 Input Signal Power (Watts): 0.01W

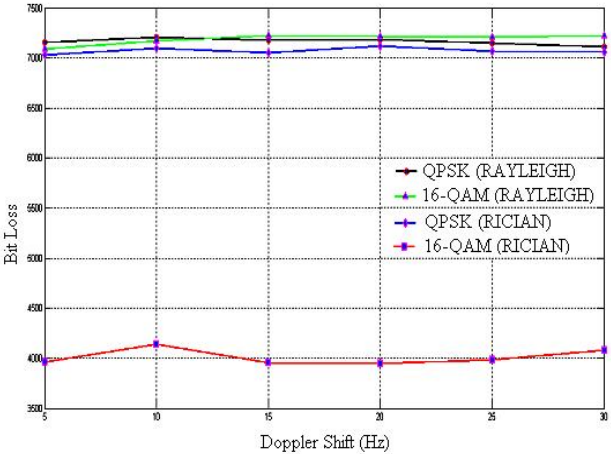


Figure 5. Comparison of Bit Loss between QPSK & 16-QAM in Rayleigh and Rician Fading Channel

The simulation results shown in Fig. 2 & 3; indicates the Packet Loss & Bit Loss in QPSK & 16-QAM modulation scheme respectively under AWGN channel condition. We have obtained the results for QPSK & 16-QAM modulation schemes in PHY layer model under Rayleigh fading & Rician fading channel also. Simulation results in Fig. 4 & 5; shows the comparison of Packet Loss & Bit Loss respectively in

QPSK & 16-QAM modulation scheme under the mentioned fading channel condition.

We observed from the simulation results that the packet & bit loss have been reduced substantially (almost 50%) for 16-QAM modulation scheme comparing with QPSK-an improvement and in case of Fading channels, by comparing the simulation results of both Rayleigh & Rician fading, we observed that the packet & bit losses are less in Rician Fading channel over the Rayleigh fading channel.

IV. CONCLUSION

In this paper, we have presented the WiMAX PHY layer model using Simulink and extensive study were carried out for performance analysis of the model under different channel conditions employing different modulation schemes. The results of the proposed simulation model are expected to enable the researchers in choosing the best model regarding channel performance in IEEE 802.16 OFDM PHY layer.

REFERENCES

- [1] IEEE 802.16-2004, "IEEE Standard for Local and Metropolitan Area Networks. Part-16: Air Interface for Fixed Broadband Wireless Access Systems," Rev. of IEEE 802.16-2001, pp.1-857, Oct. 2004.
- [2] IEEE 802.16e-2005 and IEEE 802.16-2004/Cor 1-2005(Amendment and Corrigendum to IEEE Std. 802.16-2004), "IEEE Standard for Local and Metropolitan Area Networks Part 16: Air Interface for Fixed and Mobile Broadband Wireless Access Systems Amendment 2: Physical and Medium Access Control Layers for Combined Fixed and Mobile Operation in Licensed Bands and Corrigendum 1," pp.1-822, Feb. 2006.
- [3] I. Koffman and V. Roman, "Broadband Wireless Access Solutions Based on OFDM Access in IEEE 802.16," IEEE Comm. Magazine, vol. 40, no. 4, pp. 96-103, Apr. 2004.
- [4] European Telecommunications Standards Institute (ETSI) Broadband Radio Access Networks (BRAN); HIPERMAN; Physical (PHY) Layer. Standard TS 102.177, 2003.
- [5] M. Nadeem Khan, S. Ghauri, "The WiMAX 802.16e Physical Layer Model", IET International Conference on Volume, 2008, pp.117 - 120, 2008.
- [6] Ms Jigisha Patel, Mrs Upena Dalal," A comparative performance analysis of OFDM using MATLAB simulation with M-PSK and M-QAM mapping", ICCIMA 2007,Shivakashi, IEEE CS Press, Vol. 4, pp. 407-411, Dec. 2007.
- [7] Alim, O.A.; Elboghdadly, N.; Ashour, M.M.; Elaskary, A.M., "Simulation of channel estimation and equalization for WiMAX PHY layer in simulink ", Computer Engineering & Systems, 2007. ICCES apos;07. International Conference on vol. 38, Iss.2, pp.274 - 279, Nov. 2007.
- [8] IEEE 802.16-2006: "IEEE Standard for Local and Metropolitan Area Networks - Part 16: Air Interface for Fixed Broadband Wireless Access Systems", 2006.

Effectiveness of Vocal Tract Information for Automatic Speaker Identification Based on Mel Frequency Cepstral Coefficients

K.Mohanty¹, M.Mohanty², S.K.Sanyal³

^{1,3}Dept. of Electronics & Telecommunication Engg.,
Jadavpur University, Kolkata, India

²Dept. of Electronics & Telecommunication Engg.,
Orissa Engineering College, Bhubaneswar, India

¹mohanty_kaushik@yahoo.com, ²rsmadhusmita@gmail.com, ³s_sanyal@ieee.org

Abstract— The objective of this paper is to demonstrate the development of a speaker recognition system using vocal tract information for text-independent mode. The speaker specific information in speech signal mainly varies from person to person due to difference in speech production organs (vocal tract and excitation source) and behavioral characteristic of speaker (speaking rate and speaking style). The spectral information is extracted from a segment of 10-30 ms of the speech signal. In the training and testing process for a given speaker, the vocal tract information from speech signal is extracted by using cepstral analysis. A method based on Mel frequency cepstral coefficients (MFCCs) is proposed for feature of extraction and Vector Quantization (VQ) as modeling technique. Combining the evidence from these features and VQ method seem to improve the performance of the system significantly.

Keywords- Automatic speaker recognition (ASR), Vocal tract, Mel frequency cepstral coefficients (MFCCs), Vector Quantization (VQ).

I. INTRODUCTION

There has been considerable speaker recognition activity over the last six decades. The vocal tract contains more speaker information compare to excitation source and behavioral information. The variation in the shape and size of vocal tract from one speaker to other is reflected as differences in resonance frequencies of the short time spectrum envelope of speech signal [1]. The input to the automatic speaker recognition (ASR) system is the sequence of samples of speech signal collected from either microphone or telephone line, sampled at 8000-16000 samples per second through the analog to digital converter. The general block diagram of ASR system is pictorially shown in Figure 1. It consists of two phases of operation, the training phase and testing phase. The training phase consists of analysis stage, feature extraction stage and modeling stage. The testing stage consists of analysis stage, feature extraction stage, and measurement and comparison stage. The analysis and feature extraction stage in both the phases are same and they differ in the last stage. A speaker identification system is built using 14 dimensional MFCC feature vectors and non-parametric VQ as modeling technique. The Euclidian distance is used for comparison.

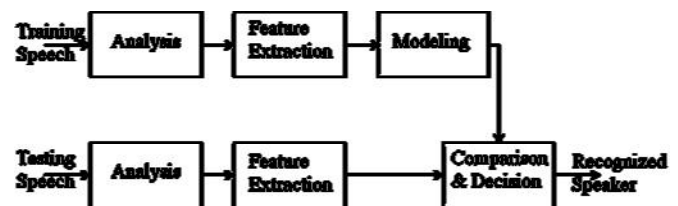


Figure 1. Block diagram representation of the proposed speaker recognition using vocal tract information.

In this work, a text-independent speaker identification system is built by using vocal tract information and the functions of different blocks are as follows.

Since speech is a non-stationary signal, it is processed in frames to perform short term analysis. There are several analysis techniques, Segmental analysis (10-30ms) for vocal tract characteristics, supra-segmental analysis (100-300ms) for high level features such as word duration and sub-segmental analysis (1-5ms) for excitation source information [2].

The output of the analysis stage is a series of frames with large number of samples. These large numbers of samples also contain redundant information. This is because speech is a highly correlated signal. The function of this feature extraction stage is to extract maximum amount of information from those samples with reduced data rate and convert it into vector form called as feature vector. These vectors are put in a k-dimensional space called as feature space, where k is the dimension of the feature vector. Some of the feature extraction techniques are Complex Cepstral Coefficients (CCC), Real Cepstral Coefficients (RCC), Linear Prediction cepstral Coefficients (LPCC) [3] and Mel-Frequency Cepstral Coefficients (MFCC) [4-6].

In the feature space these vectors are shared and overlap each other. Ideally it is required that, these vectors should be distinct for speaker to speaker for better recognition. But that does not happen in practice. In the modeling stage a second level of compression is done, where a set of nearest feature vectors are clubbed together and assigned with representative vector. As a result one model is formed for each speaker.

At the time of measurement, instead of comparing with all the vectors, the comparison is done with the speaker model.

There are several modeling techniques available in literature some of modeling techniques are Vector Quantization [7,8], Hidden Markov model, Gaussian Mixture Model [12], Genetic algorithm and Neural Network [13]. One standard form of compression technique is the vector quantization that we have considered here [7, 8].

In the measurement stage, the similarity between the incoming vector and the corresponding model is measured and decision is taken according to the requirement. The measurement criterion depends upon the modeling technique [1]. If a non parametric modeling technique like VQ is used, the model having close distance to the speech frames is declared as identified speaker.

II. MEL-FREQUENCY CEPSTRAL COEFFICIENT (MFCC) EXTRACTION

A mel is a unit of measure of frequency of a tone. Since the human auditory system perceives on a nonlinear scale, the Mel frequency scale can be used to extract the spectral information [9] and is related to linear frequency by the following relation.

$$f_{mel} = 2595 \log_{10} \left(1 + \frac{f}{700} \right) \quad (1)$$

Using equation (1), a spectrum is constructed with critical bands which are over lapped triangular filter banks [4], the linear spaced frequency spectrum (f_{Hz}) is mapped into nonlinearly spaced frequency spectrum (f_{Mel}). By this we can mimic the human auditory system [9], whose perception at a particular frequency Ω_0 is influenced by energy in a critical band of frequencies around Ω_0 . Based on this concept, MFCC feature vectors are derived. The steps involved to obtain MFCCs from a given speech signal $s(n)$ is shown in Figure-2.

Since speech is a non-stationary signal, it is processed in frames to perform short term analysis. Due to small side lobes, the hamming window provide some what smooth spectrum. For this work, we are using hamming window. Using equation (2) Hamming Window coefficients are generated, with which corresponding speech of frame is scaled.

$$W(n) = 0.54 - 0.46 \cos \left(\frac{2\pi n}{N} \right) \quad (2)$$

For the present work a windowed speech frame of size 20ms(160 samples for 8 kHz Signal) with a shift of 10 ms (80 samples for 8 kHz Signal) is taken to extract vocal tract information [10].

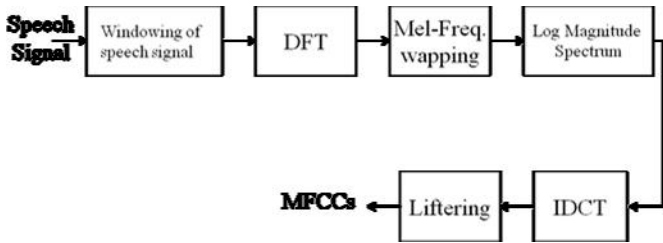


Figure 2. Block diagram representation of MFCCs Computation.

The hamming windowed speech signal is first converted to frequency domain by computing N point (512 point for present case) DFT, which leads to energy spectrum given by (3). Since speech is real signal the energy spectrum is symmetric about Nyquist frequency. It can be seen that spectrum is symmetric about 4 kHz which corresponds to 256point fft bins.

$$|X|^2 = \left| \sum_{n=0}^{N-1} x(n) e^{-j2\pi kn/2} \right|^2 \quad (3)$$

The energy spectrum is then mel-frequency warped to mimic human ear. For the present case the spectrum is symmetric about 4 kHz which is equivalent to 2146 mel in mel scale. The frequency response of mth triangular filters is given by $\psi(i)k =$

$$\left. \begin{array}{ll} 0 & , K \leq C_{m-1} \\ \frac{K - C_{m-1}}{C_m - C_{m-1}} & , C_{m-1} \leq K \leq C_m \\ \frac{C_{m+1} - K}{C_{m+1} - C_m} & , C_m \leq K \leq C_{m+1} \\ 0 & , K \geq C_{m+1} \end{array} \right\} \quad (4)$$

Next, this filter bank is imposed on the spectrum calculated in equation-3. The outputs $e(i)$ for $i=1$ to Q of the Mel-scaled band pass filters can be calculated by a weighted summation between respective filter response $\psi(i)K$ and the energy spectrum $|X(k)|^2$

$$e(i) = \sum_{k=0}^N |X(k)|^2 \psi(i) \quad (5)$$

Log magnitude spectrum is taken to satisfy the concept of cepstral analysis as follows.

$$\{\log[e(i)]\} \quad (6)$$

Finally, IDCT is taken on the log filter bank energies and the final MFCC coefficients $C(n, m)$ is calculated as follows.

$$C(n, m) = \frac{1}{Q} \sum_{i=1}^Q e(i) \cos \left(i \frac{\pi}{Q} (n - \right) \quad (7)$$

$$C(n, m) = \frac{1}{Q} \sum_{i=1}^{\frac{Q-1}{2}} e(i) \cos \left(i \frac{2\pi}{Q} \right) \quad (8)$$

Where $n = 1, 2, 3 \dots M$ for M MFCC coefficients. Since we are taking first 14 MFCC coefficient (ignoring first coefficient out of 15 MFCCs), these coefficient mostly contains vocal tract information.

If the speech signal is collected from two different microphones, due to channel mismatch, the performance of the speaker recognition system reduces. In order to avoid channel mismatch, cepstral mean subtraction (CMS) is done [9]. This may be carried out by calculating the cepstral mean for the entire utterance using equation

$$C_j.mean = \sum_{i=1}^K C_j(i) \quad (9)$$

Where k is the number of MFCC vectors for a given speech signal and $i = 1, 2, 3 \dots M$ is the dimension of each feature vector.

Liftering is a procedure which is used to eliminate the effects of different roll off in various telephone channels on cepstral coefficients [14]. This is achieved by multiplying each MFCC vector by the raised sine function given by the following equation.

$$\omega(n) = \begin{cases} 1 + h \sin\left(\frac{n\pi}{M}\right), & n = 1, 2, 3 \dots \\ 0, & n \leq 0 \text{ and } n \geq M \end{cases} \quad (10)$$

Where h is usually chosen as L/2 and L is typically 10~16 for speech of 4 kHz band-width. The weighted sequence $w(n)C_n$ corresponds to a smoothed log magnitude spectrum.

III. MODELING AND COMPARISON

After getting MFCC feature vector in the modeling stage a second level of compression is done, where a set of nearest feature vectors are clubbed together and assigned with representative vector. For this model the vector quantization (VQ) technique is used for modeling.

For generating code book vectors, we use the popular Binary Split algorithm which in turn uses K-Means Clustering for clustering the feature vectors [4, 11].

Measurement and comparison is done by Euclidean distance, which is given by

$$d(x, y) = [(x - y)^2(x - y)] \quad (11)$$

Since VQ is a non parametric modeling technique, the distance of every speech frames from each model are calculated. Decision is taken by considering the minimum of mean distance.

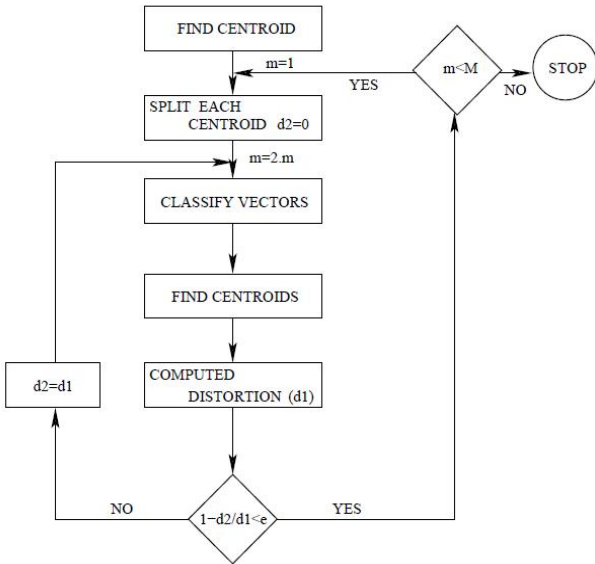


Figure 3. Flow diagram of binary split codebook generation algorithm

IV. EXPERIMENTAL RESULT

For this experiment 30 speakers are randomly selected from TIMIT database. In TIMIT database each speaker has ten sentences. The first eight sentence of each speaker is used for training and last two sentences are used for testing. For each speaker the model is tested twice. Hence in total there are sixty

trials. The identification performance of the system in text independent mode for different code book size is given in table 1. From the table it can be seen that the performance of the identification system is improving with increased codebook size and optimized at 128 codebook size which is quite obvious.

TABLE I. PERFORMANCE OF SPEAKER RECOGNITION SYSTEM USING TIMIT DATABASE OF 30 USERS SET.

Data base	Performance(%) for different Code Book size			
	16	32	128	256
TIMIT 30 Users Set	93.3333	95	96.6667	96.6667

V. CONCLUSION

The main objective of this work is to demonstrate the significance speaker specific information present in the vocal tract. From this identification studies it is found that vocal tract contains most of the speaker specific information. The variation in the shape and size of vocal tract from one speaker to other is reflected as differences in resonance frequencies of the short time spectrum envelope of speech signal. The spectral information is extracted from a segment of 10-30 ms of the speech signal. This system ignores other speaker specific information such as supra segmental information like pitch and duration and the information regarding the characteristics of excitation source.

Further direction for this work may be to develop some techniques to extract excitation source information from speech signal and to develop some combination technique to combine excitation source information with vocal tract information to improve overall performance.

REFERENCES

- [1] J. P. Campbell, "Speaker recognition: A tutorial," in Proc. IEEE, vol. 85, no. 9, pp. 1437-1462, Sept 1997.
- [2] B. Yegnanarayana, Senior Member, IEEE, S. R. Mahadeva Prasanna, Jinu Mariam Zachariah, and Cheedella S. Gupta, "Combining evidence from source, suprasegmental and spectral features for a fixed text speaker verification system," in IEEE Trans. Acoust., Speech, Signal Processing, vol. 13, no. 4, pp. 575 - 582, July 2005.
- [3] B.S.Atal, "Effectiveness of linear prediction characteristics of the speech for automatic speaker identification and verification," in J. Acoust. Soc. Amer, vol. 55, pp. 1304-1312, June 1974.
- [4] S.B.Davis and P.Mermelstein, "Comparison of parametric representations for monosyllabic word recognition in continuously spoken sentences," in IEEE Trans on Acoust., Speech, Signal Processing, vol. SSP-28, no. 4, pp. 357-366, August 1980.
- [5] A. E. Rosenberg and M. R. Sambur, "New techniques for automatic speaker verification," in IEEE Trans. Acoustics, speech, Signal Processing, vol. ASSP-23, pp. 169-176, 1975.
- [6] S. Furui, "cepstral analysis technique for automatic speaker verification," in IEEE trans. Acoustics, speech, signal processing, no. ASSP-24, 1981.
- [7] F. K. Soong, A. E. Rosenberg, L. R. Rabiner, B. H. Juang, "A vector quantization approach to speaker recognition," in AT&T Technical Journal, vol. 66, pp. 387-390, 1985..
- [8] L. Rabiner and B. H. Juang, Fundamental of Speech Recognition. Pearson Education, 2006
- [9] F. J. Bimbot, et.al., "A tutorial on text-independent speaker verification," in EURASIP Journ. on Applied Signal processing, pp. 430-451, 2004.

- [10] K. Sri Rama Murty and B. Yegnanarayana, "Combining evidence from residual phase and mfcc features for speaker recognition," in *IEEE Signal Processing Letters*, vol. 13, no.1, pp. 52–55, Jan 2006.
- [11] T. Matsui and S. Furui, "Comparison of text-independent speaker recognition methods using VQ-distortion and Discrete/Continuous HMMs," *IEEE Transactions On Speech And Audio Processing*, Vol. 2, No. 3, pp. 456-459, July 1994.
- [12] D. A. Reynolds, Richard C. Rose, "Robust text-independent speaker identification using gaussian mixture speaker models," in *IEEE Trans. on Speech Audio Processing*, vol. 3, no. 1, pp. 72–83, Jan 1995.
- [13] N. Fakotakis and J. Sirigos, "A high performance text independent speaker recognition system based on vowel spotting and neural nets," in *IEEE Conference Proceeding Acoust., Speech, Signal Processing*, vol. 2, pp. 661 –664, 1996.
- [14] Jayant M. Naik, Lorin P. Netsch and George R. Doddington, "Speaker verification over long distance telephone lines," in *Proc. ICASSP*, pp. 524–527, 1989.

Propagation Characteristics of FSO Link Using Partially Coherent Gaussian Optical Beam

Sachin M. Kale

Department of Electronics & Telecommunication
Engineering, Jadavpur University, Kolkata.
smkale50@gmail.com

Asim Kar

Department of Electronics & Telecommunication
Engineering, Jadavpur University, Kolkata.
asimkar@rediffmail.com

Abstract—Propagation characteristics of a free space optical communication (FSO) link using coherent and partially coherent Gaussian beams for wireless connections between two high speed LANs have been theoretically investigated and simulated using MATLAB programs. Variations in Scintillation index due to atmospheric turbulence causing random signal loss at the receiver have been considered as the major source of disturbance at the communication receiver. In order to achieve better performance of the communication link, partially coherent Gaussian beam has been used at the transmitter while aperture averaging on the incoming optical signal is done at the receiver to improve the quality of receiver performance. The improvements due to combined effect of partially coherent optical beam and the aperture averaging of the received optical beams are calculated and compared for different values of the aperture widths. Optical sources of two wavelengths i.e., 780nm and 1550 nm were considered for performance analysis and comparison of results. Simulations result are presented to predict the link parameters of FSO link under coherent and partially coherent beam condition for the above two wavelengths for a given aperture width. Compared to 785nm wavelength, much reduced scintillation index and free space loss with partially coherent beam are obtained at 1550nm.

Keywords— FSO, LAN, Scintillation Index, Aperture averaging

I. INTRODUCTION

Now days, LANs are design to accommodate not only for high speed data traffic but also avail the facility of broadband multimedia communication [3]. However, there are some applications where more than one local LANs are to be accommodate to form a MAN . Now it may be necessary to connect two high speeds LANs to exchange information among themselves, where the possibility of connecting the LANs using fiber optic cables (lese lines) may not be cost effective and geographically permissible such as two Institute campuses or Industrial area[4].

Free space optical communication (FSO) has attracted special attention since a few years as it can provide huge data transmission rate. In FSO a laser beam is used as a wireless connectivity between transmitter and receiver. But in practice atmospheric turbulence causes random fluctuations of phase and amplitude of the received signal called scintillation, can result in a considerable degradation [5] of the system performance.

Variety of techniques available to mitigate the effects of optical turbulence. For example, increasing the size of the receiver aperture offers an effective and simple way to reduce turbulence-induced signal fades. The use of multiple Transceiver aperture with equal gain combining (EGB) [6] and adaptive optical control techniques reduces intensity fluctuations [9].

Recently aperture averaging (spatial diversity) effects has been studied to mitigate the influence of scintillation by using optical coherent beams. In the present paper we investigate the influence of aperture averaging techniques by using partially coherent beam.

First we introduce the basic model of FSO link then we list the analytical expressions that describe the scintillation index base on kolmogorov turbulence spectrum . In third section Aperture averaging factor “A” is analysed for both coherent and partially coherent beam. In further section we discuss the performance of FSO link by comparing wavelength (λ), distance(L), beam width(W_0) and refractive index structure parameter C_n^2 .

II. OPTICAL SCINTILLATION MODELLING

To study the effect of turbulence (homogeneous) on optical beam we consider a coherent and partially coherent Gaussian laser beam propagating through the atmosphere to a receiver along horizontal path as shown in Fig.1. The optical field [1],[2]unit amplitude written as

$$U(x,y)=\exp\left(-\frac{x^2+y^2}{w_0^2}\right) \quad (1)$$

here w_0 is the initial beam size and x and y are the horizontal and vertical coordinator of the incident beam field from beam centre respectively. The irradiance function of the beam at a distance L from the source can be express as

$$I(x,y,L)=\frac{w_0}{w^2}\exp\left[-\frac{2(x^2+y^2)}{w^2}\right] \quad (2)$$

where w is the average beam size or radius at the receiver ,

Given by,

$$w = w_0 \left[1 + \left(\frac{2L}{kw_0} \right)^2 \right]^{1/2} \left[1 + 1.63 \sigma^{12/5} \Lambda(L) \right]^{1/2} \quad (3)$$

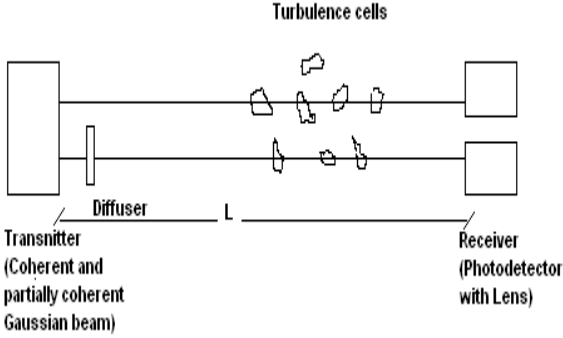


Fig1. Propagation Geometry

where $k = 2\pi / \lambda$ is wave number, λ is the wavelength of the beam, σ^2 is the Rytov variance and $\Lambda(L)$ is the fresnel ratio for vacuum propagation.

$$\text{Rytov variance } \sigma^2 = 1.23 C_n^2 k^{7/6} L^{11/6}$$

where C_n^2 is the refractive index structure constant that characterizes the strength of the index of refraction fluctuations

Using the kolmogorov spectrum and standard extended Rytov theory the on axis scintillation index for weak turbulence ($l=0$, $L=\infty$) is given by.

$$\sigma_{I,w}^2 = 3.86 \sigma^2 \left\{ \begin{array}{l} 0.4 \left[(1 + 2\Theta(L))^2 + 4(\Lambda(L))^2 \right]^{5/12} \\ \cos \left[\frac{5}{6} \tan^{-1} \left(\frac{1 + 2\Theta(L)}{2\Lambda(L)} \right) \right] \\ - \frac{11}{6} (\Lambda(L))^{5/6} \end{array} \right\} \quad (4)$$

The fresnel ratio $\Lambda(L)$ is the beam spread due to diffractions when propagate through air. $\Lambda(L)$ is associated with the beam curvature parameter $\Theta(L)$, which is the phase curvature of the beam as it propagate in vacuum defined as.

$$\Theta(L) = \frac{\Theta_0(L)}{\Theta_0^2(L) + \Lambda_0^2(L)}$$

where $\Theta_0(L) = 1 - \frac{L}{F_0}$ is the initial phase curvature

and for Gaussian beam $F_0 = \infty$ Hence $\Theta(L) = 1$

$$\Lambda(L) = \frac{\Lambda_0(L)}{\Theta_0^2(L) + \Lambda_0^2(L)}$$

where

$$\Lambda_0(L) = \frac{2L}{kw_0^2}$$

is the initial fresnel ratio.

For moderate to strong turbulence scintillation index is

$$\sigma_{I,s}^2 = \exp \left\{ \frac{0.49 \sigma_{I,w}^2}{\left[1 + 0.56(1 + \Theta) \sigma_{I,w}^{12/5} \right]^{7/6}} + \frac{0.51 \sigma_{I,w}^2}{\left(1 + 0.69 \sigma_{I,w}^{12/5} \right)^{5/6}} \right\} - 1 \quad (5)$$

Expressions for partially coherent beam are derived as same as above equation except the input beam parameters are change due to diffuser located at the transmitter side with different diffuser correlation length $l_c = 0.1, 0.001$ as shown in Fig.1

$$\Lambda_{eff}(L) = \frac{2L}{kw_0^2} \quad \text{and} \quad \Theta_{eff} = \frac{\Theta_0}{\Theta_0^2 + \Lambda_0^2 N_s}$$

$N_s = 1 + \frac{2w_0^2}{l_c^2}$ is the number of scattering centre.

In the plane of receiver detector,

$$\sigma_{I,x}^2(D) = \frac{0.49 \left(\frac{\Omega - \Lambda_1}{\Omega + \Lambda_1} \right) \sigma_{I,s}^2}{\left[1 + \frac{0.4(2 - \bar{\Theta}_1) \left(\frac{\sigma_{I,s}}{\sigma} \right)^{12/7}}{(\Omega + \Lambda_1) \left(\frac{1}{3} - \frac{1}{2} \bar{\Theta}_1 + \frac{1}{5} \bar{\Theta}_1^2 \right)^{6/7} + 0.56(1 + \Theta_1) \sigma_{I,s}^{12/5}} \right]^{7/6}}$$

$$\sigma_{I,y}^2(D) = \frac{(0.51 \sigma_{I,s}^2) / \left(1 + 0.69 \sigma_{I,w}^{12/5} \right)^{5/6}}{1 + \left[1.20 \left(\frac{\sigma}{\sigma_{I,s}} \right)^{12/5} + 0.83 \sigma^{12/5} \right] / (\Omega + \Lambda_1)}$$

$$\sigma_I^2(D) = \exp \left[\sigma_{I,x}^2(D) + \sigma_{I,y}^2(D) \right] - 1 \quad (6)$$

Similarly, irradiance variance for partially coherent beam is given as

$$\sigma_{P \ln, x}^2(D) = \frac{0.49 \left(\frac{\Omega - \Lambda_{eff}}{\Omega + \Lambda_{eff}} \right) \sigma_{Pl, s}^2}{\left[1 + \frac{0.4 \left(2 - \bar{\Theta}_{eff} \right) \left(\frac{\sigma_{Pl, s}}{\sigma} \right)^{\frac{12}{7}}}{\left(\Omega + \Lambda_{eff} \right) \left(\frac{1}{3} - \frac{1}{2} \bar{\Theta}_{eff} + \frac{1}{5} \bar{\Theta}_{eff}^2 \right)^{\frac{6}{7}} + 0.56 \left(1 + \Theta_1 \right) \sigma_{l, s}^{\frac{12}{5}}} \right]^{\frac{7}{6}}}$$

$$\sigma_{P \ln, y}^2(D) = \frac{\left(0.51 \sigma_{Pl, s}^2 \right) / \left(1 + 0.69 \sigma_{Pl, s}^{\frac{12}{5}} \right)^{\frac{5}{6}}}{1 + \left[1.20 \left(\frac{\sigma}{\sigma_{Pl, s}} \right)^{\frac{12}{5}} + 0.83 \sigma^{\frac{12}{5}} \right] / \left(\Omega + \Lambda_{eff} \right)}$$

$$\sigma_{P, l}^2(D) = \exp \left[\sigma_{P \ln, x}^2(D) + \sigma_{P \ln, y}^2(D) \right] - 1 \quad (7)$$

and $\sigma_{\ln, x}^2(D), \sigma_{\ln, y}^2(D)$ are the large and small scale log-irradiance scintillations, Ω normalized receiver aperture size given by $2L/kW_G^2$.

III. APERTURE AVERAGING FACTOR

After propagating through atmospheric turbulence in the channel the quality of the beam at the receiver deteriorates and begins to break up into random regions of high and low intensity. Increasing the size of the receiver aperture relative to the size of these regions of low intensity, averages the signal fluctuations and thus decreasing the signal fading, this phenomenon is known as ‘aperture averaging’.

The aperture averaging factor ‘A’ is defined by the normalized variance of power fluctuations of the incident optical field on collecting lens. It is the ratio of the irradiance flux variance obtained by a finite-size collecting lens having diameter D to that obtained by a point receiver or on axis flux variance.

From equations (5) and (6) we can define Aperture averaging factor both [8] for coherent and partially coherent beam as

$$A = \sigma_I^2(D) / \sigma_{I, s}^2(0) \quad \& \quad A = \sigma_{Pl, s}^2(D) / \sigma_{Pl, s}^2(0). \quad (8)$$

Where $\sigma_I^2(D)$ & $\sigma_{I, s}^2$ are the scintillation index for receiver lens of diameter D and a ‘point receiver’ (D=0) respectively. Under moderate to strong turbulence conditions, only eddies of size smaller than coherence radius ρ_0 or larger than the scattering disk $L/k\rho_0$ contribute effectively [9] [10] to the atmospheric turbulence. To take into account this dependence of the turbulence on Coherent and partially coherent beams, it is proposed to consider an Aperture averaging factor ‘A’ to mitigate the effects scintillation by considering the three special cases of weak, moderate and strong turbulence with different wavelengths. The effects of aperture averaging on the received signal is given by

$$\sigma_{I, s}^2 = A * \sigma_{I, s}^2 \quad (9)$$

IV. NUMERICAL RESULTS

All simulation were realized in the MATLAB environment with beam parameters considered as follows.

Wavelength $\lambda = 1550nm \& 785nm$.

Distance $L = 1000m$, Refractive Index structure parameter

$C_n = 10^{-12}, 10^{-14} \& 10^{-16} m^{-\frac{2}{3}}$ for weak, moderate and strong turbulence conditions respectively [7].

Beam width W and diameter D of receiver aperture for both coherent and partially coherent beam is chosen as 0.025m and 0.08m. First, consider the case of aperture averaging for both beams with different wavelength 1550 nm and 785nm with refractive index structure parameter for weak turbulence $C_n = 10^{-14}$ as shown in following fig.2 and fig.3 it is observed that the scintillation index for lower optical wavelength 785nm without aperture averaging is more pronounced compared to 1550nm for 1km distance.

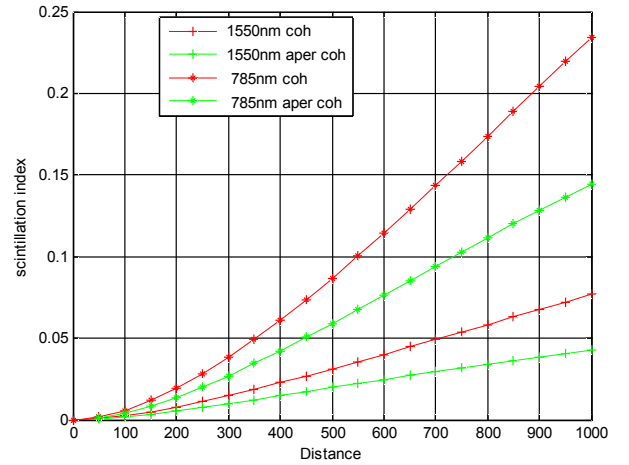


Fig.2 Scintillation index for coherent beam

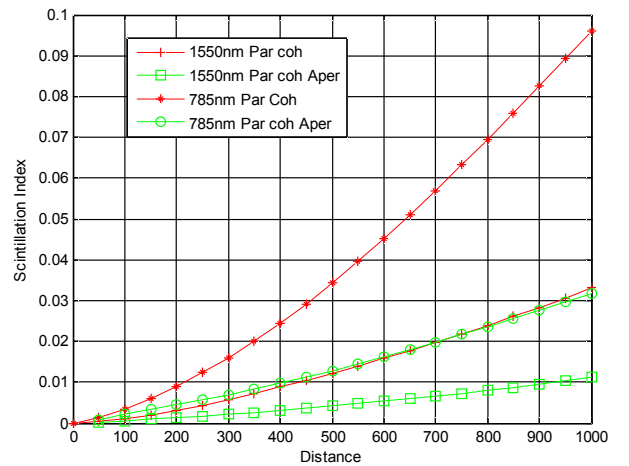


Fig.3 Scintillation index for partially coherent beam

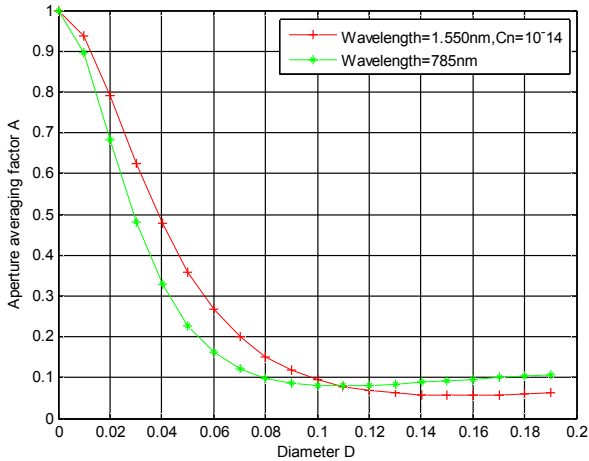


Fig4 Aperture averaging factors 'A' Vs aperture diameter 'D' for wavelength 1550nm and 785nm respectively.

The aperture-averaging factor A as shown (fig.4) is a function of the receiver lens diameter D for different beam wavelengths and turbulence strength. More aperture averaging occurs when optical turbulence is stronger, because for stronger turbulences, coherence length decreases compared to the size of the receiver aperture. Smaller wavelength results in a smaller coherence length relative to the size of receiver aperture thus for higher wavelength 1550nm more value of A compared to 785nm.

V. CONCLUSIONS

In this work theoretical development of the propagation characteristics of a FSO link in turbulent atmosphere using coherent and partially coherent Gaussian beams have been made. The scintillation index of the FSO link for 1 km distance is studied under moderate to strong atmospheric turbulence conditions where aperture averaging was done to observe the improvement in performance of the system. With the refractive index structure parameter = $C_n=10^{-14}$ and the

aperture width =8 cm, the performance of the system was studied at the 785 and 1550 nm wavelengths.

Results are verified using MATLAB simulation. It is observed that for 1550nm and 785nm wavelength, scintillation index variations is more pronounced for 785nm coherent Gaussian beam compared to partially coherent beam. By using aperture averaging techniques with partially coherent beam it shown that intensity fluctuations is reduced by 30% and 50% at wavelength 1550nm and 785nm respectively, In future different configurations and arrangements will be proposed to mitigate the scintillation effects in FSO link using partially coherent Gaussian optical beam. Further work is planned to study the effect of multiple wavelengths in mitigating the fog effects in the atmosphere using partially coherent light and adaptive optics at the receiver.

REFERENCES

- [1] Andrews L.C. , Phillips L.R. , Laser beam propagation through random medium , SPIE Press 2005.
- [2] Joseph Montoya, " Propagation of narrow bandwidth wavelength radiation through the atmosphere ", Army Research Laboratory, ARL 2008
- [3] Ahmed Mahdy and Jitender S. Deogun. "Wireless optical communication: a Survey", IEEE WCNC, 2004
- [4] Jinlong Zhang , "Proposal of free space optical mesh network architecture for broadband access" , IEEE 2002
- [5] S. Robert , "A Survey of clear-air propagation effects relevant to optical communications", proceedings of the IEEE, 1970
- [6] Zhu and Khan , "Free-Space optical communication through atmospheric turbulence channels", IEEE Transactions on communications vol.50, Aug 2002
- [7] P.Raj, S. Sharma, P.C.S. Devara, "Study of laser scintillation in different atmospheric conditions" Journal of Applied Meteorology. Vol.32. No 6. June 1993.
- [8] L. C. Andrews; R. L. Phillips; C. Y. Hopen aperture averaging of optical scintillations: power fluctuations and the temporal spectrum, Waves Random Media , Vol-10, 53-7, (2000)
- [9] Heba Yuksel and Christopher C. Davis, aperture averaging experiment for Optimizing receiver design and analyzing turbulence on Free Space Optical communication links , IEEE, Conference on Lasers & Electro-Optics (CLEO) 2005.
- [10] Jennifer C. Ricklin 1, Stephen M. Hammel", Frank D. Eaton and Svetlana L ,Lachinova , "Atmospheric channel effects on free-space laser communication " , Springer Science 2006.

An Optimized Sensor Node Deployment Scheme for WSN based Flood-Forecasting Systems

Ramesh Jana, Souvik Kr. Mitra, Shovan Maity, Arnab Raha, Mrinal Kanti Naskar

Advanced Digital and Embedded Systems Laboratory

Department of Electronics and Telecommunication Engg, Jadavpur University, Kolkata – 700032

E-mail: -rak_janak@rediffmail.com, souvikmitra.ju@gmail.com, shovanju35@gmail.com, arnabraha1989@gmail.com, mrinalnaskar@yahoo.co.in

Abstract—Wireless sensor network (WSN) technology finds its application in an ever increasing number of domains including military, healthcare, environmental monitoring and smart homes and offices. Very recently work has been done to develop efficient disaster forecasting systems utilizing WSN technology. Such networks pose a tremendous design challenge. They must have the ability to cope with node failure, limited power, wide variety of sensors and the need for communication over a large area. While designing such a system a part of the focus should be on developing a low cost yet reliable communication interface between the predictive environmental sensor network and the government administration involving very little human interference. This paper describes an efficient deployment scheme of sensor nodes required to ensure communication link between the WSN at site and the government office.

Keywords—WSN, Intermediate Node (IN), Routers, 2-connectivity, Predictive Environmental Sensor Network (PESN)

I. INTRODUCTION

Natural disasters such as river floods, hurricanes, etc. tremendously affect the lives of the poor and under privileged. A lot of work has been done to develop systems which help to minimize the damage through early disaster predictions. The main deployment targets for such networks are rural and developing regions which are the most severely affected. This leads to a problem of limited cost, limited power and limited bandwidth. Due to the lack of any existent technology in the rural regions, deploying and practically implementing such systems becomes a very difficult task. The general architecture of such systems consists of sensor nodes which sense and collect the data relevant for calculations, some nodes with large processing powers which implement the distributed prediction algorithm and the government office which verifies the results with the available online information, implements a centralized version of the prediction algorithm as a redundancy mechanism, issues alerts and initiates evacuation procedures. The network must be able to continue its operation in case of any node failure. Thus there is a need for more than one disjoint communication path between the nodes and the

government office. In most of the regions where the forecasting system is deployed there is a lack of existent wireless communication technology. As a result intermediate nodes (INs) have to be deployed to ensure connectivity between the nodes and the government office, in case the office does not fall within the communication range of the nodes. As part of our work to develop such a forecasting system specifically river flood forecasting we developed a model for deployment of INs. In this paper we propose a minimalistic scheme to ensure 2-connectivity between the WSN and the government office. Our proposed scheme tries to minimize cost at the same time ensuring sufficient connectivity so that the system does not fail in the event of node failures.

II. RELATED WORK

Flood forecasting systems available today are mostly telemetric, although there are some instances of wireless sensor networks (WSNs) based flood forecasting systems mainly in developed countries. We get some instances of two-tiered sensor network architecture [1] employing sensor nodes both for measuring and computing purposes, but in none of the cases we find a definite procedure for deployment of those nodes. A similar type of WSN based network using Gumstix nodes [2] which suffers from the need of significant power, and another architecture [3] which has no clear indication on the basin characteristics of the river and deployment scheme can be found in the literature available so far. [4] has presented a k-connected and k-covered model for deployment of sensor nodes. [4] in turn has referred to [5] for its own development of the deployment scheme. [5] has presented a 1-connected and 1-covered perspective which has been proved to be able to use minimum number of nodes to cover and connect the region. [6].

III. PROPOSED WORK

In our architecture for flood prediction and forecasting systems it is not necessary to cover the whole area with

sensors as temperature, water level, rainfall and other factors of our interest does not vary widely over short distances. Our objective is to connect the whole system from the field to the office node so that a centralized prediction algorithm can predict and forecast any possibility of flood beforehand.

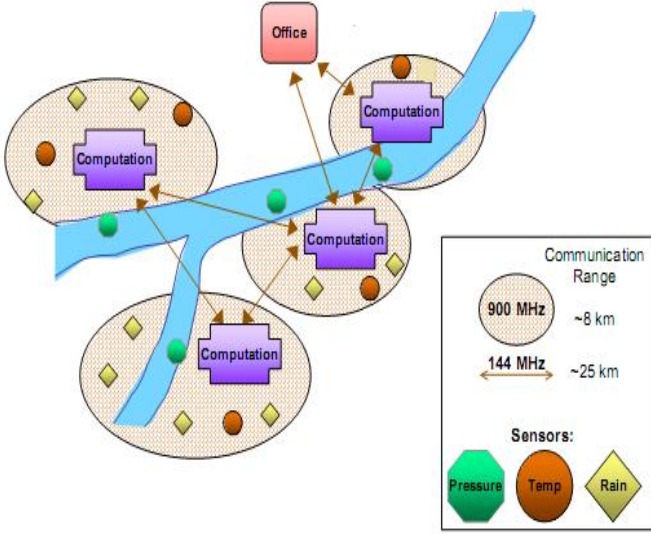


FIG 1.

Problem Statement

We will focus on finding an optimum scheme for deploying INs to ensure that all the nodes have two disjoint paths for communicating with the office, i. e. the entire WSN is 2-connected with the office.

Mathematical Formulation

The following notations are used:

- N_r : number of nodes, placed close to the river.
- N_{in} : number of INs.
- R_i : i th node of the flood forecasting system (placed close to the river).
- IN_i : i th IN.
- d_i : the distance between the i th river monitoring node and office node.

Given:

- i) The physical topology of the river, which could be expressed by a single mathematical equation or piecewise curves each having a different equation.
- ii) X_o, Y_o : The x and y coordinate of the office node.
- iii) r : the range of communication for each node.
- iv) l : length of the river to be monitored.
- v) h : the number of river node hops allowed in a communication path.

Variables:-

- i) X_{in_i}, Y_{in_i} : x and y coordinate of the i^{th} IN.
- ii) X_{r_i}, Y_{r_i} : x and y coordinate of the i^{th} node placed on the river.

Assumptions:

- i) There is no limit to the number of IN hops allowed.
- ii) All the nodes have routing capabilities.

Mathematical proof of minimal deployment:

We know that the shortest distance between two points is a straight line. So we will need minimum number of INs if we place them on straight line segments between the nodes and the office. If n nodes are deployed in a stretch of river then to connect these n nodes to the office through 2 disjoint paths, minimum number of routers will be needed if we connect the end nodes to the office node. This can be proved as follows: There are three schemes in which n nodes can be 2-connected to the office via straight line paths.

i) Connect the end nodes with the office node through routers.

ii) Connect any two nodes, other than the end nodes, to the office through routers and place duplicate nodes to the left and right of those two nodes respectively.

Duplicate nodes need to be placed to the right and left of these two nodes to ensure 2-connectivity.

If there are n nodes on the river segment then the pairs of nodes which could connect the river to the office is given by $\{N_i, N_j\}$ where $0 \leq i, j > i; j \leq n-1$;

Let the number of nodes needed to connect node N_i to the office node be p_i , where $p_i = \lfloor (d_i/r) \rfloor$ where $\lfloor x \rfloor$ is the greatest integer less than or equal to x .

For scheme (i) we consider the pair $\{N_0, N_{n-1}\}$. Clearly for scheme (i) the number of INs required is $\lfloor d_0/r \rfloor + \lfloor d_{n-1}/r \rfloor$. For scheme (ii) we consider all the pairs except for the pair $\{N_0, N_{n-1}\}$. If we connect $\{N_i, N_j\}$ through INs to the office then the number of extra nodes to achieve two connectivity is $\lfloor d_i/r \rfloor + \lfloor d_j/r \rfloor + i + (n-1-j)$. These include routers as before along with duplicate nodes. The duplicate nodes are essentially sleep nodes which operate only when original nodes fail thus conserving power.

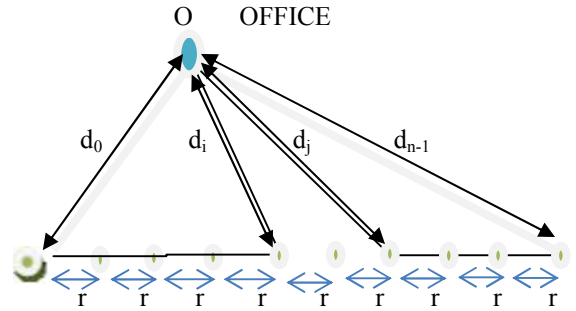


FIG 2.

From the triangle N_0ON_i we get that $d_0 < (d_i + i*r)$
 So $\lfloor d_0/r \rfloor \leq \lfloor d_i/r \rfloor + i$
 Similarly from triangle $N_{n-1}ON_j$ we get $d_{n-1} < (d_j + (n-1-j)*r)$
 So $\lfloor d_{n-1}/r \rfloor \leq \lfloor d_j/r \rfloor + (n-1-j)$
 So, we get that $\lfloor d_0/r \rfloor + \lfloor d_{n-1}/r \rfloor \leq \lfloor d_i/r \rfloor + \lfloor d_j/r \rfloor + i + (n-1-j)$ for all i, j such that $\{i, j\} \neq \{0, n-1\}$
 So, among all the pairs $\{N_0, N_{n-1}\}$ will need the minimum number of routers to connect the nodes to the office in a two connected manner.

Therefore (i) is a better scheme of deployment than (ii).

iii) Connect any one of the nodes to the office and place a duplicate node for each node from the end nodes up to the node where the router branch starts. Also a duplicate for each router should be placed.

In this scheme any node N_i can be chosen. The number of extra nodes needed in this case will be $2*[d_i/r]+n-2$. Now from triangle N_0ON_i we get $d_0 < (d_i+i*r)$ and hence $[d_0/r] \leq [d_i/r]+i$.

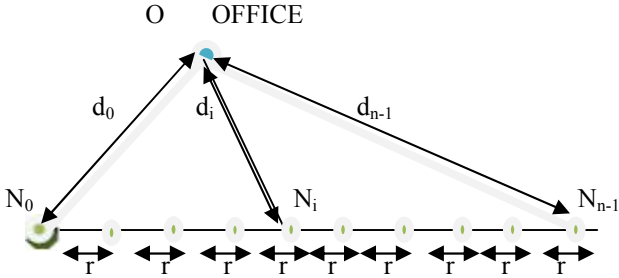


FIG 3.

From triangle N_iON_{n-1} we get $d_{n-1} < (d_i+(n-i-1)*r)$ and hence $[d_{n-1}/r] \leq [d_i/r]+(n-i-1)$

This gives us $[d_0/r]+[d_{n-1}/r] \leq 2*[d_i/r]+n-1$

For any value of i we can see that the maximum number of extra nodes required for scheme (i) is just 1 greater than the number of extra nodes required for scheme (iii). Therefore the worst case performance of scheme (i) is just about the same as the performance of scheme (iii) for large n . Scheme (iii) can only work better than scheme (i) if the segment of nodes is close to the office node. Thus in most situations scheme (i) works better.

So far we considered a small river segment. To connect the entire river monitoring system with the office in an optimum way not only do we need several such segments but also need to minimize the number of such segments.

We take the point where the first river monitoring node is placed as the origin, i.e. $X_{r_0}=0, Y_{r_0}=0$. (X_{r_i}, Y_{r_i}) is chosen so that $[(X_{r_i}-X_{r_{i-1}})^2+(Y_{r_i}-Y_{r_{i-1}})^2]^{0.5} \leq r$

Now to optimize the number of nodes required to monitor the river we place them as far as possible, i. e. The inter node distance is as close to r as possible. For convenience in calculations we consider the inter node distance to be r .

$Y_{r_i}=f(X_{r_i})$ where i is an integer such that $0 \leq i < N_r$ and f is the function defining the river flow.

The number of nodes needed to monitor the river of length l is approximately given by $[l/r]+1$.

$$d_i = [(X_{r_i}-X_0)^2 + (Y_{r_i}-Y_0)^2]^{0.5}$$

The number of router branches needed so that there are maximum h river node hops in each communication path is given by $b = [N_r/h]$

Therefore one simple way to minimize the number of INs is to set up routers on the straight line path between a river monitoring node and the office after every h river monitoring nodes. Such a scheme manages to break the river into segments where the end nodes have been connected to the office through routers just like in scheme (i). If there are some

river monitoring nodes which can communicate directly with the office node then alongside the router paths there exists another communication path through that node. Then the system becomes more reliable. In the event of the office node being close to the river the number of INs reduces and we can ensure connectivity by placing a duplicate for those nodes which can communicate directly with the office. But in the case the office node is located far away from the river site our scheme works best. However to ensure 2-connectivity of all the river nodes with the office we need to place duplicate nodes for the very small number of nodes which are there towards the ends of the length of the river being monitored. These duplicate nodes as already mentioned are essentially sleep nodes. For a very long river and a distant office node the number of those duplicate nodes is quite small compared to the number of INs.

It has been mentioned in the early parts of the paper that cost is always a bottleneck in designing such systems. Therefore to minimize cost we can alter the value of h as much as the routing capabilities of the nodes allow us. Doing so there is a chance that the number of INs may decrease. To what extent the number of INs decrease depend on the nature of the river flow.

It is shown that for 1-coverage and 1-connectivity the best possible scheme is given in [5]. but in that case they are also interested in covering the whole area. But in our case we are not interested in covering the whole region so the number of nodes needed in our case is less than the number of nodes needed in that case. There is no scheme in literature which addresses only the connectivity issue without addressing the coverage issue to the best of our knowledge. So our scheme is better than all the schemes addressing both coverage and connectivity for the specific problem at hand.

IV. SIMULATION RESULTS

We performed simulations of our deployment scheme in MATLAB. We viewed the entire deployment of INs for various lengths of the river and for various positions of the office. The communication range of the nodes was taken as 25km for one set of simulations and 15km for another set of simulations. We also change the hop limit and see how that helps in decreasing the number of INs. Also we assume the curvature of the river to follow a definite equation. The figure given below shows the deployment scheme of INs. The red node is the office node. The green nodes resemble the river monitoring nodes and the black ones resemble the INs. A table is also provided which gives the number of INs and sleep nodes for all the cases we simulated.

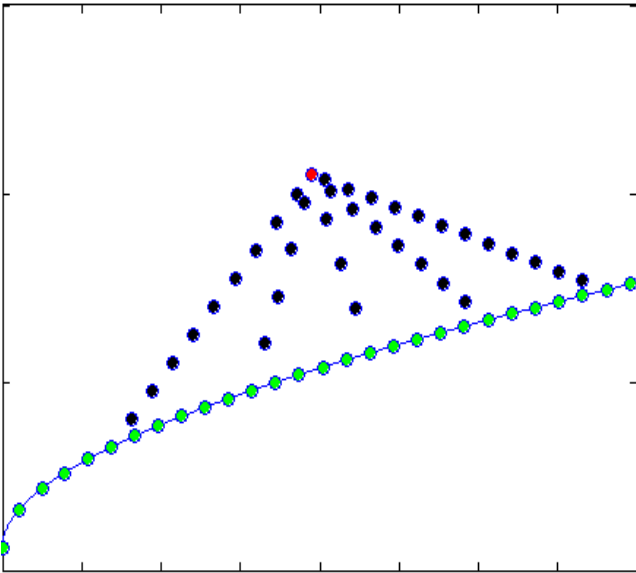


FIG 4.

TABLE 1.

Length Of The River (Km.)	Range Of Nodes (Km.)	Number of hops	Office dist. (Km)	Number Of INs+ sleep nodes	Total number of River Monitoring nodes
500	25	4	41	15+8	25
300	25	4	41	8+8	13
300	25	5	41	6+6	13
500	25	5	41	10+9	21
500	25	3	41	26+4	21
300	25	3	41	11+4	13
300	25	3	95	14+5	13
500	25	3	95	34+4	21
300	25	4	95	9+8	13
500	25	4	95	23+7	21
300	25	5	95	8+7	13
500	25	5	95	16+9	21
300	15	5	46	35+7	21
500	15	5	46	52+6	34
500	15	5	95	60+6	34
300	15	5	95	24+8	21
300	15	4	46	23+7	21
500	15	4	46	32+7	34
500	15	4	95	56+8	34
500	15	4	95	68+8	21
300	15	3	46	28+7	21
500	15	3	46	88+6	34
500	15	3	95	89+7	34
300	15	3	95	90+6	21

From the results we see that for an office node which is not far away from the river the number of routing nodes required is quite small and since these nodes only need to possess routing capabilities, implementing the system is not a very costly affair. However we also see that under no existent infrastructure the number of routers required for a very long river and a distant office node is quite larger than the number of river monitoring nodes. As it is evident from the results when the number of hops is allowed to be 4 as compared to 3 or otherwise 5 as compared to 4 the number of INs decrease thus reducing the cost. However increasing the maximum hop count might reduce the reliability of communication as the packets have to be relayed by a greater number of nodes. so we have to make a calculated trade-off between the reliability of the system and cost. Also we see that increasing the range of the node's communication capability decreases the number of nodes, but that would mean an increase in the cost of individual nodes. Thus from this simulation results we can reduce the total cost of the system by choosing the proper communication range of the nodes.

V. CONCLUSION

As we have seen our work is as optimal as possible(geometrically).However since proposing a general scheme for varying geographical topologies is a tremendously tough task our work is as close to a general scheme as possible. Also our idea is useful under the circumstances that there is absolutely no existent infrastructure available at the deployment region. The length of the river being monitored, the nature of river flow and the location of the Government office determine the number of INs required ensuring connectivity. To connect a very long river to a single office node the number of INs would be large. In such a case to minimize the number of routers some infrastructure has to exist.

REFERENCES.

[1] Elizabeth A. Basha, Sai Ravela and Daniela Rus. Model-Based Monitoring for Early Warning Flood Detection SenSys 08, November 5-7, 2008, Raleigh, North Carolina, USA.

[2] D. Hughes, P. Greenwood, G. Blair, G. Coulson, F. Pappenberger, P. Smith, and K. Beven. An intelligent and adaptable grid-based flood monitoring and warning System. In Proceedings of the 5th UK eScience All Hands Meeting, 2006.

[3] M. Castillo-Effen, D. H. Quintela, R. Jordan, W. Westhoff, and W. Moren. Wireless sensor networks for flash-flood alerting. In Proceedings of the 5th IEEE International Caracas Conference on Devices, Circuits and Systems, pages 142-146. IEEE, Nov 2004.

[4] You-Chiun Wang and Yu-Chee Tseng. Distributed Deployment Schemes for Mobile Wireless Sensor Networks to Ensure Multi-level Coverage. Ieee Transactions On Parallel And Distributed Systems, Tpd-2007-04-0119.R2.

[5] Y. C. Wang, C. C. Hu, and Y. C. Tseng, "Efficient deployment algorithms for ensuring coverage and connectivity of wireless sensor networks," Proc. IEEE First Int'l Conf. Wireless Internet (WICON '05), pp. 114–121, 2005.

[6] X. Bai, S. Kumar, D. Xuan, Z. Yun, and T. H. Lai, "Deploying wireless.

Comparative Study of Discrete radio model and First order radio model for data gathering in Wireless Sensor Network

Swarup Kumar Mitra¹, Joydeep Banerjee², M.K. Naskar³

^{1,2,3} Advanced Digital and Embedded Systems Lab, Department of ETCE, Jadavpur University, Kolkata– 32, India
swarup.subha@gmail.com¹, jogs.1989@gmail.com², mrinalnaskar@yahoo.co.in³

Abstract: Wireless Sensors Network consists of irreplaceable nodes after being deployed with limited energy resources. The data gathering protocol needs more realistic power consumptions model to estimate the network performance for various pervasive and ubiquitous applications. In this paper we have implemented the data gathering protocols using discrete radio model and compared the results with conventional radio model for balanced power control and network lifetime. The energy consumption model utilizes discrete transmit power levels of the CC2420 radio chip used by MICAz sensor motes. Log Normal Shadowing Model is modeled to obtain the received signal strength.

Keywords: Data gathering, Discrete Radio Model, CC2420 Radio chip, Log Normal Shadowing Model,

I INTRODUCTION

Wireless Sensor Network (WSN) consists of several nodes in count of hundred or thousand operating in remote location and harsh environment. The major resource constraint is the energy consumption in the network as the sensor nodes being equipped by irreplaceable batteries. A network with even topology is deployed randomly with sensor nodes. The sensor networks are required to transmit gathered data to the base station (BS) or sink. Each node is provided with transmit power control and omni directional antenna and therefore can vary the areas of its coverage. Since communication requires significant amount of energy compared to computations, sensor nodes must collaborate in an energy-efficient manner for transmitting and receiving data so that lifetime can be enhanced and also a better “energy x delay” [1] performance is achieved. Heinzelman *et al.* in [2] developed a cluster-based routing scheme called Low-Energy Adaptive Clustering Hierarchy (LEACH), where in each cluster, member nodes adopt a Time Division Multiple Access (TDMA) protocol to transmit their data packets to the cluster head. After receiving data packets from all its local members, a cluster head performs data aggregation and sends the final aggregated packet to the Base Station under the Carrier Sense Multiple Access (CSMA) protocol. To avoid cluster heads dying quickly, LEACH rotates the roles of cluster heads among all the sensor nodes. In doing so, the energy load is distributed

evenly across the network and network lifetime (in unit of data collection round) becomes much longer than the static clustering mechanism. Compared with the Minimum Transmission Energy (MTE) routing scheme [3], where communication distance is the only criterion for selecting low-energy routes, LEACH utilizes a more accurate energy model and offers much better performance in terms of energy efficiency and network lifetime. The Power Efficient Gathering in Sensor Information Systems (PEGASIS) scheme proposed in [4] is based on a greedy chain, which starts from the farthest node from the Base Station. By connecting the last node on the chain to its closest unvisited neighbor, PEGASIS greatly reduces the total communication distance and achieves much better energy and lifetime performance than LEACH for different network sizes and topologies. This problem was even approached by modern heuristic techniques like Ant colony Optimization [5], trying to optimize energy dissipation. The PEGASIS scheme depends upon a greedy chain formation whereas the LEACH scheme randomizes the leader selection in the network. While the greedy chain can not always guarantee minimal energy consumption, the randomized leader selection does not take into account the node's capability in being the leader, in terms of its energy content and transmit distance. For shortest hop between each communication pair of nodes, i.e. SHORT[6]. It also depends on the number of packets. An efficient hybrid data gathering scheme [7] which is a combination of clustering and shortest hop pairing of the sensor nodes. The cluster heads and the super leader are rotated every round for ensuring an evenly distributed energy consumption among all the nodes. In reality a transmit power level of the sensor node can only be adjusted to discrete values which may result in single power level for multiple values of distance. The real issue of energy balancing in WSN can be utilized fully through an efficient power control of nodes. In this paper we have implemented the data gathering protocol using discrete power control [8].

We introduce a radio model discussed in [9], which dynamically determines which power level setting should be used to transmit between two nodes. Using the power level setting, the cost of transmissions is calculated based off the chip specifications to ensure an accurate estimation. Comparative plots produce a benchmark in system performance.

The novelty of our paper is that we have taken into consideration that the sensor nodes are limited to few discrete power levels as in Crossbow MICAz motes that uses ChipconCC2420 radio chip [10]. Secondly assuming Log-normal Shadowing path loss model which detects an occurrence of an event at a particular distance from the node [11]. Our simulation results shows performance of the network in terms network lifetime and sustainability of the network in terms of mean energy over the conventional radio model. We have applied our realistic power consumption model over shortest hop chain formation and load balancing energy aware data gathering algorithm. The remainder of the paper is organized as Section 2 describes the Network radio model and the radio propagation path loss, Section 3 deals with Realistic power data gathering algorithm, Section 4 contributes about simulation results and finally conclusion and future works in Section 5.

II. NETWORK RADIO MODEL

A typical sensor node consists of four major components: a data processor unit, a micro-sensor unit, a radio communication subsystem that consists of transmitter/receiver electronics, antenna, and an amplifier; and a power supply unit. Although energy is dissipated in all of the first three components of a sensor node, we mainly consider the energy dissipation associated with the radio component.

In this paper we introduces a radio model [8], which dynamically determines which power level setting should be used to transmit between two nodes. Using the power level setting, the network lifetime and mean energy of the network is calculated based on the chip specifications to ensure an accurate estimation of lifetime. Transmission can only occur at predefined discrete power levels of the amplifier, based on the RSSI [9] value needed for communication. Discrete radio model provides more realistic simulations however in real world deployments. In real world deployments there may be obstacles and environment conditions that prevent accurate estimation. Due to this, the estimated power levels for transmission between nodes can only be used as a starting point Energy dissipation for reception or transmission is constant for a particular power level.

The sensor network taken into our consideration for our simulation.

(i) We have considered here a square field with base station located at (50m, 150m)

(ii) Nodes are dispersed randomly following a uniform distribution in a 2-dimensional space which is static and stationary after deployment.

(iii) Nodes are capable of transmitting at discrete power levels depending on the distance from the receiver. For example as the chip specification of CC2420 we have available transmission power levels according to distance.

(iv) Nodes can estimate the received signal strength for communicating between the nodes according to the available transmission power levels.

In most work, authors assume that the power level can be adjusted to the exact need and calculate the energy cost using these exact values. In reality this is not the case as the radio can only be adjusted to one of the associated power levels and not set to the exact transmission power needed. Using the assumption that there is an infinite amount of transmission levels, previous work makes the assumption that the longer links will cost more to transmit a packet. In many situations two links of different lengths will need to transmit at the same power level setting in order for the packet to be received and therefore the cost to transmit over different distances can be equivalent. We also have analyzed the basic parameters involved in the conventional first order radio model and discrete radio model. The power level consideration from the actual data sheet of MICAz[10] is also discussed in relevant sections. The sensing of an event depends also on the received signal strength indication (RSSI).

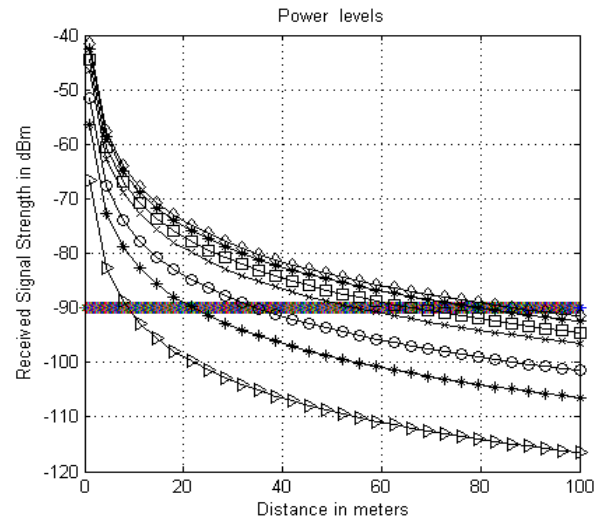


Fig 1 Received signal strength in dB_m vs Distance in meters

Sensing is a probabilistic feature which introduces a path loss component which depends on antenna height of transmitter and receiver as well as distance between transmitting and receiving mote. For received signal strength to obtain the seven power levels we have introduced a Log normal shadow model as shown in Fig 1. The dependency of all the factors (obstacles such as building, foliage) has been taken into account in this sensing model. The sensing ability of a mote is not uniform in all direction hence we have assumed a Log Normal Shadow fading sensing model to calculate the path loss. The signal loss for the plane earth model [11] is given by equation (1), when experiment is the done concerning the relationship between the distance between the transmitter and receiver, d , satisfies packet reception rate and the RSSI.

$$L(d)=L(d_0) + 10*\beta*\log(d/d_0) \dots\dots\dots(1)$$

where β is the path loss exponent and $L(d_0)$ is the path loss measured at distance d_0

III. REALISTIC POWER DATA GATHERING ALGORITHM

The discrete radio model [8] is a technique for simulating the sustainability of the network nodes and calculating the energy consumed for transmission and reception. Nodes have packets of data in each round of communication that need to be gathered and fused with other nodes packet into one packet and get transmitted to distant Base Station. We introduce a radio model discussed in [9], that dynamically determines which power level setting should be used to transmit between two nodes. Using the power level setting, the cost of transmissions is calculated based on the chip specifications to ensure an accurate estimation. We have described a model which operates on the principle of Energy Bands. Discrete order Radio Model works irrespective of distance and number of packets. Traditional radio model mainly focuses on the distance of sensor nodes from Base Station (BS) together with the count of number of hops during transmission, i.e. PEGASIS[4] and also for shortest hop between each communication pair of nodes, i.e. SHORT[6]. It also depends on the number of packets. In reality a transmit power level of the sensor node can only be adjusted to discrete values which may result in single power level for multiple values of distance. We have applied realistic power consumption model over chain based protocol PEGASIS and in shortest hop transmission protocol SHORT. Due to this, the estimated power levels for transmission between nodes can only be used as a starting point.

$$P_{transmit} = V_{remaining} * (I_{ROON} * \tau_{startup} + I_{plevel} * \frac{L}{R}) \dots\dots\dots (2)$$

Where, $V_{remaining}$ = remaining current voltage of the mote, I_{ROON} = Current required for radio oscillator to start. $\tau_{startup}$ = start up time. I_{plevel} = current at a power level. L = packet size, R = rate of transmission.

$$E_{receive} = V_{remaining} * I_R * (L / R) \dots\dots\dots (3)$$

Energy dissipation for reception or transmission is constant for a particular power level. Initial Energy = E_i

$$E_T * R_1 + E_R * R_2 = E_i \dots\dots\dots(4)$$

The transmit and receive power level is selected from the Fig 1 which provides energy consumed in transmission of 100 byte packet considering the different power levels used by CC2420. We have neglected power level 15 as it has a power output of -7dbm and simulations yields that the distance of operation of this power level is so close to power levels 11 and 19 such that it becomes meaningless to take this

power level in the context of number of packets of energy sent in the simulations. The number of packets sent in one transmission is taken to be as 5. So a total of 500 bytes are sent.

TABLE I

FND: First node dies, LND: Last Node Dies

Data gathering Scheme (For 100 sensors)	Initial Energy (mJ)	Network Lifetime (No of rounds)			
		Discrete radio Model		First Order Radio Model	
		FND	LND	FND	LND
PEGASIS 50m x 50m square field	250	130	570	190	666
	500	250	1164	400	1434
	1000	505	2259	750	3371
PEGASIS 100m x 100m square field	250	205	541	75	599
	500	400	1146	110	1325
	1000	520	2254	250	2769
SHORT 50m x 50m square field	250	232	330	540	550
	500	430	630	1100	1145
	1000	855	1250	2210	2370
SHORT 100m x 100m square field	250	230	315	540	565
	500	450	590	855	900
	1000	850	1200	1750	1795
LBEERA 50m x 50m square field	250	125	413	280	566
	500	250	810	560	1110
	1000	500	1620	900	2225
LBEERA 100m x 100m square field	250	390	1590	560	1420
	500	97	380	82	360
	1000	190	790	230	710

As most data dissemination algorithms depend upon a centralized base station configuration we will focus upon these types of networks. This network configuration provides some major advantages for discrete power level selection. Firstly, only the base station needs to track and store which nodes can communicate and at which power levels. This frees up memory and storage space, which is limited on each mote, allowing for more data aggregation to occur or storing more data before transmitting it back to the base station. Secondly, with a centralized configuration the base station will know the exact power levels of each mote are using for transmitting and therefore the exact power cost. In order to select the best power levels in a real world deployment we propose that a network initialization period is used. In this period, each mote takes a turn and broadcasts a packet at each power level with the assigned mote id and the transmission power level being used. Each other mote in the network will

listen for the packet and track the lowest power that can be used for communication from that mote. Once every mote has participated in the initialization period, they generate a packet containing their mote id and an array of incoming packet information. This incoming packet information will contain the incoming mote id, lowest received power level and the associated RSSI. This packet is transmitted to the base station for storage and processing, which relieves the mote from storing the information. With this information at the base station, the data dissemination algorithms can be optimized for the exact costs and the base station can dictate which power levels should be used when it broadcasts schedules to motes in the network.

In this paper, we investigate the combination of several data gathering techniques into a single model that will be more realistic and useful for simulations. We have investigated the performance over chain formation, PEGASIS [4] and shortest hop data gathering

IV SIMULATION RESULTS

We have simulated a comparative result of Network Lifetime for the first order radio model and discrete radio model. The sustainability of the network during trail rounds is compared for different initial energy in case of PEGASIS as shown in table II. To analyze the system performance for the conventional first order radio model which assumes the ideal condition and discrete radio model we have considered a square network area of dimension 50m x 50m,(small network) and 100m x 100m(large network) all for PEGASIS ,SHORT and LBEERA [12]as shown in Table I.

Table : II

Data gathering Scheme for 100 sensors	Initial Energy (mJ)	Network Lifetime (no of rounds) for remaining 10 mJ of Mean energy of the Network	
		Discrete radio Model	First order radio Model
PEGASIS 50m x50m square field	100	120	60
	250	275	170
	500	590	400
	1000	850	600

A comparative result in Table II shows that in case of PEGASIS we can replace the node during the trails periods of network sustainability.

V. CONCLUSION

In this paper, we have proposed an algorithm called Realistic Power Data Gathering Algorithm for collecting useful data at different power levels from a remote wireless sensor network to the BS. Utility of the network for node replacement and longer trailed

lifetime is observed .Discrete radio model is our future model which gives more realistic view.

REFERENCES

- [1] Lindsey S., Raghavendra C.S., and Sivalingam K.,“Data Gathering in Sensor Networks using energy*delay metric,”in Proceedings of the 15th International Parallel and Distributed Processing Symposium, (2001),pp.188-200
- [2] W. Heinzelman, A. Chandrakasan, H. Balakrishnan, “Energy-Efficient Communication Protocol for Wireless Microsensor Networks”, *IEEE Proc. Of the Hawaii International Conf. on System Sciences*, pp. 1-10,January 2000.
- [3] T. Shepard, “A channel access scheme for large dense packet radio networks,” in *Proceedings of ACM SIGCOMM Conference*, pp. 219 - 230, Aug. 1996.
- [4] Lindsey, S.Raghavendra, C.S,“PEGASIS: Power Efficient Gathering in Sensor Information Systems,” in Proceedings of IEEE ICC 2001 (2001) 1125-1130.
- [5]Ayan Acharya, Anand Seetharam, Abhishek Bhattacharyya, Mrinal Kanti Naskar, “Balancing Energy Dissipation in Data Gathering Wireless Sensor Networks Using Ant Colony optimization”, *10th International Conference on Distributed Computing and Networking-ICDCN 2009*, pp437-443, January 3-6, 2009.
- [6]Yang, Y., Wu, H.H., Chen, H.H., “ SHORT: Shortest Hop Routing Tree for Wireless Sensor Networks”, IEEE ICC 2006 proceedings , (2006).
- [7] Ayon Chakraborty, Swarup Kumar Mitra, and M.K. Naskar, “An Efficient Hybrid Data Gathering Scheme in Wireless Sensor Networks”, ICDCIT 2010, LNCS 5966, pp. 98–103, 2010.
- [8] M. Mallinson, P. Drane, and S. Hussain “ Discrete Radio Power Level Consumption Model in Wireless Sensor Networks,Mobile Adhoc and Sensor Systems,” 2007.MASS 2007. IEEE International Conference on 2007, pp. 1-6.
- [9] Michael Mallinson, Patrick Drane, and Sajid Hussain.,“Discrete radio power level consumption model in wireless sensor networks, in Second International Workshop on Information Fusion and Dissemination in Wireless Sensor Networks (SensorFusion),” 2007.
- [10] Chipcon AS. *Chipcon SmartRF CC2420, 2.4 GHz IEEE 802.15.4 / ZigBee-ready RF Transceiver*, 2006.
- [11]Asraf Hossain , P.K.Biswas,S.Chakrabarti, “Sensing Model and Its Impact on Network Coverage in Wireless Sensor Network,” in proceedings of the 10th Colloquium and The third ICIS, Kharagpur, India 2008
- [12] Yu1, Y., Wei, G,“Energy Aware Routing Algorithm Based on Layered Chain in Wireless Sensor Network”, 1-4244-1312-5/07/\$25.00 © 2007 IEEE.

MLSAR Analysis in a Realistic Grounded Human Head Model for a Dipole Antenna using FDTD method at 930 MHz

Md.Faruk Ali¹

Dept. of Electronics and Telecommunication Engineering
Bengal Engineering and Science University
Shibpur, Howrah-711 103, India
¹faruk_ali@rediffmail.com

Santanu Mondal² and Sudhabindu Ray³

Dept. of Electronics and Telecommunication Engineering
Jadavpur University
Jadavpur, Kolkata-700 032, India
²santanumondal2008@rediffmail.com
³sudhabin@etce.jdvu.ac.in

Abstract— Specific absorption rate (SAR) induced inside a realistic grounded human head model for a half-wave radiating dipole antenna has been computed at the frequency of 930 MHz using finite difference in time domain (FDTD) method. The head is modeled using freely available voxel based anthropomorphic Zubal phantom data considering the electrical parameters of different anatomical internal structures of the human head. Effects of variation of distance (D) measured from the end of antenna side on Maximum Local SAR (MLSAR) induced in the head model have been investigated for a set of gap (d) between the antenna and head. The value of MLSAR becomes more than the ANSI/IEEE's upper safety limit for the distance between the head and antenna less than 0.8 cm and 0.6 Watt radiated power.

Keywords- FDTD method, MLSAR, real human head model.

I. INTRODUCTION

In the recent years, cellular telephones and mobile wireless communication systems are being introduced into society at a very rapid rate. The Electromagnetic (EM) waves radiated from these devices interact with the head and other parts of human body and cause radiofrequency (RF) health hazards. Safety guidelines for RF health hazards are set in terms of SAR [1]. It is defined as the rate at which a person absorbs EM energy per unit mass. Localized SAR averaged over 1-g of tissue i.e. peak 1-g SAR not exceeding 1.6 W/kg is recommended by IEEE/ANSI as the upper safety limit [2].

It is difficult to experimentally measure SAR or EM field distributions inside human body. Therefore, various numerical techniques played significant roles to calculate these quantities. FDTD method [3] is one of the widely used technique to simulate the EM field distributions in three dimensional structures. Calculation of SAR in human head using FDTD method is reported in several research papers [4-10]. Recently the MLSAR has been studied for a three layered inhomogeneous spherical human head model consisting of skin, skull and brain [5-6]. In another study three human head models, a box model, a spherical model and a realistic model have been used to investigate peak SAR at 915 MHz and the result shows that the SAR values obtained with box or

spherical head models are greater than those for a realistic head model [8]. Calculation of peak 1-g SAR in the three MRI-based human head models of different ages consisting of fifteen types of tissues due to exposure to EM waves emitted from two different lengths of the monopole antennas has been reported at 835 MHz and 1900 MHz which shows that the value of peak 1-g SAR is larger for smaller head models of children [9]. Calculation of peak 1-g and 10-g SAR in a MRI based human head model consisting of eighteen types of tissues in the frequency range of 900 MHz to 2.45 GHz for $d = 1.2$ cm has also been reported [10].

In this paper, MLSAR has been computed using FDTD method in a realistic grounded human head model based on CT scan data for a set of d in the range of 0.4 cm to 1.2 cm and plotted against D . The head model is consisting of twenty two types of tissues and exposed to EM waves radiated from a half-wave dipole antenna at 930 MHz. FDTD code is developed to implement the head model along with a dipole antenna to calculate MLSAR using MATLAB [11].

II. MODEL AND METHOD FOR ANALYSIS

A. Human Head Model

The human head model used in this study is obtained from freely available voxel based anthropomorphic Zubal phantom data considering the electrical parameters of different anatomical internal structures of the human body. The head model has been reconstructed from the Zubal head and torso data. The Zubal head and torso data is based on CT imaging sequence of a 35 year old male weighing 155 lbs and measuring 5'10" in height and is freely available in the public domain [12]. An in-house MATLAB program has been developed to read the slices from original CT scan data file. To simplify the numerical calculations, the other parts of the human body except the head are excluded in the simulation. Geometry of the human head model along with the dipole antenna is shown in Fig. 1. The head is comprised of twenty two types of tissues; i.e., brain, cerebellum, skin, bone, muscle, fat, lense, eyeball, tongue, blood, cartilage, CSF, parotid gland, retina, teeth, trachea, spinal chord, nerve, eye sclera, bone

marrow, pituitary gland and mouth cavity/sinuses. Values of relative dielectric constant (ϵ_r), conductivity (σ) at 930 MHz and mass densities (ρ) of the respective head tissues used in the simulation are obtained from literature [13] and are listed in TABLE I.

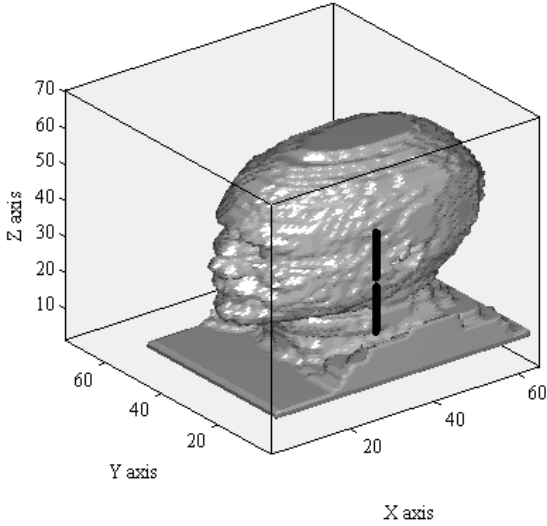


Figure 1. Geometry of human head model along with dipole antenna used in the simulation.

B. Ground Plane

As a human head floating in free space is not a realistic situation so in order to approach towards a practical condition a ground plane is added under the human head model.

TABLE I.
DIELECTRIC CONSTANT (ϵ_r), CONDUCTIVITY (σ) AND MASS DENSITY (ρ) OF THE HUMAN HEAD TISSUES AT 930 MHZ

Tissue Type	Dielectric Constant (ϵ_r)	Conductivity σ (S/m)	Mass Density ρ (Kg/m ³)
Brain	50.6800	0.9295	1030
Cerebellum	57.5980	1.0020	1030
Skin	48.0980	0.6657	1010
Bone	13.2700	0.0869	1850
Muscle	57.5960	0.7834	1040
Fat	5.6000	0.0403	920
Lense	48.4900	0.6580	1100
Eyeball	74.1000	1.9700	1010
Tongue	58.2090	0.7590	1040
Blood	64.8200	1.3320	1000
Cartilage	46.0430	0.5690	1100
CSF	71.7090	2.2380	1010
Parotid gland	49.6000	1.0300	1050
Retina	58.2090	0.9899	1020
Teeth	13.2770	0.0869	1850
Trachea	44.6850	0.6237	1040
Spinal chord	36.0650	0.4329	1040
Nerve	36.0650	0.4329	1040
Eye sclera	58.2090	0.9899	1030
Bone marrow	5.7099	0.0283	1000
Pituitary gland	55.2200	1.0000	1040
Mouth cavity or sinus	1.0000	0.0000	1.200

C. DTD Method

The FDTD method has been used to investigate the interactions between the human head model and EM waves radiated from a half-wave dipole antenna. The parameters used for FDTD computation are as follows. A space domain enclosing head model and dipole antenna is consisting $65 \times 74 \times 70$ Yee cells. Each Yee cell has a dimension of $0.4 \text{ cm} \times 0.4 \text{ cm} \times 0.5 \text{ cm}$. The time step (δt) used in this simulation is limited by Courant stability criterion:

$$\delta t \leq \frac{\sqrt{\left(\frac{1}{\delta_x^2} + \frac{1}{\delta_y^2} + \frac{1}{\delta_z^2} \right)}}{c} \quad (1)$$

where, c is the speed of light in free space and $\delta_x = \delta_y = 0.4 \text{ cm}$ and $\delta_z = 0.5 \text{ cm}$. To absorb the outgoing scattered waves, 5-point unsplit step 3-D Perfectly Matched Layer (PML) has been used as the absorbing boundary [14].

D. Antenna Model

A dipole antenna made with aluminum having length (L) of 14.5 cm and width of 0.4 cm is chosen as the radiating element. Frequency dependent reflection coefficient $S_{11}(f)$ of the dipole antenna is determined from the ratio of the Discrete Fourier Transform (DFT) of incident and reflected waveforms [6]:

$$S_{11}(f) = \frac{DFT[E_{ref}]}{DFT[E_{inc}]} \quad (2)$$

where, E_{inc} = incident electric field and E_{ref} = reflected electric field.

S_{11} is computed in dB by:

$$S_{11} = 20 \log_{10}(|S_{11}|) \quad (3)$$

E. SAR Calculations

From the converged solutions the local SAR at (i, j, k) th cell inside the head is obtained from the following equation [10]:

$$SAR(i, j, k) = \frac{\sigma(i, j, k) |\hat{E}(i, j, k)|^2}{2\rho(i, j, k)}$$

$$= \frac{\sigma(i, j, k) \left\{ |\hat{E}_x(i, j, k)|^2 + |\hat{E}_y(i, j, k)|^2 + |\hat{E}_z(i, j, k)|^2 \right\}}{2\rho(i, j, k)}$$

(W/Kg) (4)

where, \hat{E}_x , \hat{E}_y and \hat{E}_z are the peak values of the electric-field components (V/m), σ = conductivity of the head (S/m) and ρ = mass density of the head tissues (Kg/m³). During calculation of SAR the excitation source voltage (V) applied at the feeding

point of the dipole antenna is obtained by the following equation [15]:

$$V = \sqrt{P \times 8 \times R} \quad (5)$$

where, $P = 0.6$ Watt and $R = 50 \Omega$. MLSAR is obtained by finding the maximum value of SAR within the whole head model at each value of D for d in the range of 0.4 cm to 1.2 cm.

III. RESULTS AND DISCUSSIONS

Variation of S_{11} with frequency for the half wave dipole antenna of length 14.5 cm placed in free space is obtained using MATLAB and compared with that obtained using FIDELITY as shown in Fig. 2. The curve obtained using the MATLAB program is in close agreement with that obtained from FIDELITY. At the fundamental mode, the antenna resonates at 930 MHz and the value of S_{11} remains below -10 dB within GSM 900 band. Values of S_{11} at the fundamental resonance frequency obtained from MATLAB program and FIDELITY are -14.14 dB and -15.17 dB, respectively.

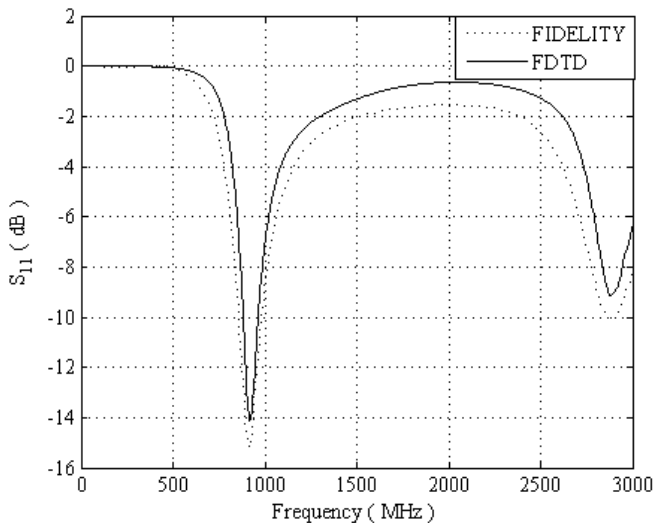


Figure 2. Variation of S_{11} with frequency for the half wave dipole antenna of length 14.5 cm placed in free space.

Fig. 1 illustrates the geometry of a grounded realistic human head model along with a dipole antenna used for the simulation by FDTD to calculate MLSAR. The human head is composed of 1,51,200 Yee cells of dimension: $0.4 \text{ cm} \times 0.4 \text{ cm} \times 0.5 \text{ cm}$. MLSAR vs. D obtained for $L = 14.5$ cm and d equal to 0.4 cm, 0.8 cm, and 1.2 cm is shown in Fig. 3. When d is equal to 0.4 cm then the value of MLSAR is 2.06 W/kg, above ANSI/IEEE's upper safety limit 1.6 W/kg [2]. As d increases over 0.8 cm then the value of the MLSAR goes below the upper safety limit. For each value of d , value of MLSAR increases towards the direction of antenna side and decreases significantly away from the antenna side due to smaller penetration of EM waves through the head model.

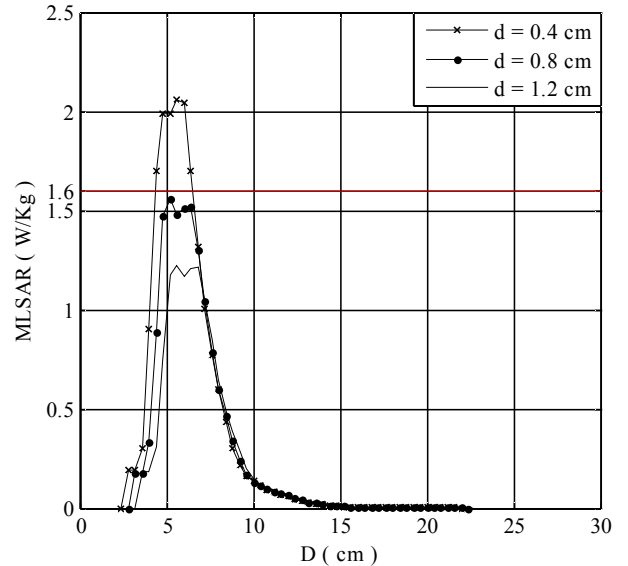


Figure 3. MLSAR vs. D induced in the human head model for a set of d in the range of 0.4 cm to 1.2 cm at 930 MHz.

IV. CONCLUSIONS

MLSAR induced in a CT-scan based human head model consisting of twenty two types of tissues have been studied using FDTD method. A half-wave resonant dipole antenna of length 14.5 cm has been used as EM source. Variation of MLSAR with distance D measured from the end of the antenna side at the frequency of 930 MHz has been obtained for a set of distance d between the radiating dipole antenna and the head in the range of 0.4 cm to 1.2 cm. MLSAR induced in the head model is found to be more than the ANSI/IEEE's upper safety limit for the distance between head and dipole antenna less than 0.8 cm for input power of 0.6 Watt.

REFERENCES

- [1] H. Shabani, Md. R. Islam, AHM Z. Alam and H. E. Abd EI-Raouf, "EM Radiation from Wi-LAN Base Station and Its' Effects in Human Body," *5th International Conference on Electrical and Computer Engineering 2008, Dhaka, Bangladesh*, pp. 86-91.
- [2] *American National Standard – Safety Levels with Respect to Exposure to Radio Frequency Electromagnetic Fields, 3 kHz to 300 GHz*, ANSI/IEEE C95.1 - 1992.
- [3] K. S. Yee, "Numerical solution of initial boundary value problems involving Maxwell's equations of isotropic media," *IEEE Trans. Antenna Propagation.*, vol. APT- 14, pp. 302-307, 1966.
- [4] D. G. Choi, C. S. Shin, N. K. Kim and H. S. Shin, "Design and SAR analysis of Broadband PIFA with Triple Band," *Progress in Electromagnetics Research symposium 2005, Hangzhur, China*, pp.22 – 26, August-2005.
- [5] Md. Faruk Ali and Sudhabindu Ray, "SAR Analysis on Human Head Exposed to Radiating Dipole Antenna for 500 MHz – 5 GHz Frequency Band Using FDTD Method," *National Conference on Communications. 2008, IIT Bombay, India*, pp. 481-485.
- [6] Md. Faruk Ali and Sudhabindu Ray, "SAR Analysis in a Spherical Inhomogeneous Human Head Model Exposed to Radiating Dipole Antenna for 500 MHz – 3 GHz Using FDTD method," *International*

- Journal of Microwave and Optical Technology*, vol. 4. No.1, pp. 35-40, January -2009.
- [7] N. Homsup and W. Homsup, "FDTD Simulation of a Mobile Phone Operating Near a Metal Wall," *Journal of Computers*, vol. 4, No. 2, Feb. 2009.
- [8] Michal Okoniewski and Maria A. Stuchly, "A Study of the Handset Antenna and Human Body Interaction," *IEEE Trans. Microwave Theory Tech.*, vol. MTT – 44. No.10, pp.1855-1864, October-1996.
- [9] O. P. Gandhi, Gianluca Lazzi and Cynthia M. Furse, "Electromagnetic Absorption in the Human Head and Neck for Mobile Telephones at 835 and 1900 MHz," *IEEE Trans. Microwave Theory Tech.*, vol. MTT – 44. No.10, pp.1884-1897, October-1996.
- [10] A. Hirata, M. Morita and T. Shiozawa, "Temperature increase in the human head due to a dipole antenna at microwave frequencies", *IEEE Trans. Electromagnetic Compatibility*, Vol. 45, pp. 109-116, Feb. 2003.
- [11] Matlab 7.1, The MathWorks, Inc. <http://www.mathworks.com>.
- [12] The Zubal Phantom data, MRI Head Phantom Data Description. <http://noodle.med.yale.edu/phantom/getmridesc.htm>
- [13] Dielectric Properties of the Human Body tissue in the Frequency Range of 10 Hz-100GHz. <http://niremf.iroec.fcnr.it/tissprop>.
- [14] D. M. Sullivan, "An Unsplit Step 3-D PML for use with the FDTD method," *IEEE Trans. Microwave Theory Tech.*, vol. MTT – 7. No.7, pp.184-186, July-1997.
- [15] H. Y. Chen and K. Y. Shen, "Reduction of SAR in a Human Head model wrapped in clothing Materials," *Microwave and Optical Technology Letter*, vol. – 37. No.4, pp.305-308, May-2003.

A Brief Review of Energy Absorption in the Human Body and its Effects

Sayantana Dhar, Arkaprov Das and Sonali Das

Department of Electronics and Tele-Communications Engineering,
Jadavpur University, Kolkata 700 032, India

sayan.dhar@gmail.com, arka_reek@yahoo.co.in, sonali_das1234@yahoo.com

Abstract - The phenomenal increase of wireless setup has raised concerns over the effect of non-ionizing radiation on public health. In a world where the human – antenna interaction is increasing on a daily basis we have to be vigilant about any adverse health effects it might cause. This paper tries to unravel the biological concerns involving non-ionizing radiation. Technologies which require attention for their effects on the human body are also discussed. Finally some discussions on what future developments promise are presented.

I. INTRODUCTION

Radio communications has been in use for more than a century since the successful demonstration of wireless communication by Guglielmo Marconi in 1895. It has since then been used in a myriad of applications like radio broadcasting, television, radar, mobile communications, etc. Due to the technological advancements in digital and RF circuitry [1] at large, mobile radio communications have grown at a phenomenal rate in the past few decades. With hand-held mobile telecommunications equipment seeing an exponential growth, the technological advancements too have been evolving alongside. Now with mobile equipment flooding the consumer market, an electromagnetic radiating device is being used at close proximity with the body for long periods of time. It has been common knowledge that high doses of electromagnetic radiation is detrimental to health [2]. There have been concerns over the effects of E.M. radiation for quite a few years now like “Does the use of mobile phones for a long period cause brain tumours?” When a person is exposed to the radio waves from mobile phones or base stations, most of the energy will be reflected by the body or be diffracted. Some of the energy however, will be absorbed by tissues at the surface of the body. Inside, the water molecules will start to move or rotate due to the presence of the electromagnetic fields. This resonance effect converts the energy into heat [3]. If the radio wave intensity is very high, the heating may be significant and potentially detrimental. This paper tries to provide a holistic approach to the problems on electromagnetic absorption in human body the methods commonly used to compute the specific absorption rate and discusses the biological effects pertaining to EM radiation. Intense research work is being done on the possible biological hazards resulting from over-exposure to Radio Frequency (RF) and microwave energy. In 1996 WHO established a

program to review the biological effects concerning electromagnetic fields [4].

II. ENERGY ABSORPTION INSIDE THE BODY AND SPECIFIC ABSORPTION RATE

In today’s evolving technological world, the rapid advancement of the wireless communications has meant that we are constantly exposed to electromagnetic waves. In an urban scenario there are waves radiated by radio and TV broadcasters in the VHF and UHF range, cellular phone operators operating in the 900 MHz to 2450 MHz range. Our cause of concern is the potential threat to public health as a result of exposure to RF waves and Microwaves [5]. The rate at which RF energy is absorbed by the body when exposed to radio-frequency electromagnetic field is a measure of the Specific Absorption Rate (SAR). SAR is a dosimetric quantity and is defined as the power absorbed per mass of tissue and has units of watts per kilogram and is given by

$$SAR = \frac{\sigma |E|^2}{\rho} \quad (1)$$

where E is the electric field intensity of the electromagnetic wave in the tissue, σ and ρ are the conductivity and density of the tissue respectively, of the human body organ under examination. In order to estimate the risk caused by the use of wireless devices on different parts of the body, the following parameters are usually established:

1. a maximum SAR or local peak SAR,
2. a whole body average SAR,
3. a maximum 1 gram average SAR, and
4. a maximum 10 gram average SAR

Guidelines for human exposure to RF fields are based on SAR thresholds where adverse biological effects may occur. When the human body is exposed to an RF field, the SAR experienced is proportional to the squared value of the electric field strength induced in the body. SAR limits are specified for both whole-body exposure and for partial-body or localized exposure (generally specified in terms of spatial peak values). To ensure protection of the general public against EM radiation several countries have mandated standards and guidelines on the amount of radiation that the public can be exposed to. In most countries standard and regulatory bodies and even independent organizations like Institute of Electrical and Electronic Engineers [6] (IEEE), Federal Communications Commission [7] (FCC), the National Council on Radiation Protection and Measurements [8]

(NCRP), the International Committee on Non-Ionizing Radiation Protection [9] (ICNIRP) and Association of Radio Industries and Business [10] (ARIB) have recommended exposure guidelines for the general public as well as for RF workers in their course of duty. These standards also specify the Maximum Permissible Exposure (MPE) as the maximum power densities associated with the electric and magnetic fields that a human can be exposed to within the safety limit. Appendix I and II list the recommended limits for the maximum radiation exposure adopted by different organizations and SAR limits adopted by different countries.

III. METHODS USED TO COMPUTE SAR

One of the most difficult problems associated with the determination of energy absorption is that of obtaining samples. Because of ethical considerations we cannot irradiate live humans with electromagnetic energy, instead it is more convenient to simulate a human using computer models. The key factor is to assess how much energy is absorbed and where it is deposited. From (1) we observe that the localized SAR is directly proportional to the square of the internal electric field. Thus our focus is to calculate the electric field distribution within the biological body. However, these fields are difficult to calculate as they depend on a number of factors such as the nature of the field (near field or far field), the dielectric parameters of the body, the dimension of the body, etc. The mathematical techniques essentially involve solving the Maxwell's equations for accurate representation of the body [11-14]. Numerical modeling of the human body has generally revolved around two techniques: the Method of Moments (MoM) which is mostly a frequency domain method and the Finite Difference Time Domain Method (FDTD) which is a time domain method.

There are numerous numerical phantoms which simulate the characteristics of a human body for theoretical analyses and computational simulations. In theoretical analyses, simple-shaped phantoms are generally used. These types are called theoretical phantoms. However, in order to calculate the characteristics of antennas close to the human body, it is necessary to use a more realistic numerical phantom, which is composed of many VOXELs (VOlumetric piXEL). There are also physical models simulating the characteristics of the biological tissues called physical phantoms as shown in Fig. 1 [15]. The interaction of EM waves radiated from the mobile phone and the human head using analytical phantoms have been a favored topic of research lately [16-18]. Works involving physical phantom models are gaining popularity off late.



Fig.1 Realistic Phantom model of a human torso

IV. SOURCES OF NON-IONIZING RADIATION AFFECTING THE HUMAN BODY

In this section we concentrate on those sources of non-ionizing radiation which are usually placed in very close vicinity to the human body.

A. Mobile Phones

Since the wireless revolution the mobile phone has seen tremendous penetration into the daily lives of people. It is a potent source of microwave radiation which is kept at very close proximities to the human body at all times. Now with passage of time more and more research is being performed on the potential ill effects of mobile phone radiation.

Many scientific studies have investigated possible health effects of mobile phone radiation. These may be categorized into two broad categories - Thermal and Non-thermal effects. The thermal effect deals with dielectric heating i.e. rotation of polar water molecules in our body causing heat energy. Body parts which have low blood supply are most affected by the thermal effect. The eyes and testes are prime examples.

The non-thermal effects are mainly described as effects when the interaction of electric or magnetic fields of RF radiation with the human body produces effects apart from heating [19]. On similar lines, researchers at Lund University, Sweden have found that irradiating a rat's brain with microwave radiation for about 2 hours releases protein into the brain via a permeated blood-brain barrier [20-21].

The ever increasing use of mobile phones has also prompted questions such as "Do cell phone radiations cause cancer?" Projects such as INTERPHONE [22] have tried to answer these questions by analyzing data from patients suffering from glioma (cancer in the brain or spine) and meningioma (another type of brain tumor) in the age group of 30-59 years. Their long term epidemiological study proved inconclusive. However, there was some evidence that very high users experienced excess risk of glioma. Similar studies are being performed today to probe further into the link between cancer and cell phone usage.

In December 2004 [23], a pan-European study involving 12 collaborating laboratories in several countries showed some compelling evidence of DNA damage of cells in in-vitro cultures, when exposed between 0.3 to 2 watts/kg, whole-sample average. There were indications, but not rigorous evidence of other cell changes, including damage

to chromosomes, alterations in the activity of certain genes and a boosted rate of cell division.

B. Implanted Antennas

With advances in engineering technology, the boundaries between core engineering and other fields are fast disappearing. There is an increasing trend to utilize radio frequency antennas inside/outside a human body for diagnosis and therapeutic purpose. Most of the research on antennas for medical applications has focused on producing hyperthermia for medical treatments and monitoring various physiological parameters [24]. Antennas used to elevate the temperature of cancer tissues are located inside or outside of the patient's body, and the shapes of antennas used depend on their locations. Furthermore, remote health care monitoring is slowly turning into a reality with improvements in wireless technology in bio-medical applications. For implantable communication links between implanted antennas inside a human body and exterior antennas in free space, implanted antennas are located in biological tissues in two ways – direct contact or indirect contact [25].

The direct contact method involves the antenna directly in contact with a biological tissue whereas, in the indirect contact method, the antenna indirectly contacts a biological tissue using a buffer layer. The buffer layer can be an air region or a dielectric material. Although the antenna in direct contact requires less amount of space it generates a significant amount of SAR within the body which is a cause of concern.

Recently, a Swiss medical device company has developed contact lens fitted with an antenna which can pick up slight changes in ocular pressure and delivers the data wirelessly to a data recorder as shown in Fig. 2 [26]. Although the use of such devices aid doctors to monitor a patient's glaucoma condition it still exposes the eye to RF radiation. The human eye having very little blood vessels runs the risk of heating up quickly. Increase of the eye's temperature by 4°C increases the risks of cataracts. Careful studies of SAR levels need to be performed before RF antennas are placed inside the human body.



Fig. 2 A person wearing a diagnostic contact lens

V. BIOLOGICAL CONCERNS

For quite some time now, researchers have been engaged in a controversy over the possible hazards of non-ionizing

electromagnetic radiation and possible thermal effects [4,5, 12, 27-33]. It has been known for many years that exposure to high levels of RF radiation can be harmful due to its ability to heat biological tissue rapidly. As a consequence of the non-uniform energy deposition produced by EM fields, it is also possible that localized temperature increases, so-called "hot-spots" without affecting the overall temperature of the body. However, localized temperatures above 41.6°C can cause protein denaturation, increased permeability of cell membranes, or the liberation of toxins in the location where the hot-spot exists. The severity of the resultant physiologic effect produced localized temperature increases can be expected to be worsened in critical organs, such as the brain. The human eye is one of the most sensitive organs for EM wave exposure so there have been numerous research papers on the effects of EM radiation on the eye [28, 34-35]. Lin [34-35] has investigated the effects of RF and microwave radiation on the eyes. In his study he finds that a temperature of 41°C behind the lens induces cataracts in rabbits. Furthermore, he observes that "hot spots" or regions of SAR maxima tend to appear in the interior of the eyeball with decreasing frequency and concludes by saying that within exposure guidelines cataract formation in humans is improbable. A more thorough work on the temperature rise in the eye over a range of frequencies has been discussed in [36]. The effects of temperature rise in the human head when irradiated with microwave frequencies has also been investigated [37]. These works are indicative of the fact that radiation from mobile phones is not harmful due mainly to the low power that they radiate.

There are however, viable concerns surrounding the power radiated from the base station especially for people staying close it. The signal from a cellular base station antenna is essentially directed toward the horizon in a relatively narrow pattern in the vertical plane. As with all forms of electromagnetic energy, the power density from a cellular transmitter decreases rapidly (according to an inverse square law) as one moves away from the antenna. Consequently, normal ground-level exposure is much less than exposures that might be encountered if one were very close to the antenna and in its main transmitted beam. When cellular antennas are mounted at rooftop locations it is possible that RF levels greater than the norm maybe present on the rooftop itself. But rooftop cellular antennas usually operate at lower power levels than antennas on free-standing towers. In addition, the significant signal attenuation of a building's roof minimizes any chance for persons living or working within the building itself to be exposed to RF levels that could approach or exceed applicable safety limits.

VI. SUMMARY

In spite of our best efforts, review of such a huge realm as envisaged here is bound to remain incomplete. However, from this review work, it is understood that there are several critical issues to be considered while designing antennas that are electromagnetically safe to humans. Various techniques used for SAR computations and biological concerns involving EM

radiations were discussed. Although FDTD method is the most acceptable method for evaluating SAR with a high degree of resolution, it is still not a complete model to predict the energy deposition within the body. Physical phantoms are recently gaining popularity as they can represent realistic models of the adult human body for SAR calculations. With increasing dependence of people on cellular phones there exists a constant threat from over exposure to RF radiation. The link between cell phone usage and cancer can be better understood with passage of time. Since an epidemiological study involves decades of research, it is perhaps a bit early to write off the adverse effects of cell phone radiation.

Key biological concerns have been listed as a holistic list was not possible to incorporate here. Though dependence of SAR on the permittivity of a body was highlighted; but few literatures are available on this subject. Tissue specific dielectric variation and the change in the permittivity values with increase in temperature could be investigated. Also localized temperature increase in brain tissues could also be a subject of scrutiny. An area which has also been overlooked is the effect of transient fields in the human body, most reports present in literatures deal with steady state conditions. Since transients can cause havoc on electrical circuits it would be interesting to study the effect of these fields on the human body. Prolonged effects of magnetic field from a cell phone on brain activity are also to be addressed. Also, during MRI scan, where the human body is exposed to strong magnetic field, research needs to be carried out to study the effect of these magnetic fields on the brain activity.

Finally, with the revolutionized increase of telecommunication industry in India over the last two decades, mobile users have been demanding higher data rates and high speed internet access on the go. Wireless network providers have to tap into higher frequencies of the EM spectrum to meet the needs resulting in installation of many more base stations. This will expose the public to more EM waves and the exposure guidelines for public safety might be exceeded. Thus, there is a need for periodic evaluation of SAR to maintain it within specified acceptable limits. But, in a country as huge as ours, we are yet to finalize upon any SAR limits recommended by the government. This is an issue which must be addressed as quickly as practicable since the health of millions of people are at stake.

ACKNOWLEDGMENTS

We express our sincere thanks to Prof. Bhaskar Gupta and Mr. S. Sankaralingam of Department of Electronics and Tele-Communication Engineering, Jadavpur University, Kolkata for encouraging us to take up this work.

REFERENCES

- [1] T.S. Rappaport, *Wireless Communications Principles and Practice*, second edition. Prentice Hall, New York, 2005
- [2] Chris Zombolas, "Specific Absorption Rate (SAR) New Compliance Requirements for Mobile and portable RF Telecommunications Equipment", Technical Report, EMC Technologies, 2003
- [3] Internet resource, *Radio waves and Health: Mobile communications*. 2006, <http://www.ericsson.com>
- [4] *Federal Communications Commission Office of Engineering & Technology. Questions and Answers about Biological Effects and Potential Hazards of Radiofrequency Electromagnetic Fields*, OET Bulletin 56, Fourth Edition, 1999
- [5] M. A. A. Karunarathna and I. J. Dayawansa, "Energy absorption by the human body from RF and microwave emissions in Sri Lanka", *Sri Lankan Journal of Physics*, Vol. 7, 35-47, 2006
- [6] *IEEE Standards C95.1-1991, IEEE Standard for Safety Levels with Respect to Human Exposure to Radio Frequency Electromagnetic Fields, 3 kHz to 300 GHz*, New York, 1999
- [7] *FCC OET Bulletin.65, Evaluating Compliance with FCC Guidelines for human exposure to Radio Frequency Electromagnetic Fields*, Washington D.C., 1997
- [8] *NCRP Report 86, Biological Effects and Exposure Criteria for Radio Frequency Electromagnetic Fields*, Bethesda, MD, 171-174, 1986
- [9] *INCIRP Guidelines, "Guidelines for limiting Time-Varying Electric, Magnetic, and Electromagnetic Fields (up to 300GHz)*, Health Physics, 74, 1998
- [10] *ARIB Std. - T56, Specific Absorption Rate (SAR) Estimation for Cellular Phone*, Version 1.0, 1998
- [11] R. J. Spiegel, "A Review of Numerical Models for Predicting the Energy Deposition and Resultant Thermal Response of Humans Exposed to Electromagnetic Fields", *IEEE Trans. on Microwave Theory & Techniques*, vol. MTT-32, No. 8, pp. 730-746, 1984
- [12] C.H.Durney, "Electromagnetic dosimetry for models of humans and animals: A review of theoretical numerical techniques," *Proc. IEEE*, vol. 68, No. 1, pp. 33-40, 1980
- [13] O.P.Gandhi, "State of the knowledge for electromagnetic absorbed dose in man and animals," *Proc. IEEE*, vol. 68, No. 1, pp. 24-32, 1980
- [14] A. W. Guy, M. D. Webb, and C. C. Sorenson, "Determination of power absorption in man exposed to high frequency electromagnetic fields by thermographic measurements on scale models," *IEEE Trans. Biomed. Eng.*, vol. BME-23, no. 3, pp. 361-371, 1976
- [15] P.S. Hall and Y. Hao, "Antennas and Propagation for Body-Centric Wireless Communications", Illustrated edition, Artech House, 2006
- [16] S. Watanabe, M. Taki, T. Nojima and O. Fujiwara, "Characteristics of the SAR Distributions in a Head Exposed to Electromagnetic Fields Radiated by a Hand-Held Portable Radio", *IEEE Trans. Microwave Theory Tech.*, vol. 44, no. 10, pp. 1874-1883, 1996
- [17] H. Shabani, R. Islam, AHM Zahirul Alam, H. Essam and Abd El-Raouf, "Development of Analytical Flat Phantom Model for EM Radiation to Evaluate Specific Absorption Rate (SAR) in Human Body", *Proceedings of the International Conference on Computer and Communication Engineering*, May 2008, pp. 1186-1193
- [18] Q. Balzano, M. Y. Kanda, and C. C. Davis, "Specific Absorption Rates in a Flat Phantom in the Near-Field of Dipole Antennas", *IEEE Trans. on Electromagnetic Compatibility*, vol. 48, No. 3, pp 563-568, 2006
- [19] R. Glaser, "Are thermoreceptors responsible for "non-thermal" effects of RF fields?" *Edition Wissenschaft Forschungsgemeinschaft Funk V.G.* 14515 Issue 21, 2005
- [20] G. Salford, Arne E. Brun, Jacob L. Eberhardt, Lars Malmgren, and Bertil R. R. Persson, "Nerve Cell Damage in Mammalian Brain after Exposure to Microwaves from GSM Mobile Phones", *Environmental Health Perspectives*, Vol. 111, No.7, 2003
- [21] Allan H. Frey, "Headaches from Cellular Telephones: Are They Real and What Are the Implications?", *Environmental Health Perspectives*, Vol. 106, No.3, 1998
- [22] The Interphone Study Group, "Brain tumour risk in relation to mobile telephone use: results of the INTERPHONE international case-control study", *International Journal of Epidemiology*, pp. 1-20, 2010
- [23] A project funded by the European Union under the programme Quality of Life and Management of Living Resources, *Risk Evaluation of Potential Environmental Hazards From Low*

Frequency Electromagnetic Field Exposure Using Sensitive in vitro Methods, 2004

[24] Leonard S. Taylor, "Microwave Antenna Implanted in the Human Brain," *IEEE Antennas and Propagation Society Newsletter*, pp. 10-11, October 1980

[25] Y. Rahmat-Samii, J. Kim, *Implanted Antennas in Medical Wireless Communications*, Morgan & Claypool, 2006

[26] Prachi Patel, "Diagnostic Contacts", *IEEE Spectrum Update*, June 2010

[27] D. E. Livesay and K. Chen, "Electromagnetic fields induced inside arbitrary shaped biological bodies," *IEEE Trans. Microwave Theory & Techniques* vol. MTT-22, pp. 1273-1280, 1974

[28] R.M. Edwards and W.G. Whittow, "Applications of a genetic algorithm for identification of maxima in specific absorption rates in the human eye close to perfectly conducting spectacles", *IEE Proc.-Sci. Meas. Technol.*, Vol. 152, No. 3, pp. 89-96, 2005

[29] D. W. Z. Peiyun and Z. Y. L. Changhong, "Study on Human Head/Antenna Interactions with a Novel Hybrid MoM-FDTD Method", *Microwave Conference Proceedings, Asia-Pacific Conference Proceedings*, Dec. 2005,

[30] W. Thiel, K. F. Sabet and L.P.B. Katehi, "A hybrid MoM/FDTD approach for an efficient modeling of complex antennas on mobile platforms", *European Microwave Conference*, 33rd Volume, 2003

[31] H. Shabani, R. Islam, AHM Zahirul Alam, H. Essam and Abd El-Raouf, "Development of Analytical Flat Phantom Model for EM Radiation to Evaluate Specific Absorption Rate (SAR) in Human Body", *Proceedings of the International Conference on Computer and Communication Engineering*, pp. 1186-1193, May 2008

[32] S. Watanabe, M. Taki, T. Nojima and O. Fujiwara, "Characteristics of the SAR Distributions in a Head Exposed to Electromagnetic Fields Radiated by a Hand-Held Portable Radio", *IEEE Trans. Microwave Theory Tech.*, vol. 44, no. 10, pp. 1874-1883, 1996

[33] Q. Balzano, M. Y. Kanda, and C. C. Davis, "Specific Absorption Rates in a Flat Phantom in the Near-Field of Dipole Antennas", *IEEE Trans. on Electromagnetic Compatibility*, vol. 48, No. 3, pp 563-568, 2006

[34] J. C. Lin, "Cataracts and Cell-Phone Radiation", *IEEE Antennas and Propagation Magazine*, Vol. 45, Issue 1, pp. 171 – 174, 2003

[35] J. C. Lin, "Biological Bases of Current Guidelines for Human Exposure to Radio-Frequency Radiation", *IEEE Antennas and Propagation Magazine*, Vol. 45, Issue 3, pp. 182-184, 2003

[36] A. Hirata, S. Matsuyama and T. Shiozawa, "Temperature Rises in the Human Eye Exposed to EM Waves in the Frequency Range 0.6–6 GHz", *IEEE Trans. on Electromagnetic Compatibility*, vol. 42, No. 4, pp 386-393, 2000

[37] A. Hirata, M. Morita, and T. Shiozawa, "Temperature Increase in the Human Head Due to a Dipole Antenna at Microwave Frequencies", *IEEE Trans. on Electromagnetic Compatibility*, vol. 45, No. 1, pp 109-116, 2003

APPENDIX

APPENDIX I: RECOMMENDED LIMITS FOR THE MAXIMUM RADIATION EXPOSURE ADOPTED BY DIFFERENT ORGANIZATIONS

Organizations	Exposure Criteria	Frequency Range (MHz)	E-field Strength (Vm ⁻¹)	H-field Strength (Am ⁻¹)	Power Density (Wm ⁻²)	Averaging Time E ² , H ² or S (min)
IEEE	Occupational	300-3000	—	—	f/300	6
	General Public		—	—	f/1500	30
ICNIRP	Occupational	400-2000	3f ^{1/2}	0.008f ^{1/2}	f/40	—
	General Public		1.375f ^{1/2}	0.0037f ^{1/2}	f/200	—
FCC	Occupational	300-1500	—	—	f/300	6
	General Public		—	—	f/1500	30

APPENDIX II: RECOMMENDED SAR LIMITS ADOPTED BY DIFFERENT COUNTRIES

	Exposure Criteria	SAR Limits (W/kg)			Averaging Time (min)
		Whole Body	Spatial Peak	Size	
Australia	Occupational	0.4	10	10g.	6
	General Public	0.08	2	10g.	6
USA	Occupational	0.4	8	1g.	6
	General Public	0.08	1.6	1g.	30
Europe	Occupational	0.4	10	10g.	6
	General Public	0.08	2	10g.	6
Japan	Occupational	0.4	8	10g.	6
	General Public	0.04	2	10g.	6

Design of A Lowpass Filter using Defected Microstrip Structure (DMS)

Tamasi Moyra

Dept. of Electronics and Communication Engineering,
College of Engineering and Management, Kolaghat
Midnapur dist., West Bengal, India
email: tamasi_moyra@yahoo.co.in

Lakhindar Murmu, Santanu Das, Susanta Kumar Parui

Dept. of Electronics and Telecommunication Engineering,
Bengal Engineering and Science University, Shibpur,
Howrah – 711 103, Westbengal, India
email: arkapv@yahoo.com & santanumdas@yahoo.com

Abstract—A new brand of slowwave structure called defected microstrip structure (DMS) has been introduced. The frequency characteristics of proposed L-shaped DMS unit show a deep stop-band. An equivalent L-C network is proposed to model it. It is also observed that two such cascaded units provide good elliptic filtering response.

Keywords- microstrip, defected microstrip structure, defected ground structure, lowpass filter

I. INTRODUCTION

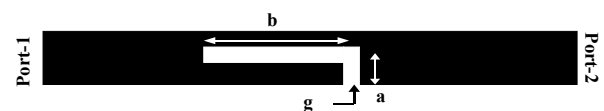
The microstrip line acts as a good transmission line. But the performance of the microstrip line can be improved with the help of slots in microstrip line and this structure also known as Defected Microstrip Structure (DMS). In lots of papers it is observed that a defected etched in the metallic ground plane of a microstrip line is an attractive solution for achieving finite pass band, rejection band and slow-wave characteristics due to disturbance or perturbation of the shield current distribution in the ground plane.

Dumb-bell shaped DGS is explored first time by D. Ahn and applied to design a lowpass filter [1,2]. Unit cell has been described as a one-pole Butterworth filter, where the capacitance comes only from the gap and the inductance comes only from the loop. It is well known that a filter with attenuation poles and attenuation zeros at finite frequencies shows higher selectivity compared to all pole filter. DGSs with quasi-elliptical response were proposed and used for designing lowpass filter recently [3-5].

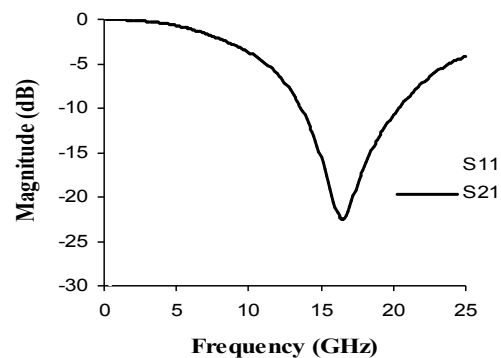
In this paper a new approach has been taken. A defected slot introduces over the microstrip line is an attractive solution for achieving finite pass band, rejection band and slow-wave characteristics. The slow wave factor over the microstrip is increased since the current distribution in the microstrip line is perturbed due to the trajectory followed around the slot line, which introduces high line inductance and capacitance of the microstrip line [6]. Thus, it obtains a stop band and compact size, which meet emerging application challenges.

II. FREQUENCY CHARACTERISTICS OF DMS

Fig. 1(a) shows the schematic diagram of a investigated DMS unit consists of L-shaped slot etched off over the microstrip line. The substrate with a dielectric constant of 4.4, loss tangent of 0.0025 and thickness of 1.57 mm is considered for the microstrip line. The width (w) of the microstrip line is obtained as 3 mm corresponding to 50 Ohm characteristics impedance. The different dimensions of L-shaped DMS unit have been taken as $a = 1.6$ mm, $b = 2$ mm and $g = 0.2$ mm as shown in Fig. 1(a). In order to investigate the frequency characteristics of the DGS unit, it is simulated by the MoM based IE3D simulator.



(a)



(b)

Figure 1. (a) Schematic diagram of L-shaped DMS (b) Its scattering parameters

III. EQUIVALENT CIRCUIT

It is observed that DMS cell behaves like an L-C resonant circuit. It may be described by a series inductor performing the associated inductance and the inductor is connected in parallel to a short circuited transmission line with impedance Z_S and electric length θ , which represents the periodic behavior of the line. DMS Equivalent circuit is shown in Fig 2(a).

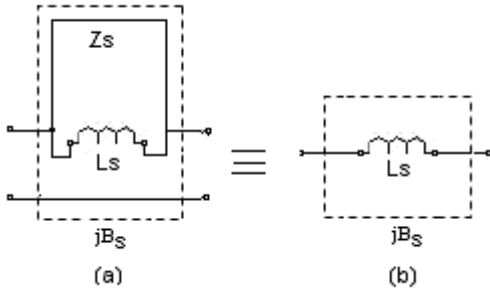


Figure 2. (a) Equivalent circuit model for defected (slotted) microstrip structure and (b) Butterworth-type low-pass Filter

As in the case of Defected Ground, the Defected Microstrip model is compared to the performance of a one-pole Butterworth-type, since similar properties can be seen in both circuits. The corresponding equations are obtained for DMS model as per Fig. 2. The equations are represented as

$$X_S = j \frac{Z_S \omega L_S \tan \theta}{\omega L_S + Z_S \tan \theta} \dots\dots\dots(1)$$

$$X_B = j \omega L_B \dots\dots\dots(2)$$

Where, X_S , Z_S , θ , L_S are the reactance of the equivalent circuit, the transmission line impedance, the electric length of the line and the associated inductance of the model, respectively. X_B is the reactance of the one-pole Butterworth-type low-pass filter.

To find the values of the elements in the equivalent model, (1) and (2) are solved simultaneously, considering the conditions of resonance of both circuits, where the susceptance and reactance should be equal to zero. At the cutoff frequency, (1) is equal to (2). At the frequency where the pole is located, the condition that satisfies the equations is $\theta = 0^\circ$ or 180° . Then, such conditions give the following pair of equations:

$$L_S = \frac{L_B (f_O \cot \theta_O - f_C \cot \theta_C)}{f_0 \cot \theta_0} \dots\dots\dots(3)$$

$$Y_S = -\frac{1}{2\pi f_0 L_S \cot \theta_0} \dots\dots\dots(4)$$

Where, θ_0 and θ_C are the electric length of the line at the resonant frequency, f_0 , and the -3dB cutoff frequency, f_c , respectively. The required frequencies for the solution of equations are obtained extracting the parameters from EM simulation.

IV. FREQUENCY CHARACTERISTICS OF DIFFERENT DMSS

The resonant frequency of the DMS unit may be varied by bending the total length of the DMS slot like L, U and Spiral shape keeping same overall cutout area as illustrated in Fig. 3.

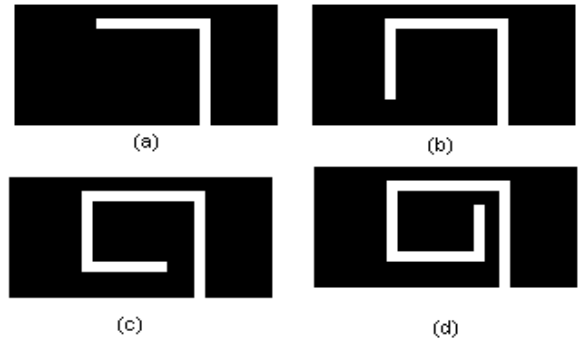


Figure 3. (a) L-DMS (b) U-DMS (c) Spiral (SP1)-DMS (d) Spiral1 (SP2)-DMS

The frequency characteristics of the different DMS structures are shown in the Fig. 4. It is observed from the response that the resonance frequency will be decreased due to the increment of the inductance value with increment of the length of DMS unit.

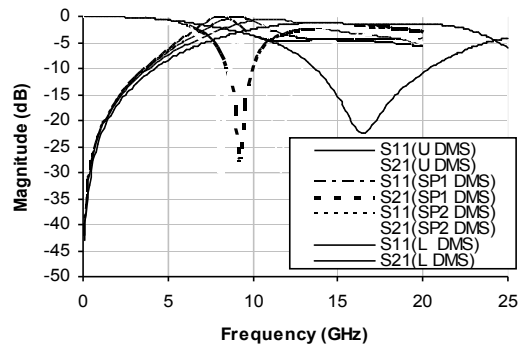


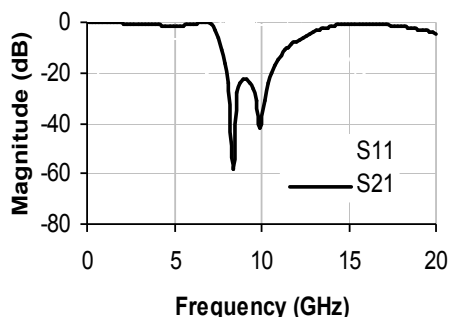
Figure 4. S-Parameters for different shaped DMS

V. REALIZATION OF LOWPASS FILTER

It is possible to implementation of LPF filter by cascading two spiral (SP1) type DMS units with separation (S) between them by 1mm and total length of DMS is 5.4 mm as shown in the following Fig 5(a).



(a)



(b)

Figure 5. (a) Schematic diagram of lowpass filter comprising two DMS cell (b) S-Parameters for different s

The simulated S-parameters in the Fig. 5(b) looks like an elliptical lowpass filter having attenuation pole at 8.34 GHz, attenuation zero at 7.3 GHz, sharpness factor of 53.5 dB/GHz and 20 dB bandwidth of 2.5 GHz. The stopband may be tuned with the separation (s) between DGS cells as shown in Fig 6.

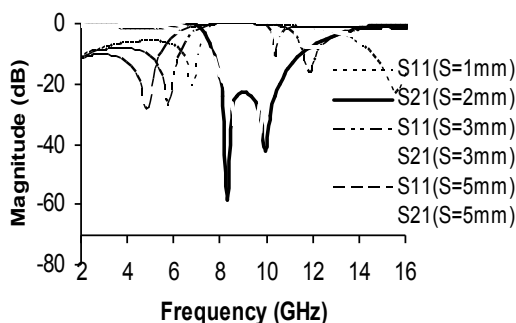


Figure 6. S-Parameters for lowpass filter for different value of s

As the separation between two cell decreases, the sharpness factor at transition knee increase and also the bandwidth increases. But the insertion loss in the passband reduces with the separation between two cells. The results are tabulated in Table-1 as follows.

Table-1. Filter parametric variation with ‘S’

S (mm)	attn Pole (GHz)	Attu Zero (GHz)	Insertion loss (dB)	sharpness factor(dB /GHz)	20dB bandwidth (GHz)
1	8.34	7.3	1.02	53.5	2.50
2	8.76	7.17	0.89	30.77	2.24
3	8.89	6.84	0.55	22.15	2.02
5	9.18	6.23	0.38	15.68	1.73

VI. CONCLUSION

The proposed DMS structures exhibit the one pole filtering characteristics. This structure is very simple and it is implemented with minimum use of real estate. It may be implemented within feed line of any conventional planar circuit and component. Two such DMS units are cascaded to achieve a lowpass filter with better sharpness factor, low passband insertion loss, and good fractional bandwidth. Thus, it may find use to improve the different circuit and systems required in modern wireless communication system.

VII. ACKNOWLEDGEMENT

The work is done under the project funded by CSIR, New Delhi, Govt. of India.

VIII. REFERENCES

- [1] C.S.Kim, J.S.Park, D.Ahn and J.B. Lim, "A novel one dimensional periodic defected ground structure for planar circuits," *IEEE Microwave and Guided wave Letters*, vol. 10, No. 4, pp.131-133, 2000
- [2] D. Ahn, J.S.Park, C.S.Kim, J.Kim, Y Qian and T. Itoh, "A design of the lowpass filter using the novel microstrip defected ground structure," *IEEE Trans. on Microwave Theory and Techniques*, vol. 49, no. 1, pp. 86-93, 2001
- [3] Chen J.-X., Li J.-L., Wan K.-C. and Xue Q., "Compact quasi-elliptic function filter based on defected ground structure," *IEE Proc.-Microwave Antennas propagation*, vol. 153, no. 4, pp. 320-324, Aug. 2006
- [4] Susanta Kumar Parui, Santanu Das 'An asymmetric defected ground structure with elliptical response and its application as a lowpass filter' *Int. J. Electron. Commun. (AEÜ)* vol. 63 ,pp.483 – 490, 2009
- [5] Parui, Susanta Kumar, Moyra, Tamasi and Das, Santanu "Quasi-elliptic filter characteristics of an asymmetric defective ground structure," *International Journal of Electronics*, Vol.-96, No.-9, PP-915-924. September 2009
- [6] A. Tirado-Mendez, H. Jardon-Aguilar, and R. Flores-Leal "Improving frequency response of microstrip filters using defected ground and defected microstrip structures" *Progress In Electromagnetics Research C*, Vol. 13, 77 - 90, 2010

Design and analysis of a rectangular microstrip patch antenna with EBG structure at the ground plane for WLAN application.

¹Chandan Kumar Ghosh, ²Sanchita Datta, ³Ankita Mitra, ⁴Susanta Kumar Parui
^{1,2,3}Dr. B.C. Roy Engineering College, Jemua Road, Fuljhore, Durgapur-6, India
¹mcet_ckg@yahoo.com, ²sanchita5138@yahoo.co.in, ³mistu_mitra@yahoo.com
⁴Bengal Engineering and Science University, Shibpur, India

Abstract-In this article a circularly polarized rectangular patch antenna with and without electromagnetic bandgap (EBG) structure using coaxial probe feed is presented. The proposed antenna is low profile, conformable to planar and nonplanar surfaces, simple and inexpensive to manufacture using modern printed-circuit technology. It is mechanically robust when mounted on rigid surfaces and compatible to WLAN band. The characteristics of the patch antenna have been studied both numerically and experimentally. The proposed antenna offers minimum return loss (RL), good radiation characteristics and better efficiency. The experimental results have a good agreement with the simulated one.

INTRODUCTION

THE microstrip patch antennas are very popular for their low profile, low cost, planer and non-planer structure and easy to handle. In this investigation we have designed, simulated and analyzed a simple patch antenna with and without EBG structure at the ground plane.

EBG structures are novel periodic composites exhibiting desirable electromagnetic properties [1, 2] that may not occur with a simple planer structure. They have been implemented in a wide range of applications in antennas, electromagnetic compatibility, microwave circuits etc. This structures have attracted considerable interest in recent years due to their advantages of high directivity, low side lobes [3, 4], simple structure and relatively low-profile. Typically these antennas consist of an EBG structure, such as a frequency selective surface (FSS) placed approximately half a wavelength above a ground plane containing a source antenna [5]. The exact distance between the EBG structure and the ground plane is determined by the reflection phase of both materials at the operating frequency. One limitation of these types of antennas is their low radiation bandwidth due to the high Q factor of the resonating structure. One method of improving the useable frequency range of the antenna, which we investigated in this article, is to make the operating frequency reconfigurable.

The proposed antenna is designed to function in the 5.25 GHz which corresponds to IEEE 802.11a (VSWR<2, data rate 54Mbps/B.W 20 dB and S-parameters, $S_{ij} < -20\text{dB}$ where $i \neq j$) wireless LAN application. The proposed antenna array is a high gain, low-cost, low weight base station antenna for WLAN band. The characteristic analyses such as return loss (RL),

bandwidth, VSWR and radiation pattern of the prototype antenna array have been investigated both numerically and experimentally. In this investigation, VSWR less than 1.35 and bandwidth of 120MHz (For RL>-9.5dB) and antenna gain of 7.88 dBi have been achieved.

The microstrip patch normally radiates normal to the patch. So elevation pattern gain for $\phi=0$ deg. and $\phi=90$ deg. is important. The substance of thickness (h) 1.588, is a RT/duroid material with electrical properties $\epsilon_r=2.2$, $\tan\delta=0.001$ have been considered. The band width of a patch antenna is inversely proportional to the square root of the dielectric constant of the substrate [6]. The length and width of the patch has been design by the following formulae [7]. The characteristics of the antenna have been simulated with the help of Zeland make IE3D electromagnetic simulator, based on method of moment (MOM). The characteristics of the patch antenna have been studied numerically with

$$W = \frac{c}{2f} \sqrt{\frac{2}{\epsilon_r + 1}} \quad (1)$$

$$L_{\text{eff}} = \frac{c}{2f_0 \sqrt{\epsilon_{\text{reff}}}} \quad (1a)$$

$$\epsilon_{\text{reff}} = \frac{\epsilon_r + 1}{2} + \frac{\epsilon_r - 1}{2} \left(\frac{1}{\sqrt{1 + 12h/W}} \right) \quad (2)$$

$$\Delta L = 0.412h \frac{(\epsilon_{\text{reff}} + 0.3) \left(\frac{W}{h} + 0.264 \right)}{(\epsilon_{\text{reff}} - 0.258) \left(\frac{W}{h} + 0.8 \right)} \quad (3)$$

The actual length of the patch $L = \frac{\lambda}{2} - 2\Delta L$ and the final effective length $L_e = L + 2\Delta L = \frac{\lambda}{2}$, using above numerical equations the dimension of the patch are given in the **Table-1**, using operating frequency of 5.25GHz

Table-1

Parameter of the patch	W (mm)	ϵ_{reff}	ΔL (mm)	L_{eff} (mm)	L (mm)
Calculated value	23.95	2.047	0.83	21.17	19.52
Design Value	23.00	2.044	0.83	21.19	19.53

The geometry of the patch is illustrated in the Figure-1 and the corresponding equivalent circuit is given in the Figure-2. There are a number of substrates that can be used for the design of microstrip antennas, and their dielectric constants are usually in the range of $2.2 \leq \epsilon \leq 12$. The substances which have dielectric constants in the lower side provide better efficiency, larger band width, loosely bound fields for radiation into space, but the element size should be large.

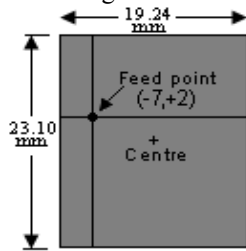


Fig. 1 Actual dimension and position of the feed point.

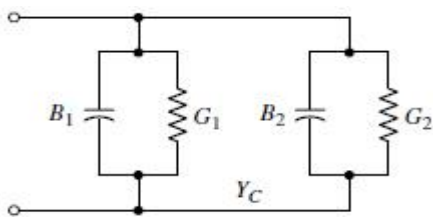


Fig.2 Equivalent circuit of the patch

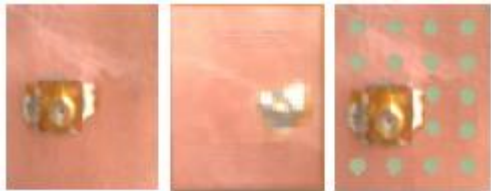


Fig.3 Fabricated prototype antenna with and without EBG structure at the ground plane.

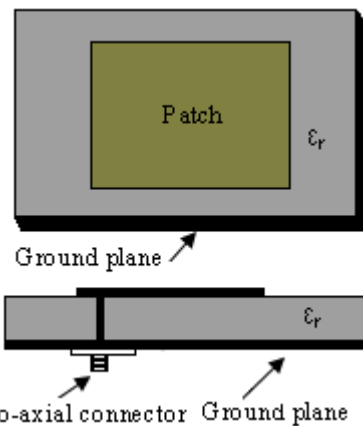


Fig. 3 Schematic diagram of Probe feed to the patch

RESULTS

The software used to model and simulate the microstrip patch array is Zeland Inc's IE3D electromagnetic simulator. It has been widely used in the design of patch

antenna, wire antenna, and other RF/wireless antennas. It can be used to calculate and plot the S- parameters, VSWR, antenna efficiency, current distribution as well as the radiation pattern of any geometrical shaped microstrip patch antenna.

The simulated results of return Loss (RL) and the elevation pattern of radiation characteristics are illustrated in Figure-4 and Figure-5 & Figure-6. The antenna efficiency is illustrated in the figure-7

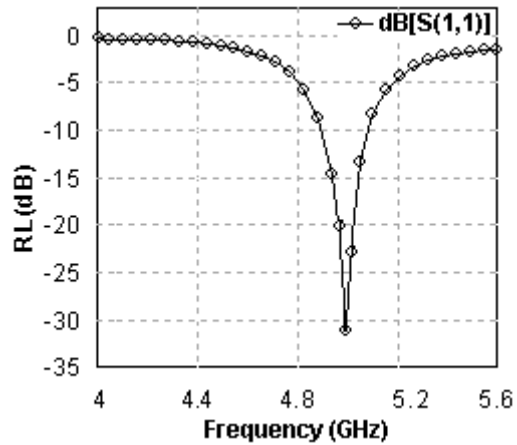


Fig.5 Return loss Characteristics of proposed antenna.

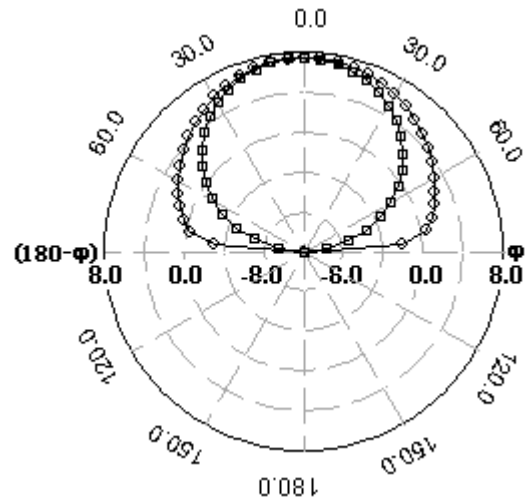


Fig.6 E- plane and H- plane pattern at 4.95 GHz

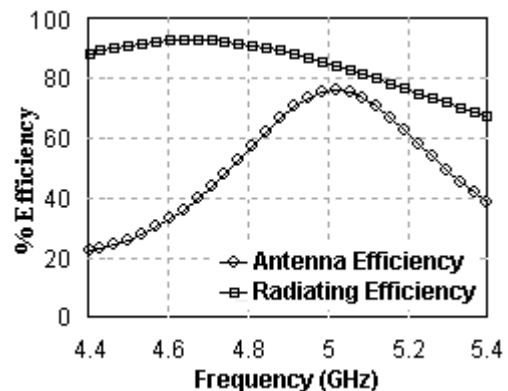


Fig. 7 Efficiency Vs frequency plot of proposed antenna.

The main disadvantages of patch antenna are their poor efficiency, low power handling capability, high Q and narrow bandwidth. However, the efficiency and band width can be improved by increasing the height of the dielectric substrate.

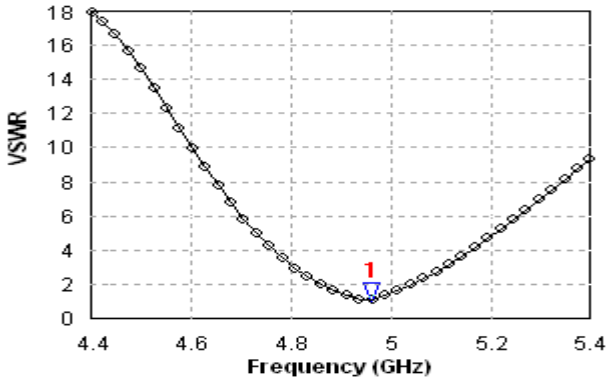
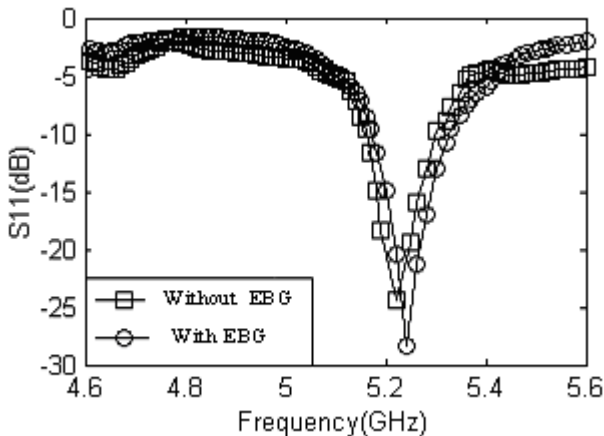
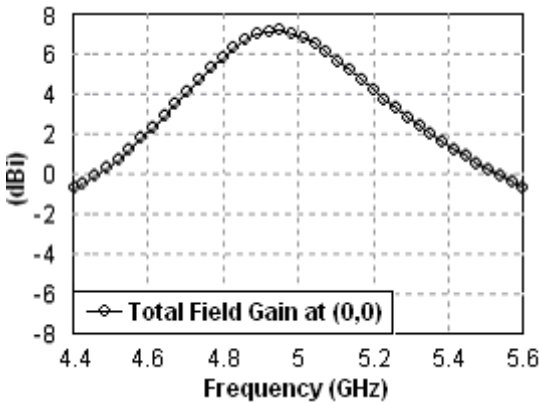


Fig.6 Graphical plot of VSWR Vs frequency

The radiation pattern was measured using a reference antenna designed to operate at 5.0GHz, as a transmitting antenna and the patch antenna as receiver. In this attempt, the patch was rotated 360 and measured the amplitude of received E-field for each degree. The result is illustrated in the Figure-X. The measurement was carried out at Bengal Engineering and Science University. The Impedance was measured using network analyzer.



REFERENCES

- [1] Sievenpiper, D., L. Zhang, R. F. J. Broas, N. G. Alexopoulos, and E. Yablonovitch, "High-impedance electromagnetic surfaces with a forbidden frequency band," *IEEE Trans. Microwave TheoryTech.*, Vol. 47, 2059–2074, Nov. 1999.
- [2] M. Thèvenot, C. Cheype, A. Reineix, and B. Jecko, "Directive photonic bandgap antennas," *IEEE Trans. Microw. Theory Tech.*, vol. 47, no. 11, pp. 2115–2122, 1999.
- [3] A. R. Weily, L. Horvath, K. P. Esselle, B. C. Sanders, and T. S. Bird, "A planar resonator antenna based on a woodpile EBG material," *IEEE Trans. Antennas Propagation*, vol. 53, no. 1, pp. 216–223, Jan. 2005.
- [4] A. R. Weily, T. S. Bird and Y. J. Guo, "A Reconfigurable High Gain EBG Antenna," *EMTS 2007 International URSI Commission B - Electromagnetic Theory Symposium • July 26-28, 2007 • Ottawa, ON, Canada*
- [5] Sievenpiper, D., L. Zhang, R. F. J. Broas, N. G. Alexopoulos, and E. Yablonovitch, "High-impedance electromagnetic surfaces with a forbidden frequency band," *IEEE Trans. Microwave TheoryTech.*, Vol. 47, 2059–2074, Nov. 1999.
- [6] C.C. Chiau, X.Chen and C.G. Parini, "A Novel Dielectric Loaded Folded Half-Loop Antenna for Mobile Terminals", *IEEE AP-S International Symposium on Antenna and Propagation*, Washington DC, USA, vol. 1A, pp.499-502, 3-8 July,2005.
- [7] R. A. Sainati CAD of micro strip antenna for wireless applications. Artech House, Inc.1996.

Design and Development of a Wearable Antenna for HiperLAN/2 Applications

S.Sankaralingam¹ and Sayantan Dhar²

Department of Electronics and Tele-Communication Engineering
Jadavpur University, Kolkata – 700 032 INDIA
slingam.nec@gmail.com¹, sayan.dhar@gmail.com²

Abstract- The evolution of antenna technology for man-machine interface has taken quantum leaps in utilizing textile materials as antenna substrates. In future this will allow complete freedom to develop body-worn antenna systems embedded in every day wear. Fuelled by this idea of a body-centric approach to future communication technology, many research projects have been initiated, to integrate antennas and RF systems into the clothes with regard to size reduction and cost effectiveness. For instance, the development of wearable computer systems is very rapid and soon one will see a wide range of unobtrusive wearable and ubiquitous computing equipment into his/her everyday wear. Rapid progress in wireless communication promises to replace wired-communication networks in the near future in which antennas play a vital role. In this paper, a wearable antenna for HiperLAN/2 applications has been designed, developed and evaluated. This antenna yields promising results and demonstrate the use of textile materials as substrates for the design and development of wearable microstrip antennas.

I. INTRODUCTION

Wearable computing and wearable electronics are seen as the next step in integration of electronic devices into everyday human life. In recent years, both 2.45 GHz (WLAN) and 5.8 GHz (HiperLAN/2) bands are used for wireless network applications. HiperLAN/2, which stands for High Performance Radio Local Area Network, is a Wireless LAN standard developed by the Broadband Radio Access Networks (BRAN) division of the European Telecommunications Standards Institute (ETSI). HiperLAN/2 technology operates in the 5 GHz frequency band using Orthogonal Frequency Division Multiplexing (OFDM) and offers many features [1] including high speed transmission (data rate up to 54 Mbps), power saving, mobility support, security support and increased range of coverage (up to 50 m). HiperLAN/2 band ranges from 5725 MHz – 5875 MHz with 5.8 GHz as its centre frequency. This HiperLAN/2 band is aimed for communication

between all kinds of wireless devices. These mobile wireless systems contain several subsystems and antenna is an essential one among them. Therefore wearable antenna plays a paramount role in optimal design of any wearable system. For convenience of the user, the wearable antenna needs to be hidden and of low profile. This requires a possible integration of the antenna elements within everyday clothing. Microstrip patch is a suitable candidate for any wearable application, as it can be made conformal for integration into clothing [2].

In line to their previous research work on copper based wearable antennas with rectangular and circular geometries [3-6], the authors present the design, development and assessment of a copper based triangular shaped microstrip wearable antenna for HiperLAN/2 applications in this paper. The antenna under investigation makes use of copper for all its conducting parts and polyester insulating fabric for the dielectric substrate material. Theoretical and experimental results on performance characteristics of this wearable antenna like resonant frequency, return loss, impedance bandwidth, gain and radiation pattern are presented.

The rest of the paper has been organized as follows: Section II explains the steps involved in the antenna design procedure. Section III describes the electromagnetic modeling and fabrication of antenna. Both theoretical and experimental results on the performance characteristics of the wearable antenna under investigation are presented in Section IV. Concluding remarks of this research work are offered at the end of this paper in Section V.

II. ANTENNA DESIGN PROCEDURE

Triangular microstrip wearable antennas are found to provide radiation characteristics similar to those of rectangular or circular wearable antennas, but with a smaller size. The geometry of an equilateral triangle microstrip antenna and the coordinate system used are shown in figure 1.

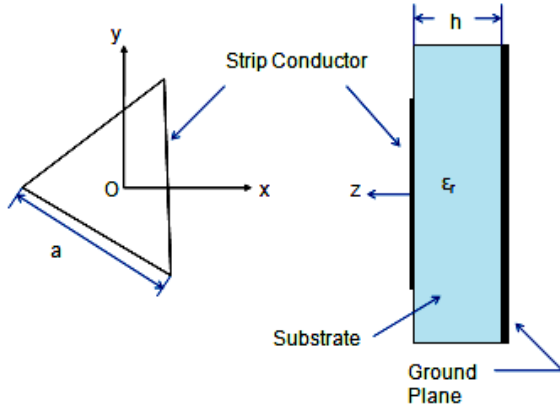


Fig. 1 Geometry of triangular microstrip patch antenna

The simplest of the triangular microstrip wearable antenna comprises an equilateral triangular conductor on a grounded dielectric substrate. The design specifications of the antenna are listed hereunder:

- Resonant frequency (f_r) = 5.8 GHz
- Thickness of the substrate (h) = 2.85 mm
- Relative permittivity (ϵ_r) = 1.44
- Loss tangent ($\tan \delta$) = 0.01

The design equations are given below:

The resonant frequency for TM_{10} mode by considering an effective value of the side length (a_e) of equilateral triangle is given by [7],

$$f_{10} = \frac{2c}{3a_e\sqrt{\epsilon_r}} \quad (1)$$

where

$$a_e = a \left[1 + 2.199 \frac{h}{a} - 12.853 \frac{h}{a\sqrt{\epsilon_r}} + 16.436 \frac{h}{a\sqrt{\epsilon_r}} + 6.182 \left(\frac{h}{a}\right)^2 - 9.802 \left(\frac{1}{\sqrt{\epsilon_r}}\right) \left(\frac{h}{a}\right)^2 \right] \quad (2)$$

The height of the equilateral triangle is

$$(a\sqrt{3}) / 2 \quad (3)$$

Its vertices are at

$$\left(-\frac{a}{\sqrt{3}}, 0\right), \left(\frac{a}{2\sqrt{3}}, \frac{a}{2}\right), \text{ and } \left(\frac{a}{2\sqrt{3}}, -\frac{a}{2}\right) \quad (4)$$

The design procedure involves the following steps:

- (1) Calculate the effective value of side length (a_e) using eqn. (1)
- (2) Calculate the value of a using eqn. (2)
- (3) Compute the coordinates of the vertices of the triangle using eqn. (4).
- (4) Simulate the geometry of the triangular patch using IE3D software and optimize for a
- (5) Optimize the probe feed position to get good impedance matching (50 ohms)

The effective value of side length of triangular patch is computed to be 28.74 mm

III. MODELING AND FABRICATION OF ANTENNA

The modeling of the HiperLAN antenna is performed using the Method of Moments (MoM) based IE3D simulator [8] from Zeland Software Inc., USA. An infinite ground plane is assumed so as to (i) avoid back lobes in the radiation pattern of the antenna (ii) reduce the diffraction and scattering effects at the edges of the ground plane and to (iii) minimize the undesirable effects of surface waves. The conductive parts of the antenna are made up of copper whereas the substrate material is the polyester fabric of required thickness. The value of side length a for this patch antenna is optimized as 25.5 mm by doing rigorous simulations. This wearable patch antenna is excited by means of a coaxial feed. While modeling the coaxial probe feed to patch, the inner and outer diameters of the probe are taken as 1.3 mm and 4.1 mm respectively corresponding to a standard 50 ohm SMA connector. The feed position is optimized to get good matching characteristics (50 ohm impedance) at the centre frequency. It is located at a distance of 3.7 mm from the centroid of the triangular patch towards its apex. Figure 2 shows a photograph of the fabricated antenna whose ground plane size is taken as 120 mm X 120 mm. The thicknesses of top signal layer and bottom ground plane are 0.1 mm and 0.5 mm respectively. The patch and ground plane of the antenna are cut out from copper sheets using CNC machine so that an accuracy of about 20 μ m is achieved. The size of the insulating fabric material is taken to be equal to that of ground plane. The insulating fabric pieces are stacked and stitched properly to get required thickness. While assembling the antenna elements, the copper sheets are just fixed on the dielectric fabric material with scotch tape and due care is taken such that there is no air gap between the insulating fabric material and the conducting parts of the antenna

IV. RESULTS ON PERFORMANCE CHARACTERISTICS OF WEARABLE ANTENNA

A. Return Loss Characteristics

A.1 Simulated and Measured Results

Simulations and measurements as well are carried out over the frequency range of 5.2 GHz to 6.2 GHz for the antenna developed. Fig. 3 shows the simulated and measured S_{11} plots of the HiperLAN/2 antenna under investigation.



Fig. 2 Photograph of the fabricated wearable antenna

As depicted by the simulation results, this wearable antenna resonates at a frequency of 5.8 GHz and exhibits a -10dB return loss bandwidth of 432.76 MHz. The measurements are done using a vector network analyzer (Model # 5071 B) from Agilent Technologies. Initially, the network analyzer is calibrated using the 2 port Ecal [9] module, bearing model # 85092C for an operating frequency ranging from 300 kHz to 9 GHz, which provides excellent accuracy. The fabricated structure is measured for a resonant frequency of 5.775 GHz with an impedance bandwidth of 308.7 MHz and having a return loss of -17.76 dB at the resonant frequency as shown in fig 3. There is an excellent match between simulated and measured resonant frequencies in this case as the deviation between these values is only 0.0043%. As far as the impedance bandwidth is concerned, it is observed that the measured value of impedance bandwidth covers the entire HiperLAN/2 band and therefore this antenna can be designed and employed for High Performance Local Area Network applications.

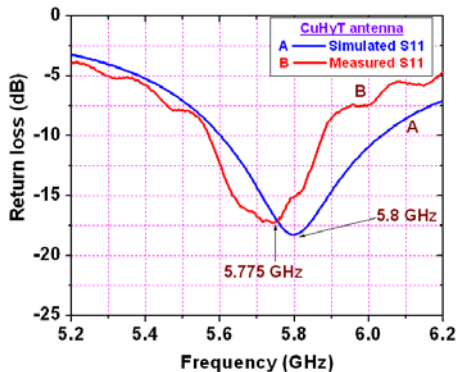
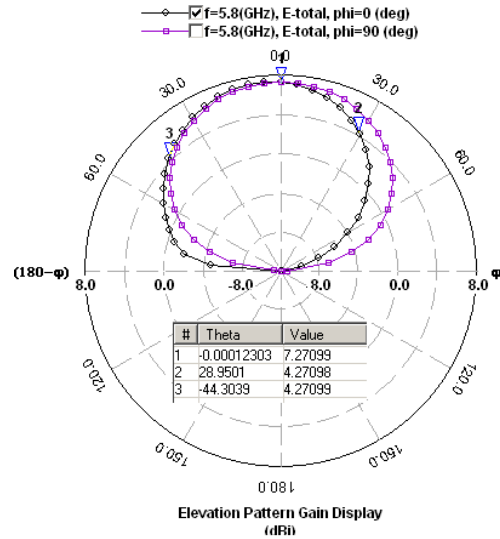


Fig. 3 Return loss plot of triangular microstrip wearable antenna

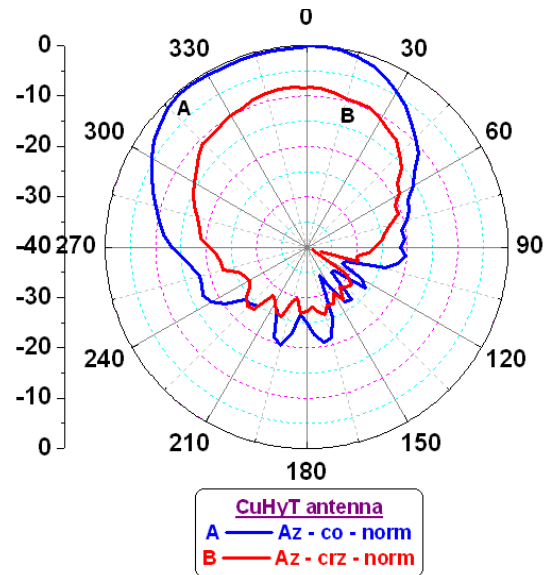
B. Far-field Radiation Characteristics

B.1 Radiation Patterns (Simulated and Measured Results)

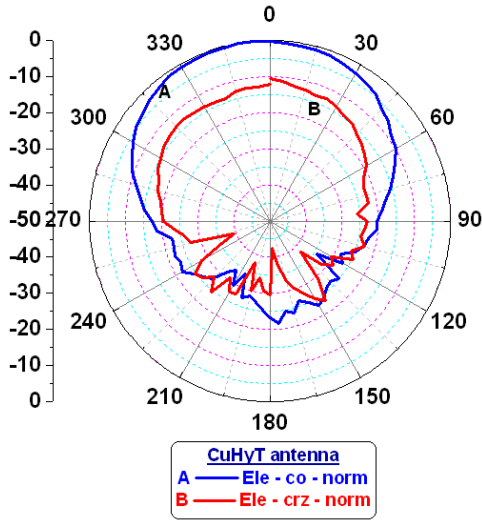
Simulated total far-field radiation patterns of electromagnetically modeled antennas, in both principal planes of $\phi = 0^{\circ}$ (x-z) and $\phi = 90^{\circ}$ (y-z), are obtained at its simulated resonant frequency of 5.8 GHz. Fabricated triangular microstrip antenna is subjected to far-field radiation pattern measurements at its measured resonant frequency (5.775 GHz) in a rectangular shielded anechoic chamber. Simulated and measured far-field patterns of this triangular shaped wearable antenna are shown in figures 4 (a) – (c).



(a) Simulated



(b) Measured (Azimuth)



(c) Measured (Elevation)

Fig. 4 (a)-(c) Radiation patterns of triangular shaped wearable HiperLAN antenna

C. Discussions

Referring to radiation patterns of the fabricated antenna, it is understood that the values of discrimination between co-polar and cross polar components in azimuth and elevation planes are 8.5 dB and 12.19 dB respectively. These values are reasonably good for practical applications. Simulated values of 3dB beam-width in the x-z and y-z planes of this antenna are 73.25° and 83.09° respectively. Measured 3 dB beam-width values in azimuth and elevation planes, as obtained from the corresponding radiation pattern plots, are 77° and 73° respectively.

D. Gain, Directivity and Efficiency

Simulations are done for a range of frequencies from 5.5 GHz to 6.0 GHz in order to find antenna parameters like gain, directivity and radiating efficiency. Gain of the antenna in the same frequency range is measured using gain-comparison method [10]. Variations of simulated gain, measured gain and simulated directivity as functions of frequency for the investigated antenna are plotted in figures 5. The simulated radiating efficiency plot of the antenna under study is shown in fig. 6. The measured value of directivity of antenna is computed from measured radiation patterns using the standard formulae [10]. The performance characteristics of this wearable antenna are tabulated in Table 1. The characteristics exhibited by the developed antenna are very useful for practical considerations.

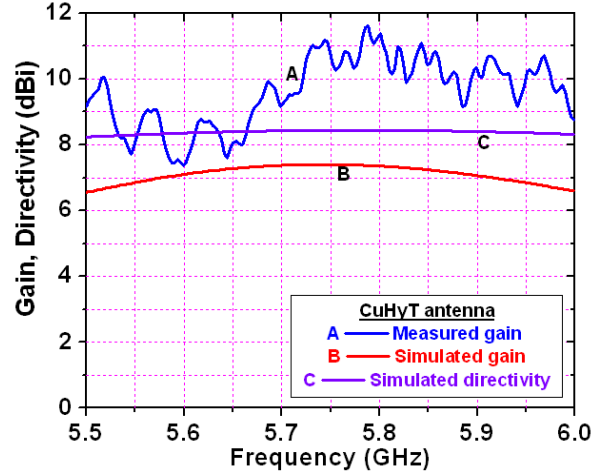


Fig.5 Gain and Directivity as functions of frequency

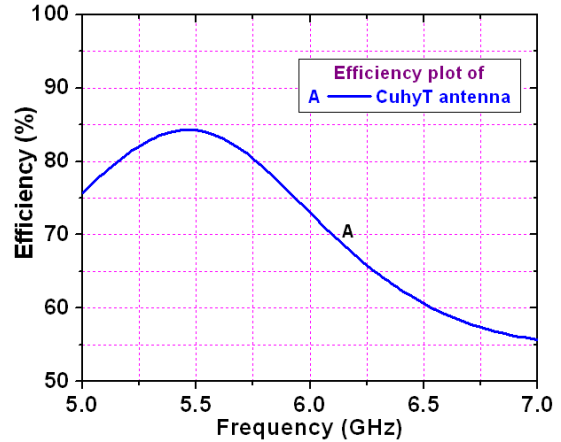


Fig. 6 Efficiency plot of wearable antenna

TABLE 1
PERFORMANCE CHARACTERISTICS OF TRIANGULAR SHAPED WEARABLE ANTENNA

Parameter	Simulated	Measured
Gain (dBi)	7.35	11.01
Directivity (dBi)	8.44	7.12
Efficiency (%)	79.07	72.0

V. CONCLUSIONS

In this paper a triangular shaped patch antenna has been designed, developed and tested in order to get its impedance and radiation characteristics. The following conclusions may be drawn from this experimental work. Firstly, microstrip antenna is a suitable candidate for wearable applications, as it can be built using fabric substrate materials. The antennas of this type are very versatile and it is easy to make them operate at various frequency bands. In addition, the well known techniques [7] of improving bandwidth and obtaining different polarizations, adopted for microstrip patch antennas are readily suitable for wearable antennas too. It may be

concluded that these textile patch antennas may eventually replace patch antennas on standard PCB substrates for various applications. These wearable antennas must be drapable as the fabrics can take diverse shapes because of human body movements. Therefore, further investigations are required to study the effects of antenna bending on performance characteristics of wearable antennas.

ACKNOWLEDGEMENT

The authors would like to thank Dr. Anil Kumar Singh and Sri. Mohan Kumar of Electronics and Radar Development Establishment (LRDE) - Defence Research and Development Organization (DRDO), Bangalore for their help in measurement of radiation characteristics of the antenna developed

REFERENCES

- [1] <http://www.tml.tkk.fi/Studies/Tik110.300/1999/Essays/hiperlan2.html#ch1>
- [2] Pekka Salomen and Heli Hurme, "A Novel Fabric WLAN Antenna for Wearable Applications," Proceedings of IEEE APS International Symposium, Vol. 2, pp 700-703, June 2003
- [3] S.Sankaralingam and Bhaskar Gupta, "Performance Study of a Bluetooth antenna for wearable applications" Proc. of Int. Symposium on Antennas and Propagation (ISAP), Bangkok, Oct. 2009
- [4] S. Sankaralingam and Bhaskar Gupta, "Use of Fabric Materials as Substrates for Antennas for ISM applications" Proc. of Int. conf. on Communication Technologies and VLSI Design, Vellore, Oct. 2009
- [5] S. Sankaralingam and Bhaskar Gupta, "A circular disk microstrip WLAN antenna for wearable applications" In press: Proc. of INDICON 2009, Ahmedabad, Dec. 2009
- [6] S. Sankaralingam and Bhaskar Gupta, "A textile antenna for WLAN applications" In press: Proc. of ELECTRO 2009, Varanasi, Dec. 2009
- [7] Ramesh Garg, Prakash Bhartia, Inder Bahl and Apisak Ittipiboon, Microstrip Antenna Design Handbook, Artech House Publishers, 2001
- [8] IE3D Electromagnetic Simulator from Zeland Software Inc., USA, 2004, Release 10.2
- [9] Internet resource, Applying Error Correction to Network Analyzer Measurements, Agilent application note 5965-7709E, March 27, 2002, Available: <http://www.home.agilent.com>
- [10] Constantine A. Balanis, "Antenna Theory: Analysis and Design", 2nd edition, John Wiley & Sons (Asia) Pte Ltd., Singapore, pp 722-736, 1997

Design and Development of Microstrip Directional Coupler

Bipin Chandra Mandi

Dept. of Electronics and Telecommunication, Jadavpur University Kolkata, India
Email: bipin0087@gmail.com

Abstract: — The directional couplers are used for electromagnetic power flow monitoring in microwave circuits. In this paper 3dB directional coupler in microstrip configuration is designed, developed and evaluated. A good match is obtained between simulated and measured values of the performance characteristics of this directional coupler.

Keywords: Microstrip Directional Coupler, Coupling factor, Insertion Loss, Directivity.

I. INTRODUCTION

The Directional Couplers are four port passive devices. When two transmission lines are close together, because of the interaction of the electromagnetic fields of each line, power can be coupled between the lines to construct directional configurations. Generally, microstrip [1] and stripline [2] forms are used in the design of microstrip directional coupler. Directional couplers are general purpose tools used in RF [3] and microwave signal routing for isolating, separating or combining signals. They find use in a variety of measurement applications: Power monitoring, Source leveling, Isolation of signal sources, Swept transmission and Reflection measurements. As shown in figure 1, Directional Coupler has four ports: Input, Transmitted, Coupled and Isolated.

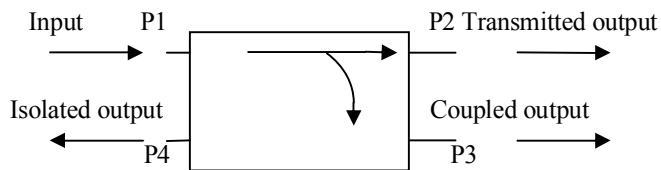


Figure 1. Schematic Diagram of a Directional Coupler

The performance characteristics of a Directional Coupler are defined as given below:

$$\begin{aligned} \text{Coupling factor (dB)} &= 10 \log (P_1/P_3) \\ \text{Insertion Loss (dB)} &= 10 \log [1-(P_3/P_1)] \\ \text{Isolation (dB)} &= 10 \log (P_1/P_4) \\ \text{Directivity (dB)} &= 10 \log (P_3/P_4) \end{aligned}$$

where P1 is the input power at port1, P2 is the transmitted output power at port2, P3 is the coupled power at port3 and P4 is the isolated power at port4.

The rest of this paper is organized as follows: Section II discusses about the design aspects of the microstrip directional coupler. Section III explains about the modeling and

fabrication of the microstrip directional coupler. Section IV describes about the result and discussion. The last section V offers about the conclusion.

II. DISCUSSION OF THE DESIGN ASPECTS OF THE MICROSTRIP DIRECTIONAL COUPLER

The aim of this paper is to design 3dB microstrip directional coupler. The design specifications table is given

Parameters	Specification
Operating Frequency	1GHz
Dielectric substrate	Teflon
Thickness	1/16 inch
Relative permittivity	4.4
Material for ground and patch	Copper

The following equations are in the design of coupled lines

$$\frac{W}{h} = \frac{0.8e^A}{e^{2A} - 2} \quad \text{for } \frac{W}{h} < 2 \quad \dots (1a)$$

$$\frac{W}{h} = \frac{2}{\pi} \left[B - 1 - \ln(2b - 1) + \frac{\epsilon_r - 1}{2\epsilon_r} \left\{ \ln(B - 1) + 0.39 - \frac{0.61}{\epsilon_r} \right\} \right] \quad \text{for } \frac{W}{h} > 2 \quad \dots (1b)$$

where

$$\begin{aligned} A &= \frac{Z_0}{60} \sqrt{\frac{\epsilon_r + 1}{2} + \frac{\epsilon_r - 1}{\epsilon_r + 1} \left(0.23 + \frac{0.11}{\epsilon_r} \right)} \\ B &= \frac{377\pi}{2Z_0\sqrt{\epsilon_r}} \end{aligned}$$

W/h = width and height ratio, ϵ_r = dielectric constant of a homogeneous medium, Z_0 = characteristic impedance.

The effective dielectric constant can be interpreted as the dielectric constant of a homogeneous medium that replaces the air and dielectric regions of the microstrip.

$$\epsilon_e = \frac{\epsilon_r + 1}{2} + \frac{\epsilon_r - 1}{2} \left(\frac{1}{\sqrt{1 + 12d/W}} \right) \dots (2)$$

Having obtained W/h , we can obtain the value of W , which is the width of the microstrip line. Thus the widths of the different strip lines are calculated using the corresponding value of characteristic impedance (Z_0 or $Z_0/\sqrt{2}$) [6]. Until this point, the width of the directional coupler has only been taken care of. But another important parameter for the design of the coupler is its length. In determining length of the directional coupler in order to have better coupling, a design frequency need to be chosen and the length arranged accordingly. Here for better coupling our length consideration is $\lambda/4$. This is because analysis of the coupler shows that maximum coupling occurs at a frequency which gives the quarter wave coupling length, which is $\lambda/4$. This is the mid-band frequency and due to this property, these couplers are also known as quarter-wave couplers. The length of the coupler is calculated using the parameter λ , where, $\lambda = v/f$; v being the phase velocity given by $v = c/\sqrt{\epsilon_{eff}}$. Here c is the speed of light in free space = 3×10^8 m/s, and f is the design frequency. Calculations show that, $W1 (Z_0/\sqrt{2})$ = Width of the broader strip lines = 5.2 mm (approx.), $W2 (Z_0)$ = Width of the thinner strip lines = 3.04 mm (approx.), $L1$ = Length between the thinner strip lines = 40.11 mm (approx.) $L2$ = Length between the broader strip lines = 41.73 mm (approx.) The lengths of the arms connecting the coupler to the four ports are arbitrarily taken as 30 mm.

III. MODELLING AND FABRICATION OF DIRECTIONAL COUPLER

The directional coupler is electromagnetically modeled using the Method of Moments [MoM] based on I3ED simulator shown below: The geometry of the Directional coupler is shown in fig 2.

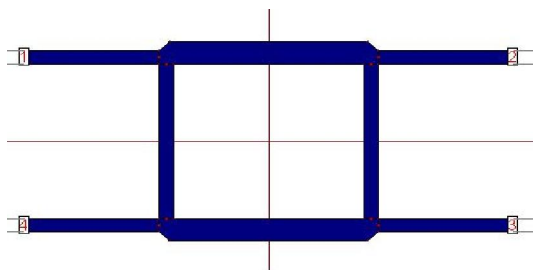


Figure 2. Geometry of Directional Coupler

We observe the following scattering parameters [4] the coupling (S_{31}), insertion loss (S_{21}) and the isolation (S_{41}) over a frequency range of 500 MHz to 2 GHz. The simulated results are as under:

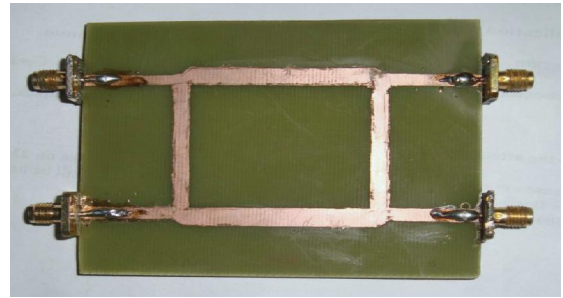


Figure 3. Diagram of fabricated directional coupler

IV. RESULT AND DISCUSSION

The simulated scattering parameters from I3ED simulator are given in figure 4. Mainly three scattering parameters the coupling factor (S_{31}) indicated by yellow color, the insertion loss (S_{21}) indicated by green color and the isolation (S_{41}) indicated by blue color over a frequency.

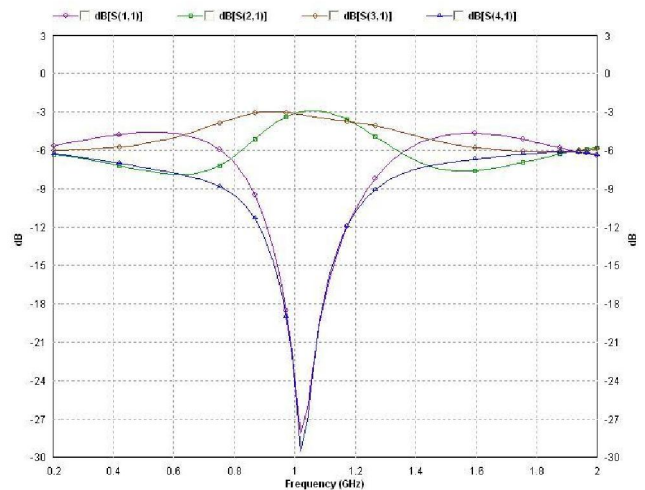


Figure 4. Graph for simulated scattering parameters

The measured results in figure 5(a-c) observed on Agilent made Vector network analyzer.

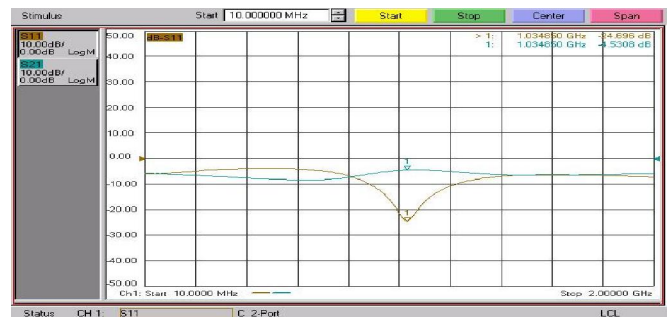


Figure 5(a). S21 vs Frequency

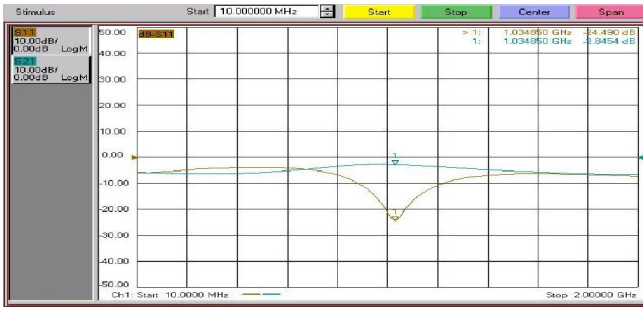


Figure 5(b). S31 vs Frequency



Figure 5(c): S41 vs Frequency

TABLE : COMPARISON OF PRACTICAL AND SIMULATED RESULTS

Parameters	Simulated	Measured
Operating Frequency	1.05 GHz	1.0348GHz
Reflection coefficient (S11)	29.5dB	26.35 dB
Insertion loss (S21)	3.05dB	4.53dB
Coupling factor (S31)	2.9 dB	2.8454 dB
Isolation (S41)	29.7 dB	19.354 dB

The simulated and practical results are shown in this table. Each of the scattering parameters is measured with the other two ports terminated by matched loads (50 ohms).

V. CONCLUSION

A 3dB directional coupler for electromagnetic power flow monitoring in microwave circuits has been designed, developed and evaluated. A close resemblance between the simulated and practical operating frequencies is obtained. The reflection coefficient values at operating frequency are also pretty good. The value of insertion loss and coupling factor are very close to 3dB as per requirements.

ACKNOWLEDGEMENT

The author would like to thank Mr S. Sankaralingam, a Research Scholar of Dept. of ETCE, Jadavpur University for his valuable suggestions and comments in preparing the manuscript.

References

- [1]. Edwards, T. C. Foundations for microstrip circuit design, Wiley Chichester, Wes 1991.
- [2]. Gupta, K. C. Micro strip lines and slot lines / K. C. Gupta, Ramesh Garg, I. J. Bahl. Artech House Dedham, Mass, 1979.
- [3]. Pozar, David M. Microwave Engineering Second Edition, Wiley, New York 1998.
- [4]. C.W. Tang, M.G. Chen, Y.S. Lin and J.W. Wu "Broadband microstrip branch line coupler with defected ground structure" IEEE Electronics Letters, 7th December 2006 (Vol. 42, No. 25).
- [5]. Gardiol, Fred E. Microstrip circuits, Wiley, New York 1994.
- [6]. Fooks, E. H. Microwave engineering using microstrip circuits, Prentice Hall New York 1990.

Text Extraction and Segmentation from Multi-skewed Business Card Images for Mobile Devices

Ayatullah Faruk Mollah

School of Mobile Computing and Communication,
Jadavpur University, Kolkata, India
Email: afmollah@gmail.com

Subhadip Basu, Mita Nasipuri

Department of Computer Science & Engineering,
Jadavpur University, Kolkata, India
Email: {subhadip, mnasipuri}@cse.jdvu.ac.in

Abstract— Text extraction and segmentation are very important steps of Optical Character Recognition (OCR) of image embedded text documents since these images are of multiple natures and often contain graphics, pictures and texts of various fonts and sizes both in background and foreground. So, in order to segment such documents, conventional techniques designed for document images can not be directly applied on mobile devices. In this paper, we have presented text extraction and segmentation techniques for camera captured business card images. At first, foreground components are isolated from each other. Then, the non-textual components are eliminated and the textual ones are skew corrected, binarized and segmented. Experiment shows that the technique is fast, efficient and applicable for mobile devices.

Keywords— Text Extraction, Skew Correction, Binarization, Segmentation, Business Card Reader

I. INTRODUCTION

Optical Character Recognition (OCR) of printed document images is a well researched topic. But, it is limited to simple document images. The performance of such systems is significantly hampered when applied on images of complex documents such as business cards. Such document images contain wide variety of texts, graphics, images, etc. Many a times, texts are written in artistic fashion and images overlap with texts. At the same time, pervasive availability of low cost portable imaging devices has made digital camera so popular that majority of the mobile devices such as cell-phones and Portable Digital Assistants (PDA) have inbuilt digital camera. The resolution of these cameras is getting increased day by day. The computing power and memory of the mobile devices are also gradually going higher. So, the idea of image processing and analysis is no more limited to desktop computers. Researchers have paid significant attention towards developing Optical Character Recognition (OCR) systems for document images on mobile devices too. Unlike scanned document images, camera captured document images suffer from blur, shadow, skew, perspective distortion etc. On the other hand, mobile devices are portable and so more useful than scanners for document processing, particularly for capturing and processing any arbitrary documents such as thick books, fragile documents like old historical manuscripts, scene texts, caption texts, graphic texts, etc.

Business Card Reader (BCR) for mobile devices is such a useful application of camera captured document image processing. With the development of an efficient BCR system, the information of the acquired business card images can be directly populated to the contact profile of the mobile devices. Thus, the business card management will be of great ease than ever before. One would have to neither carry the business card album nor have to type the information of the cards to populate into the handheld devices.

Major challenges of designing such a system include text extraction and segmentation from captured business card images. Business card images often have complex background and texts of multiple natures. These images may contain logo, picture, texts of different fonts and various font sizes, graphic background, etc. Moreover, different components of the image are skewed at different angles because of perspective projection. Therefore, segmentation can not be done straight forward and we found that neither global nor locally adaptive binarization techniques [1-4] can help segmentation of business card images.

Until recently, various text extraction methods have been proposed and evaluated, of which most of them are for document images. Some have been proposed for business card images captured with a built-in camera of a mobile device [5-7]. Few other text extraction methods are reported in [8-10]. DCT and Information Pixel Density have been used to analyse different regions of a business card image in [5]. In [6], a low resource consuming region extraction algorithm has been proposed for mobile devices with the limitation that the user needs to manually select the area in which the analysis would be done and the success rate is yet to be improved. Pilu et al. [7] in their work on light-weight text image processing for handheld embedded cameras, proposed a text detection method that can not remove the logo(s) of a card and may mistake parts of the oversized fonts as background and can not deal with reverse text. In [8], text lines are extracted from Chinese business card images using document geometrical layout analysis method. Fisher's Discrimination Rate (FDR) based approach followed by various text selection rules is presented in place of mathematical morphology based operations [9]. Yamaguchi et al. [10] has designed a digit extraction method in the works of telephone number identification and recognition from signboards by eliminating

noise using Roberts filter, and then applied different text identification rules.

Some of the above methods seem to be computationally expensive and the rest needs more efficiency. In this paper, we have presented a computationally efficient rule-based text extraction and segmentation method that works satisfactorily for camera captured business card images under the computing constraints of mobile devices.

II. THE PRESENT METHOD

Foreground components are generated by removing background as discussed in Section II-A. Then the foreground non-textual elements are removed as explained in Section II-B. After that the image is expected to contain only text regions. These text regions are skew corrected as illustrated in Section II-C. Skew corrected text regions are binarized in Section II-D. And finally, binarized text regions are segmented as discussed in II-E.

A. Foreground Component Generation

The entire image is at first divided into blocks of a fixed size. The more is the length of the block, the more is the number of horizontally contiguous words included in a single text region. And similarly, the less the height of the block is, the less is the possibility that a block covers more than one text lines. So, we have mostly experimented with rectangular blocks. The width and height is varied and tuned for best results and we found that it works well for the block of width $W/64$ (W is the width of the card image) and height of 2 pixels. Next, we classify each block as either an information block or a background block based on the intensity variation within it. An information block belongs to either a text region or an image region including noise. The motivation behind this approach is that the intensity variation is low in case of background blocks and high in case of information blocks. So, if the intensity variation of a block is lesser than a dynamically generated threshold (T_σ) as given in Eq. (1), it is considered as a background block. Otherwise, the block is considered as an information block. But, no block is classified as background until the minimum intensity within the block exceeds a heuristically chosen threshold (T_{min}). The formulation of T_σ is described below.

$$T_\sigma = T_{fixed} + T_{var} \quad (1)$$

$$T_{var} = [(G_{min} - T_{min}) - \min(T_{fixed}, G_{min} - T_{min})] * 2 \quad (2)$$

where, G_{min} and G_{max} are respectively the minimum and maximum gray level intensity of the pixels in a block and T_{fixed} is the minimum intensity tolerance subject to tuning.

All the pixels of the blocks identified as background in this section are assigned the maximum intensity i.e. 255 to denote that they are part of the background. This makes the foreground components distinct from each other.

B. Component Classification

The standard 4-connected region growing algorithm [11] is applied to identify the distinct foreground Connected Components (CC) from background eliminated card images.

A CC may be a picture, logo, texture, graphics, noise or a text region. In the current work, we focus to identify only the text regions using rule-based classification technique. The following features are used to classify a CC under consideration as a text region or not.

The height, width, width to height ratio (aspect ratio), gray pixel density, black pixel density, number of vertical and horizontal segments, and the number of cuts along the middle row of the CC are considered as features to decide upon the characteristic of each CCs. Different heuristically chosen adaptive (with respect to the size/resolution of the input image) thresholds are estimated for designing the rule-based classifier for text/graphics separation. Too small regions that are unlikely to become text regions and horizontal/vertical lines detected by checking their width, height and aspect ratio are considered as non-text components. Typically, a text region has a certain range of width to height ratio (R_{w2h}). So, we consider a CC as a potential text region if R_{w2h} lies within the range (R_{min}, R_{max}). We assume that neither horizontal nor vertical lines can be drawn through a logo and it is larger than the largest possible character within the card. Thus, logos and other components satisfying the above specification get eliminated. Another important property of text regions is that the number of foreground pixels in a text region is significantly less than that of the background pixels. We consider a certain range of ratio of the foreground pixels to the background (RA_{cc}) given by (RA_{min}, RA_{max}) for the candidate text regions.

C. Skew Correction

Skew angle is estimated for each text region and then the text region is rotated accordingly to get it skew corrected. To calculate the skew angle, we consider the bottom profile of the gray shade of a text region. It may be noted that the gray shade is the background of the card around the text strokes. It is based on the observation that the background of a camera captured card image is not of the maximum intensity. The profile contains the heights in terms of pixel from the bottom edge of the bounding rectangle formed by the text region to the first gray/black pixel found while moving upward. However, if the extent of the gray shade along the column of a profile is too small, we discard it considering an invalid profile.



Fig. 1: Skew Angle Computation

As the profile is ready, we calculate the mean (μ) and the mean deviation (τ) of heights as shown in Eq. 3 and 4 respectively. The computation of mean deviation does not involve floating point arithmetic. Although, we can convert the floating point arithmetic to integer one, we want to avoid it as our intent is to embed the method on mobile devices that usually do not have a Floating Point Unit (FPU). Then, we exclude some elements of the profile that are not in sync with

the others i.e. not within $(+\tau, -\tau)$. These elements hardly contribute to the actual skewness of the text region and so get eliminated.

$$\mu = \frac{1}{N} \sum_{i=0}^{N-1} h[i] \quad (3)$$

$$\tau = \frac{1}{N} \sum_{i=0}^{N-1} |\mu - h[i]| \quad (4)$$

where N is the profile length, h is the profile array and $h[i]$ denotes the height at i^{th} position.

Among the remaining profile elements that really contribute to the actual skewness of the text regions, we consider the leftmost ($h1$), rightmost ($h2$) and the middle profile element ($h3$) as shown in Fig. 1. The distance between $h1$ and $h2$ is computed as d . Then, the individual skew angles for the slope between $h1$ and $h2$ (α), $h1$ and $h3$ (β), and $h2$ and $h3$ (γ) are computed as formulated in Eq. 5-7 respectively. Now, ideally they should be the same. We introduce a threshold (ε) to allow a certain deviation in between them. So, if none of the deviations between any two of α , β and γ is more than ε , we take an average and rectify the skew of the text region. Otherwise, we look forward to the top profile of the text region and compute the skew angle. Respective skew angles as computed from the top profile of the text region are α' , β' and γ' . If these are found to be inline, we take an average of them and rectify the skew. Else, the smaller one between the averages obtained from top and bottom profiles is considered as the skew angle. It may be noted that this approach gives a mean to bypass some computation if not required.

$$\alpha = \arctan\left(\frac{\delta h}{d}\right), \delta h = h2 - h1 \quad (5)$$

$$\beta = \arctan\left(\frac{\delta h}{d}\right), \delta h = h3 - h1 \quad (6)$$

$$\gamma = \arctan\left(\frac{\delta h}{d}\right), \delta h = h2 - h3 \quad (7)$$

TABLE I
BINARIZATION ALGORITHM

for all pixels (x, y) in a CC if $Intensity(x, y) < (G_{min} + G_{max})/2$, then mark (x, y) as foreground else if no. of foreground neighbors > 4 , then mark (x, y) as foreground else mark (x, y) as background end if end if end for

D. Binarization of Text Regions

As a CC is classified as a text region, it is binarized with an adaptive yet simple technique. If the intensity of a pixel within the CC is less than the mean of the maximum and minimum intensities of a CC, it is taken as a foreground pixel. Otherwise, we check the 8 neighbors of the pixel and if any 5 or more neighbors are foreground, then also we consider the pixel as a foreground one. It may be noted that the border pixels do not have 8 neighbors and so will not be subject to this technique. The remaining pixels are considered as part of the background. The algorithm is given in Table I.

The advantage of this approach of binarization is that the disconnected foreground pixels of a character are likely to be connected due to neighborhood consideration. Instead of having efficient binarization techniques, we have designed this simple algorithm keeping the computational constraints of the mobile devices in view.

E. Character Segmentation

A text region extracted with the present technique may have multiple lines. We segment the text regions into text lines and then characters are segmented from them. Horizontal histogram profile is analyzed for line segmentation. All possible line segments are determined by comparing the profile elements with a considerably large threshold. After that the inter-segment distances are analyzed and some segments are rejected. The central idea behind this technique is that the distance in terms of pixel between two lines will not be too small and the inter-segment distances are likely to become equal.

III. EXPERIMENTAL RESULTS AND DISCUSSION

We have experimented on a dataset of 100 business card images of various types acquired with a cell-phone camera (Sony Ericsson K810i) to evaluate the performance of the present technique. The dataset consists of both simple and complex cards containing complex backgrounds and logos. Some cards contain multiple logos and some logos are combination of text and image. Most of the images are skewed, perspective distorted and degraded.

A. Text Extraction Accuracy

Ground truth images are compared with the resultant images for evaluating the performance of the present technique. A component may be either a text or a graphic component. Here, a graphic component refers to all non-text regions including background texture and noises. Based on the presence of a component in either or both the ground truth image (GT) and the output image (OUT), we count the number of true positive (C_{TP}), false positive (C_{FP}), true negative (C_{TN}) and false negative (C_{FN}).

The recall (R), precision (P) and accuracy (A) rates are calculated as formulated in Eq. 8-10. The recall parameter signifies how many text components have been correctly identified among all the text components in the ground truth image, whereas the precision factor signifies how many text components identified in the resultant image are truly text components. In an ideal situation R , P and A should be all 100 %.

$$R = \frac{C_{TP}}{C_{TP} + C_{FN}} \quad (8)$$

$$P = \frac{C_{TP}}{C_{TP} + C_{FP}} \quad (9)$$

$$A = \frac{C_{TP} + C_{TN}}{C_{TP} + C_{FP} + C_{TN} + C_{FN}} \quad (10)$$

Experiments have been conducted with images of various resolutions of the same set of business cards with different values of the following parameters. However, a fairly good result is achieved with $T_{fixed} = 20$, $T_{min} = 100$, $H_{TH} = H/60$, $W_{TH} = W/40$, $A_{TH} = W*H/1500$, $B_{TH} = H/100$, $L_{TH} = W/40$, $R_{min} = 1.2$, $R_{max} = 32$, $RA_{min} = 5$ and $RA_{max} = 90$. The mean R , P and A as obtained with various resolutions are shown in Table II.

TABLE II
TEXT EXTRACTION PERFORMANCE WITH VARIOUS RESOLUTIONS

Resolution	Recall	Precision	Accuracy
640x480 (0.3 MP)	98.07	97.21	96.69
800x600 (0.45 MP)	98.40	94.59	96.00
1024x768 (0.75 MP)	98.25	96.77	97.38
1182x886 (1 MP)	98.35	95.29	96.66
1672x1254 (2 MP)	98.23	96.60	97.66
2048x1536 (3 MP)	98.96	97.21	98.00

B. Text Segmentation Accuracy

Character segmentation accuracy has been estimated in terms of the ratio of the number of correct segmented characters to the total number of characters present in a card image. A character is categorized as incorrectly segmented one if it is over-segmented or is segmented as a part of another character.

By following this estimation technique we found that the character segmentation accuracy is 97.48% in case of 3 MP images. It may be noted that the present segmentation technique is not meant for italic and cursive texts. So, such texts have been ignored while calculating the segmentation accuracy.

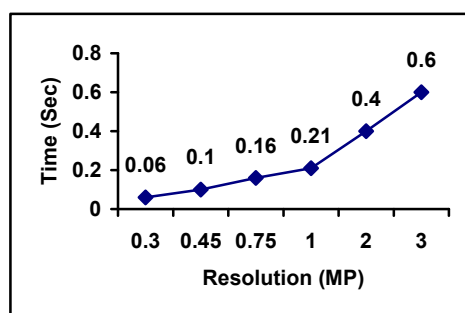


Fig. 2: Computation Time with Various Resolutions

C. Applicability on Mobile Devices

The applicability of the presented technique on mobile devices is checked by its computational requirements. As our

aim is to deploy the proposed method into mobile devices, we want to develop a light-weight Business Card Reader (BCR) system beforehand and then to embed into the devices.

An observation [12] reveals that the majority of the processing time of a camera based optical character recognition (OCR) engine embedded into a mobile device is consumed in preprocessing including binarization. Although, we have shown the computational time of the presented method with respect to a desktop, the total time required to run the developed method on mobile devices will be tolerable. Fig. 2 shows the computation time with various resolutions.

As, limited memory is another constraint of the mobile devices, the presented method is designed to work with low memory requirement. Memory consumption is approximately 2-3 folds of the input image size.

IV. CONCLUSIONS

We have presented and evaluated a method of text extraction and segmentation of mobile camera captured business card images and our experiments show that the result is satisfactory. It has been observed from this experimentation, that with the increase in image resolution, the computational time and memory requirements increase proportionately. Although, the maximum text region isolation accuracy is obtained with 3 mega pixel resolution, it involves high memory requirement and 0.6 seconds of processing time. It is evident from the findings that the optimum performance is achieved at 1024x768 (0.75 MP) pixels resolution with a reasonable accuracy of 97.38% and significantly low (in comparison to 3 MP) processing time of 0.16 seconds.

ACKNOWLEDGMENT

Authors are thankful to the *Center for Microprocessor Application for Training Education and Research (CMATER)* and project on *Storage Retrieval and Understanding of Video for Multimedia (SRUVM)* of the Department of Computer Science and Engineering, Jadavpur University for providing infrastructural support for the research work. We are also thankful to the *School of Mobile Computing and Communication (SMCC)* for proving the research fellowship to the first author.

REFERENCES

- [1] N. Otsu, A threshold selection method from gray level histogram, *IEEE Transaction SMC-9*, pp. 62-66, 1979
- [2] W. Niblack, *An Introduction to Image Processing*, Prentice-Hall, Englewood Cliffs, NJ, 1986, pp. 115-116
- [3] O. D. Trier, Goal-directed evaluation of binarization methods, *IEEE PAMI* Vol. 17, No. 12, 1995
- [4] J. Sauvola and M. Pietikainen, Adaptive document image binarization, *Pattern Recognition*, Vol. 33, pp. 225-236, 2000
- [5] Jang, I. H., Kim, C. H. and Kim, N. C. (2005). Region Analysis of Business Card Images in PDA Using DCT and Information Pixel Density. *Proceedings of the Advanced Concepts for Intelligent Vision Systems*, Belgium, 243-251.
- [6] Guo, J. K., and Ma, M. Y. (2007). A Low Resource Consumption Image Region Extraction Algorithm for Mobile Devices. *Proceedings of the IEEE International Conference on Multimedia & Expo*, Beijing, China. 336-339.
- [7] Pilu, M. and Pollard, S. (2002). A light-weight text image processing method for handheld embedded cameras. *Proceedings of the British*

- Machine Vision Conference. UK. (<http://www.hpl.hp.com/personal/mp/docs/bmvc2002-textpipeline.pdf>)
- [8] Pan, W., Jin, J., Shi, G. and Wang, Q. R. (2001). A System for Automatic Chinese Business Card Recognition. Proceedings of the International Conference on Document Analysis and Recognition. USA. 577-581.
 - [9] Ezaki, N., Kiyota, K., Minh, B.T., Bulacu, M., and Schomaker, L. (2005). Improved Text-Detection Methods for a Camera-based Text Reading System for Blind Persons. Proceedings of the International Conference on Document Analysis and Recognition. Korea. 257-261.
 - [10] Yamaguchi, T., Nakano, Y., Maruyama, M., Miyao, H., and Hananoi, T. (2003). Digit Classification on Signboards for Telephone Number Recognition. Proceedings of the International Conference on Document Analysis and Recognition. UK. 359-363.
 - [11] E. Gose, R. Johnsonbaugh, S. Jost, "Pattern Recognition and Image Analysis", Prentice-Hall of India, Eastern Economy Edition, pp. 334.
 - [12] M. Laine and O. S. Nevalainen, A Standalone OCR System for Mobile Cameraphones, 17th Annual IEEE International Symposium on Personal, Indoor and Mobile Radio Communications, Sept. 2006, pp. 1-5.

Image Secret Sharing Scheme Using a Novel Secret Sharing Technique with Steganography

Prabir Kr. Naskar
cse.prabir@gmail.com

Ayan Chaudhuri
ayanchaudhuri27@gmail.com

Atal Chaudhuri
atalc@hotmail.com

Dept. of Computer Science & Engineering
Jadavpur University, Kolkata 700032

Abstract:

Secret sharing is a technique for protecting sensitive data, such as cryptographic keys. Well known secret sharing schemes in literature include Shamir[1], Blakley[2] and Asmuth-Bloom[3] leading to high computational complexity during both sharing and reconstructing and also generates noise like shares. To create meaningful shares, Lin and Tsai[13] proposed a method that uses Steganography using Shamir's secret sharing scheme, again that led to high computational complexity. To overcome above problem, we are suggesting a scheme which deploys simple graphical masking method, done by simple ANDing for share generation and reconstruction can be done by simple ORing the qualified set of shares. Also, this proposed method finally creates meaningful shares by using Steganography instead of noise like shares.

Keywords: Secret sharing, Steganography, Low computational complexity

1 Introduction

Steganography is a method to protect data from illicit attacks. This method hides a secret message in a cover medium to avoid malicious eyes. The cover could be a digital image, video, audio, or even html code. Attackers fail to guess whether the cover medium has hidden secret data or not. Therefore, they will not aim to do anything on these apparently innocent covers to extract the original data. Efficient cryptographic methods are there to protect sensitive data using Steganography. However, a common weakness of this technique is that an entire protected data or image is kept in a single cover medium. The secret data or image cannot be revealed if the medium is lost or corrupted. Secret sharing is a technique that deals with such problem, namely, sharing a highly sensitive secret among a group of

n users so that only when a sufficient number k of them comes together, the secret can be constructed.

The first idea of secret sharing was proposed individually by Adi Shamir and George Blakley in 1979. Shamir's[1] scheme based on polynomial interpolation where as Blakley[2] scheme based on hyper plane geometry. Also there is secret sharing scheme that makes use of the Chinese Remainder Theorem namely Asmuth-Bloom's[3] scheme, in which the shares are generated by reduction modulo operation and the secret is recovered by essentially solving the system of congruence using the Chinese Remainder Theorem.

A shortcoming of above secret sharing schemes is the need to reveal the secret shares during the reconstruction phase. The system would be more secure if the subject function can be computed without revealing the secret shares or reconstructing the secret back. This is known as function sharing problem where the function's computation is distributed according to underlying SSS such that distributed parts of computation are carried out by individual user and then the partial results can be combined to yield the final result without disclosing the individual secrets. Various function sharing protocols are been proposed [4], [5], [6], [7], [8], [9], [10] mostly based on Shamir's secret sharing as the underlying scheme. Some work [11] is also available on Blakley's secret sharing scheme and Asmuth-Bloom scheme [12] as well.

In 2004, Lin and Tsai[13] proposed a method that used Steganography for generation of meaningful shares with secret image sharing. Yang et al. proposed a method to overcome some of the weakness in the method in 2007 [14]. But both the studies used polynomial-based secret sharing approach proposed by Shamir. That led to high computational complexity.

In this paper we have suggested a secret sharing scheme absolutely different from any of the schemes discussed so far, where simple ANDing

operation is used for share generation and reconstruction can be done simply ORing the predefined minimal set of shares. Not only the generated shares are kept into meaningful cover images but the novelty of the scheme depends upon the technique of generating individual masks to be used for ANDing over the original secret for share generation. A step wise algorithm is suggested for such mask design for any (n, k) scheme where n number of masks are designed to generate n different shares and any k shares ($k < n$) on ORing reconstruct the original secret. [The proof in support of the correctness of the algorithm is available in [15] our immediate previous work.]

2 Secret Sharing Algorithm

The proposed work is based upon a novel secret sharing scheme which employs simple graphical masking method using simple ANDing for share generation and reconstruction can be done by simple ORing the predefined minimal number of shares.

2.1 Concept

For better understanding let us consider any secret as a binary bit file (i.e. bit is the smallest unit to work upon, in actual implementation one can consider a byte or group of bytes or group of pixels as the working unit). The secret could be an image, an audio or text etc. We shall decompose the bit file of any size onto n shares in such a way that the original bit file can be reconstructed only ORing any k number of shares where $k \leq n \geq 2$ but in practice we should consider $2 \leq k < n \leq 3$.

Our basic idea is based on the fact that every share should have some bits missing and those missing bits will be replenished by exactly $(k-1)$ other shares but not less than that. So every individual bit will be missed from exactly $(k-1)$ shares and must be present in all remaining $(n-k+1)$ shares, thus the bit under consideration is available in any set of k shares but not guaranteed in less than k shares. Now for a group of bits, for a particular bit position, $(k-1)$ number of shares should have the bit missed and $(n-k+1)$ number of shares should have the bit present and similarly for different positions there should be different combinations of $(k-1)$ shares having the bits missed and $(n-k+1)$ number of shares having the bits present. Clearly for every bit position there should be ${}^nC_{k-1}$ such combinations and thus in our scheme every mask is of size ${}^nC_{k-1}$, which will be

repeatedly ANDed over the secret in any regular order. Different masks will produce different shares (*The style of placing the mask over the secret could be anything but it will be same for every share. It may also be noted that the knowledge of positioning the masks over the secret is not at all required for reconstruction of the secret.*) from the original secret. Thus 0 on the mask will eliminate the bit from the secret and 1 in the mask will retain the bit to form a share. Every mask having unique 1 and 0 distribution will thus generate unique share.

Next just ORing any k number of shares we get the secret back but individual share having random numbers of 1's & 0's reflect no idea about the secret. As an example a possible set of masks for 5 shares with threshold of 3 shares is shown below:

Share 1:	1 1 1 1 1 1 0 0 0 0
Share 2:	1 1 1 0 0 0 1 1 1 0
Share 3:	1 0 0 1 1 0 1 1 0 1
Share 4:	0 1 0 1 0 1 1 0 1 1
Share 5:	0 0 1 0 1 1 0 1 1 1

One can easily check that ORing any three or more shares we get all 1's but with less than three shares some positions still have 0's i.e. remain missed.

2.2 Algorithm

Here we are presenting the algorithm for designing the masks for n shares with threshold k .

Step-1: List all row vectors of size n having the combination of $(k-1)$ numbers of 0's and $(n-k+1)$ numbers of 1's and arrange them in the form of a matrix. Obvious dimension of the matrix will be ${}^nC_{k-1} \times n$.

Step-2: Transpose the matrix generated in Step-1. Obvious dimension of the transposed matrix will be $n \times {}^nC_{k-1}$. Each row of this matrix will be the individual mask for n different shares. The size of each mask is ${}^nC_{k-1}$ bits, i.e. the size of the mask varies with the value of n and k . Each row of this matrix is to be used as mask in generation the corresponding share.

(It may be noted that the masking patterns are not unique. Different arrangements of the row vectors in Step-1 leads to different sets of masks but for a particular set, the masks are unique and they satisfy the requirements.)

Let us consider the previous example where $n=5$ and $k=3$.

Step-1: List of row vectors of size 5 bits with 2 numbers of 0's and 3 numbers of 1's.

1	1	1	0	0
1	1	0	1	0
1	1	0	0	1
1	0	1	1	0
1	0	1	0	1
1	0	0	1	1
0	1	1	1	0
0	1	1	0	1
0	1	0	1	1
0	0	1	1	1

Dimension of the matrix is ${}^5C_2 \times 5$ i.e. 10×5

Step-2: Take the transpose of the above matrix and we get the desired masks for five shares as listed above in the form of matrix of dimension $5 \times {}^5C_2$ i.e. 5×10 . There are five masks each of size 10 bits.

3 Image Secret Sharing Protocol

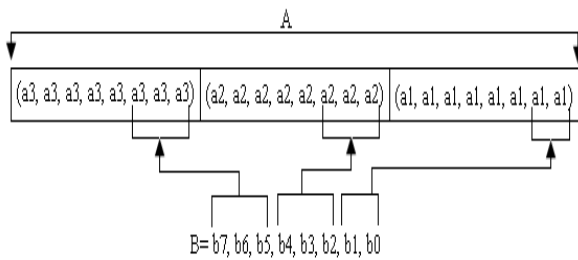
Here we are presenting stepwise protocol for image secret sharing scheme.

Input : a secret image $S (x \times x)$ and n cover images $(3x \times x)$.

Output : n stego images $(3x \times x)$.

Encode:

First mask pattern is placed repeatedly on the secret image. The bytes corresponding to 1 in the mask are kept as it is and the bytes corresponding to 0 in the mask are replaced by 0. For each masked byte (say B), select a pixel (say A) comprising of three bytes for RGB values from the corresponding cover image. Then insert the eight bits of byte B by replacing the LSB bits of the three consecutive bytes of the cover as follows:



This forms the first stego image. Same is repeated with all other mask patterns to form others stego images respectively. (The change of RGB values upto 3 LSB bits is imperceptible to human eyes.)

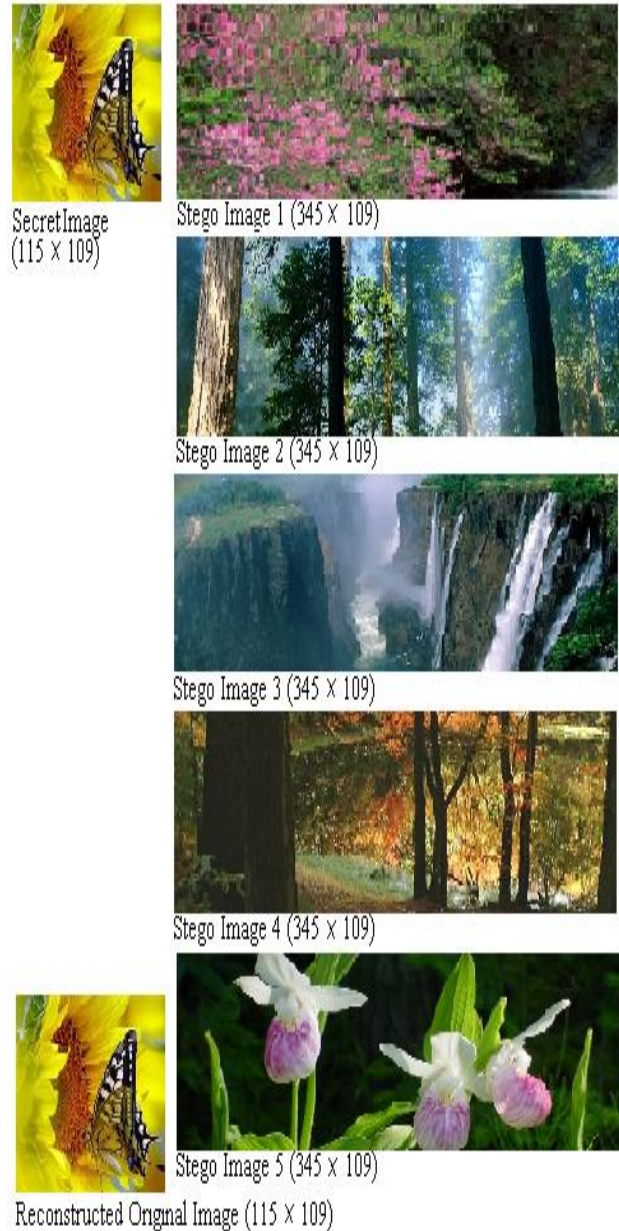
Decode:

First select any k or more stego images (i.e. shares), From all k stego images select the corresponding pixel and extract the share bytes B_i where $i=1, 2, \dots, k$ from the stego images. Now by simply ORing these k bytes we get the corresponding secret byte. Thus the secret byte is

$$B_s = B_1 \text{ OR } B_2 \text{ OR } \dots \text{ OR } B_i \text{ OR } \dots \text{ OR } B_k$$

Same is repeated with all pixels of k stego images to get back the secret image $S (x \times x)$. Thus the original lossless secret image is reconstructed, effective computational overhead is zero.

Let us take an example with $n=5$ and $k=3$.



Using any 3 or more stego Images

Fig.1: Original Secret image (115×109) , Five Stego images (345×109) and reconstructed Secret image (115×109) .

4 Conclusion

We have presented a novel secret sharing approach with minimal computational overhead if not nil. To the best of our knowledge this is the simplest threshold sharing scheme, practically having no computational overhead during both share generation and secret reconstruction. However, for steganography purpose our method needs cover image size bigger than the secret. Our future effort is to reduce the size of the cover image further i.e. cover image size may be lesser than the secret. Moreover we have used the simplest watermarking scheme for stego image shares. We can always use any of many robust watermarking techniques available on demand of the application.

References

- [1] A. Shamir: "How to share a secret ?" Comm ACM, 22(11):612-613, 1979.
- [2] G. Blakley : "Safeguarding cryptographic keys " Proc. of AFIPS National Computer Conference, 1979.
- [3] C. Asmuth and J. Bloom : "A modular approach to key safeguarding" IEEE transaction on Information Theory, 29(2):208-210, 1983.
- [4] Y. Desmedt "Some recent research aspects of threshold cryptography" Proc of ISW'97 1st International Information Security Workshop vol.1196 of LNCS paper 158-173 Springer-Verlag 1997.
- [5] Y. Desmedt and Y. Frankel "Threshold cryptosystems" Proc of CRYPTO'89 volume 435 of LNCS, paper 307-315 Springer Verlag 1990.
- [6] Y. Desmedt and Y. Frankel "Shared generation of authenticators and signatures" Proc. of CRYPTO'91 volume 576 of LNCS pages 457-469 Springer Verlag 1992.
- [7] Y. Desmedt and Y. Frankel "Homomorphic zero knowledge threshold schemes over any finite abelian group" SIAM journal on Discrete Mathematics 7(4): 667-675, 1994.
- [8] H. F. Huang and C.C. Chang "A novel efficient (t, n) threshold proxy signature scheme" Information Sciences 176(10): 1338-1349, 2006.
- [9] A. De Santis, Y. Desmedt, Y. Frankel and M. Yung "How to share a function securely ?" In proc of STOC 94, paper 522-533, 1994.
- [10] V. Shoup "Practical threshold signatures" In Proc of Eurocrypt 2000. volume 1807 of LNCS paper 207-220, Springer-Verlag 2000.
- [11] Bozkurt, Kaya, Selcuk, Guloglu "Threshold Cryptography Based on Blakely Secret Sharing" Information Sciences.
- [12] K. Kaya and A. A. Selcuk "Threshold Cryptography based on Asmuth-Bloom Secret Sharing" Information Sciences 177(19) 4148-4160, 2007
- [13] C.C. Lin and W.H. Tsai, "Secret image sharing with steganography and authentication", Journal of Systems and software, vol. 73, no. 3, pp. 405-414, 2004.
- [14] C.N. Yang, T.S. Chen, K.H. Yu, and C.C. Wang, "Improvements of image sharing with steganography and authentication", Journal of Systems and Software, vol. 80, no. 7, pp. 1070-1076, 2007.
- [15] S. Guha, S. Das, S. Sarkar and A. Chaudhuri "Visual Cryptography using pixel filtering technique for continuous tone 24-bit image" Proc of National Seminar on Role of ICT in improving Quality of life Page 61-72, 2010.

Authorship Identification Using Stylometry Analysis: A CRF Based Approach

Tanmoy Chakraborty

Department of Computer Science and Engineering
Jadavpur University
Kolkata, India
its_tanmoy@yahoo.co.in

Sivaji Bandyopadhyay

Department of Computer Science and Engineering
Jadavpur University
Kolkata, India
sivaji_cse_ju@yahoo.com

Abstract— Stylometry, which is defined as the science of inferring characteristics of the author from the characteristics of documents written by that author, is a problem which belongs to the core task of Text categorization e.g. authorship identification, plagiarism detection etc. In this work, we present a strategy for authorship identification of the documents written in Bengali. It takes into account a write-independent model and builds a robust system which reduces the pattern-recognition problem. Conditional Random Field (CRF) model is a state-of-the-art sequence labeling model which can use the feature of the documents more efficiently. We adopt a set of fine-grained attribute features for the analysis of the text and use them to train the CRF model. As an initial approach, we have also used a statistical similarity approach for authorship identification using same feature set. Evaluation results of both systems for Bengali author's Stylometry detection shows reasonably promising accuracy in comparison to proposed baseline system.

Keywords—Stylometry, Conditional Random Field, Cosine-similarity, hapax legomena, authorship identification.

I. INTRODUCTION

Stylometry is an approach that analyses text in text mining e.g. novels, stories, dramas that the famous authors wrote, trying to measure the author's style, rhythm of his pen, subjection of his desire, prosody of his mind by choosing some attributes that are consistent throughout his writing, which plays the linguistic fingerprint of that author. Simply, Stylometry is the application of the study of linguistic style, usually to written language which concerns the way of writing rather than its contents. Stylistic analysis that has been done by Croft [2] claimed that for a given author, the habits "of style" are not affected "by passage of time, change of subject matter or literary form. They are thus stable within an authors writing, but they have been found to vary from one author to another" [8]. Authorship identification belongs to the subtask of Stylometry detection where a correspondence between the predefined writers and the unknown articles has to be established considering various stylistic features of the documents. In order to identify the author, one must extract the most appropriate features to represent the style of that author. In this context, the Stylometry offers a strong support to define a discriminative feature set. The literature shows that most of the features are drawn from the lexical aspects and they are strongly dependent on the length of the document under study and are difficult to apply reliably.

In this paper, we have tried to adapt a system beyond the conventional approaches of Stylometry detection. For this, Conditional Random Field (CRF) model has been

introduced very first time in this field of application and features have been selected after microscopic investigation of the contextual information of the documents. We have also proposed a statistical approach for comparing the results with the previous one. We have used the articles which were written by the famous novel laureate Rabindranath Tagore long years back and try to dissimilate them from the anonymous articles written by other authors at that period of time. In the rest of the article, we use the expressions *Stylometry detection* and *authorship identification* interchangeably to express their anonymous senses. Experimental results indicate that the CRF model can enhance the task of identifying the authors.

The rest of this paper is organized as follows: the next section reviews some related work of Stylometry and authorship identification. In Section III, the detailed description of our proposed approach is presented. Subsequently in Section IV, the proposed system architecture and the components are discussed. The experimental results that evaluate the procedure are mentioned in Section V. The paper is concluded with summery and future work direction.

II. RELATED WORK

There exists a long history of linguistic and stylistic investigation into author identification which goes back to the nineteenth century, with the pioneering studies of Mendenhall [11] on distribution of sentence and word lengths in works of literature and the gospels of the New Testament. After that, a number of studies based on computational stylistic approach [4], content analysis [5], exponential gradient learn algorithm [7], Winnow regularized algorithm [9], Support Vector Machine based approach [3] etc have been proposed for various languages like English, Portuguese. The use of computers regarding the extraction of Stylometry has been limited to auxiliary tools (i.e. simple program for counting user-defined features fast and reliably). Hence, authorship attribution studies so far may be looked like *computer-assisted*, not *compute-based*. As a beginning of Indian language Stylometry analysis, this research does not considered any manual intervention of extracting features and introduce CRF for the first time for authorship identification. Moreover we have dealt with a number of large-size non-homogeneous texts since they are composed of dialogues, narrative parts etc and try to build a language-independent system for attribute analysis.

III. OUR APPROACH

In this experiment, we have explored some stylistic features looking at the contextual level of the text and used those features for training purpose of the CRF. Authorship

identification task can be thought of mapping the test documents into the proper clusters where clusters are the group of articles of different writers. Here, we have grouped the training documents into three clusters and same features have been extracted from each cluster. These features can be thought of the dimensions of the articles in an n-dimensional space. At the same time, we have also measured a statistical approach (Cosine-similarity) to draw a relative study between statistical and machine learning approaches. As this is the first attempt in Bengali language, there is no baseline system for evaluation. We have assumed a baseline system for evaluating both of our systems. Currently, authorship attribute studies are dominated by the use of lexical measures. In a review paper [1], the author asserted that:

“..... yet, to date, no stylometrist has managed to establish a methodology which is better able to capture the style of a text than based on lexical items.”

Therefore, we have decided to implement a lexically-based approach called *vocabulary richness* as our baseline system because this is a traditional methodology and till now, most successful one comparing to the other studies in this field. In rest of this section, we give a brief overview of CRF model, cosine-similarity measure and then discuss the architecture of our system in details.

A. Conditional Random Field (CRF) Model

Conditional Random Field (CRF) is a new probabilistic model for segmenting and labeling sequence data [12]. CRF is an undirected graphical model that encodes a conditional probability distribution with a given set of features. For the given observation sequential data $X(X_1X_2...X_n)$, and their corresponding status label $Y(Y_1Y_2...Y_n)$, a linear chain structure which CRF defines as the conditional probability as follows:

$$P(Y|X) = \frac{1}{Z_x} \exp\left(\sum_i \sum_j \lambda_j f_j(y_{i-1}, y_i, X, i)\right)$$

where, Z_x is a normalization and it makes the probability of all state sequences sum to 1. Function inside the summation is the feature function and λ_j is a learnt weight associated with the feature f_j . Maximum entropy learning algorithm can be used to train CRF. For the given observation sequential data, the most probable sequence can be determined by

$$Y^* = \arg \max_j P(Y|X)$$

where, Y^* can be efficiently determined using Viterbi algorithm. An N-best list of labeling sequences can also be obtained using modified Viterbi algorithm and A^* search.

The main advantage of CRF comes from that it can relax the assumption of conditional independence of the observed data often used in generative approaches, an assumption that might be too restrictive for a considerable number of object classes.

B. Cosine-similarity Measures

Cosine-similarity is a measure of similarity between two vectors of n dimensions by finding the cosine of the angle between them, often used to compare documents in text mining. Given two vectors of attributes, R and T, the cosine similarity, θ , is represented using a dot product and magnitude as:

$$Similarity = \cos(\theta) = \frac{R.T}{|R|.|T|} = \frac{\sum_{i=1}^n r_i.t_i}{\sqrt{\sum_{i=1}^n r_i^2} * \sqrt{\sum_{i=1}^n t_i^2}}$$

The resulting similarity ranges from -1 meaning exactly opposite, to 1 meaning exactly the same, with 0 usually indicating independence, and in-between values indicating intermediate similarity or dissimilarity.

IV. SYSTEM ARCHITECTURE

Figure 1 shows the process of the CRF-based authorship identification. The implementation carries out in the following steps.

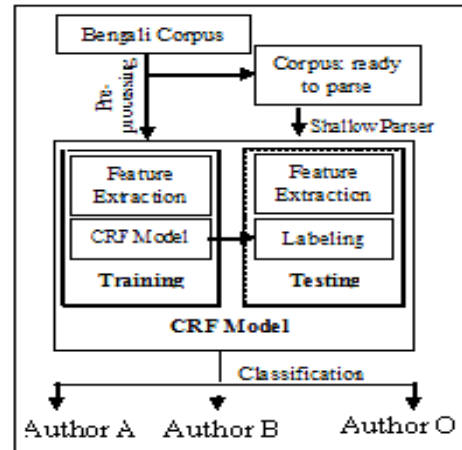


Figure 1. Proposed system architecture

A. Pre-processing and Parsing:

The documents are raw and so unformatted that an initial cleaning is required before CRF model training. We must transfer the document into the formatted sequences, i.e. a bag of words or phrases of the document. From the pre-processed document, token-level and some of the context-level features are extracted. For a new document, we conduct the sentence segment, POS tagging using Shallow Parser¹ so that the stylistic features are easily viewed to the system. From this, chunk-level and context-level markers are identified.

B. CRF Model:

The input is the feature vector discussed in Table I. There are three kinds of features, i.e. (1) token-level features, (2) phrase-level features and (3) context-level features. Token-level features include length of the word, number of keywords, starting word of a dialog maximum time present, count of hapax legomena. Phrase-level include count of POSs, chunks those we have considered here (not all POSs or chunks, the Shallow parser generally gives, are considered). Average length of the paragraph and length of the dialog are included in context-level features. Detected sentences are the sentence boundary ended mainly with 'dari' ('ৱ'), question marks ('?') or exclamation notation ('!') in Bengali. Sentence-length, word-count are the traditional and well-defined measures

¹ <http://ltrc.iiit.ac.in/analyzer/bengali>

in authorship attribute studies and punctuation count is the very interesting characteristics of the personal style of a writer. Problem occurs to identify keywords as there is no standard tool to extract keywords for Bengali documents. For this, we have identified top ten high frequent words (excluding stop-words in Bengali) for every cluster using TF*IDF method which act as the list of keywords of that cluster corresponding to that author. Now, similarly, we have extracted a list of top ten high frequent words from every testing document and intersect them with the keywords of cluster1, cluster 2 and cluster 3 which are the count of the features KW1, KW2, KW3 respectively. Since Shallow parser is an automated text-processing tool, the style markers of the above levels are measured approximately. Depending on the complexity of the text, the provided measures may vary from real values which can only be measured using manual intervention. Making the system fully automated, the system fully believes on the performance of the parser for the extraction of all POS and chunk level features. The last column of the training feature file is labeled as R, A or O which is the indication of the three authors and for testing, all are labeled as X which is an arbitrary word indicating unknown author. CRF adds an extra column at the last position which indicates the label of the author for that document (R, A or O).

TABLE I. FEATURES IN THE CRF MODEL

No.	Features	Explanations	Normalization
1	Doc	Name of the document	-
2	Len_w	Average length of the word	Avg. len (word)/ Max len of word
3	Len_d	Average length of the dialog	Avg. words per dialog / no. of sentences
4	Len_p	Average length of the paragraph	Avg. sentences per paragraph / no. of sentences
5	Punc	No. of punctuations	count (punc.) / no. of word
6	Chunk_N	Detected Noun phrase	count (NP) / no. of all chunk count
7	Chunk_V	Detected Verb phrase	count (VP) / no. of all chunk count
8	Chunk_CCP	Detected conjunct phases	count (CCP) / no. of all chunk count
9	POS_U	Detected unknown word	count (unknown)/ count (word)
10	POS_RE	Detected reduplication and echo-word	count (RDP+ECH) / count (word)
11	KW1	Intersection of the keywords of cluster 1 and the tested document	$ KW(doc) \cap KW$ (cluster 1) / no. of KW in cluster 1
12	KW2	Intersection of the keywords of cluster 2 and the tested document	$ KW(doc) \cap KW$ (cluster 2) / no. of KW in cluster 2
13	KW3	Intersection of the keywords of cluster 3 and the tested document	$ KW(doc) \cap KW$ (cluster 3) / no. of KW in cluster 3
14	Start	Starting word (stemming form) of the dialog which is present in maximum time	-
15	Hapax Legomena	No. of words with frequency = 1, including named-entities	count (Hapax legomena)/count (word)

As we can see that maximum of these features are the ratio of two relevant measures, this approach was followed in order to achieve as text-length independent style markers as possible. However, it is worth noting that we do not claim that the proposed set of features is the final one. It could be possible to split them into more fine-grained measures. Here, our goal is to make a pioneer approach towards the investigation of Bengali author's writing style and to prove that an appropriately defined set of such style markers performs better than the traditional lexically-based approaches.

V. EXPERIMENTAL DETAILS

A. Used Corpus

Resource acquisition is one of the most challenging obstacles to work with electronically resource constrained languages like Bengali. However, this system has used thirty stories in Bengali written by the noted Indian Nobel laureate Rabindranath Tagore². Among them, we have selected twenty stories for training purpose and rest for testing. We choose this domain for two reasons: firstly, in such writings the idiosyncratic style of the author is not likely to be overshadowed by the characteristics of the corresponding text-genre; secondly, in the previous research [10], the author has worked on the corpus of Rabindranath Tagore to explore some of the stylistic behaviors of his documents. To differentiate them from other author's articles, we have selected 30 articles from author A and 30 articles from a group of other authors³ not included previously and divided them into same fashion as training and testing purpose as previous. In this way, we have three clustered documents called as articles of Author R (Tagore's articles, cluster 1), Author A (cluster 2) and others (Author O, cluster 3). This paper focuses on two topics: (a) the effort of many authors on feature selection and learning and (b) the effort of limited data in authorship detection.

B. Baseline System

In order to set up a baseline system, we proposed traditional lexically-based methodology called *vocabulary richness*. Among the various measures like Yule's K measure, Honore's R measure, we have taken most typical one as the type-token ratio (V/N) where V is the size of the vocabulary of the sample text and N is the number of tokens which forms the simple text. We have gathered dimensional features of the articles of each cluster and averaged them to make a mean vector for every cluster. So these three mean vectors indicate the references of three clusters respectively.

TABLE II. CONFUSION MATRIX OF BASELINE SYSTEM

Baseline System				
	R	A	O	e (Error)
R	6	0	4	0.40
A	7	2	1	0.80
O	5	2	3	0.70
Average error				0.63

² <http://www.rabindra-rachanabali.nltr.org>

³ <http://banglalibrary.evergreenbangla.com/>

Now, for every testing document, similar features have been extracted and a test vectors have been prepared. By using nearest-neighbor algorithm, we have tried to identify the author of the testing documents. The results of the baseline system are shown using confusion matrix in Table II. Each row contains classification of the ten texts of the corresponding authors. The diagonal contains the correct classification. The baseline system achieves 37% average accuracy. Approximately 60% of average accuracy error (for author A and O) is due to the wrong identification of the author as Author R.

C. Performance of Statistical Model

As aforementioned, we are dealing with two ways of classification model in Natural Language Processing i.e. statistical and machine learning approaches to make a comparative study among them to show which is more accurately performed in Stylometry detection task. Same features are used in this methodology and they act as the dimensions of the vector. After grouping the documents into three clusters, we have made a reference vector (mean vector) individually for every cluster which performs as the representatives for that cluster. For every test document, the cosine-similarity measures are performed with the three reference vectors and the document is assigned to that cluster with which, the similarity is higher. The first half of the confusion matrix named as “Cosine-similarity” in Table III depicts the results of this measure. As we can notice from the table that the accuracy of the statistical measure is 54% which is far better than the traditional baseline system and the articles of Rabindranath Tagore are identified more perfectly than others. It may be because of the resource acquisition of the corpus of Rabindranath Tagore is homogeneous in nature, where as for other authors, it has not been possible to collect same length corpus and sometime the collected corpus are of different domains.

TABLE III. CONFUSION MATRIX FOR BOTH MEASURES

Cosine-similarity					CRF			
	R	A	O	e	R	A	O	e
R	6	2	2	0.4	7	1	2	0.3
A	2	5	3	0.5	3	5	2	0.5
O	4	2	5	0.5	3	1	6	0.4
Average error				0.46	Average error			0.40

D. Performance of CRF based Modal

Performance of the CRF model for authorship identification is shown in the second half of the Table III named as “CRF”. The average accuracy of this system is 60% which shows a tremendous improvement in comparison with the baseline system. The identification of the documents of author A is more or less same with the previous statistical approach and 30% of the error for Author A and Author O have been occurred for wrong identification of the author as Author R. This shows a little biasness of the system to the Stylometry of Tagore’s writing.

VI. CONCLUSION

Conditional Random Field is a state-of-the-art sequence modeling approach, which can use the features of the documents more sufficiently and effectively. In this paper, we have studied in Bengali corpus to detect the stylistic features of the anonymous writings and try to map them with their possible authors. The presented methodology can also be used in author verification task i.e. the verification of the hypothesis whether or not a given person is the author of the text under study even if in other languages since maximum of the features are language independent. Particularly, it seems from our experiments that texts with less word are less likely to be correctly classified. However, for our future study, we would like to apply this system for other languages. Furthermore, we plan for a hybrid approach that can takes into account the advantage of both the unsupervised as well as machine learning approaches and look for the improvement of the performance. For this, more textual analysis and relevant corpus collection will be needed. Above all, we would implement this system on the other fields of Text mining i.e. e-mail identification, forensic investigation, copyright and estate disputes etc. to make it more robust and general.

REFERENCES

- [1] D. Holmes, “Authorship Attribution,” *Computers and the Humanities*, 28 (1994), pp. 87–106.
- [2] D.J. Croft, *Book of Mormon word prints reexamined*. Sun Stone Publish., 6:15-22, 1981, Available: <http://lds-mormon.com/wordpri.shtml>.
- [3] D. Pavelec, E. Justino and L. S. Oliveira, “Author Identification using Stylometric features,” *Inteligencia Artificial, Revista Iberoamericana de Inteligencia Artificial*. Valencia, Espana, Vol 11, pp. 59-65, 2007.
- [4] E. Stamatatos, N. Fakotakis and G. Kokkinakis, “Automatic authorship attribution,” in *proc. of the 9th Conference on European Chapter of the ACL*, June 8-12, 1999, p. 158.
- [5] K. H. Krippendorf, “Content Analysis-An Introduction to its Methodology,” 2nd Edition, *Sage Publications Inc.*, ISBN: 13: 978- 0761915454, p. 440, 2003.
- [6] M. B. Malyutov, Authorship attribution of texts: A review. Lecture Notes in Computer Science, 2006, Volume 4123/2006, pp. 362-380, DOI: 10.1007/11889342_20.
- [7] S. Argamon, M. Saric and S.S. Stien, “Style mining of electronic messages for multiple authorship iscrimination: First results,” in *Proc. 9th ACM SIGKDD*, 2003, p. 475.
- [8] T. K. Mustafa, N. Mustapha, M. A. Azmi and N. B. Sulaiman, “Dropping down the Maximum Item Set: Improving the Stylometric Authorship Attribution Algorithm in the Text Mining for Authorship Investigation,” *Journal of Computer Science* 6 (3), pp. 235-243, 2010.
- [9] T. Zhang, F. Damerou and D. Johnson, “Text chunking using regularized winnow,” in *proc. 39th Annual Meeting on ACL*, July 6-11, 2002, pp. 539-546.
- [10] T.Chakraborty and S. Bandyopadhyay, “Identification of Reduplication in Bengali Corpus and their semantic Analysis: A Rule Based Approach,” In *proc. of the COLING (MWE 2010)*, Beijing, pp. 72-75.
- [11] T. Mendenhall, “The characteristic curve of composition,” *Science*, 214:237-249, 1887.
- [12] C. Zhang, H. Wang, Y. Liu, D. Wu, Y. Liao and B. Wang, “Automatic Keyword Extraction from Documents Using Conditional Random Fields,” *Journal of Computational Information Systems* 4:3(2008):1169-1180.

Analysis of Data Retrieval Time for Filter-based Data Fusion Management Scheme

Boudhayan Bhattacharya
Assistant Professor
Dept. of Computer Application
Brainware Group of Institutions
Kolkata, India
mail4boudhayan@rediffmail.com

Sharmistha Bhattacharjee
Scientist "C"
Education & Training
DOEACC Society
Kolkata, India
sharmi9870@yahoo.com

Dwijesh Dutta Majumder
Professor Emeritus, ISI
Emeritus Scientist, CSIR
Secretary & Director, ICSIT
Kolkata, India
ddm@isical.ac.in

Abstract- Data Fusion comprises of information coming from multiple sources to facilitate better assessment. This article presents a comparison of Retrieval time of other existing data fusion architectures - Centralised, Cascaded, Federated, and Distributed with our Multi-level Federated architecture's to improve the filtration of each signaling sensor for a reference sensor (RS) within its fusion domain which shows improvement with respect to the existing architectures. It is done by sending the individual sensor data through multiple levels of local filters (LF) each time sensor carries the data for fusion. This process not only reduces the load from Master Fusion Filter (MFF) but also lessens both Rate of Data Loss and Data Retrieval time.

Keywords: Master Fusion Filter, Reference Sensor, Local Filter, Centralised, Cascaded, Federated, Distributed and Multi-level Federated.

I. INTRODUCTION

Data fusion had gone through considerable and rapid change in the last few years. Fusion has become an important feature of data processing in several different fields. Based on the architectures of the local filters and master fusion filter, the information that needs to be fused can vary greatly.

On the other hand, the research work published so far does not provide any systematic study of the inertial network architecture, especially in terms of data fusion methods, dynamic alignment and correction of distributed inertial sensor systems, and distributed sensor failure detection and isolation techniques with respect to the levels of local filters to ease out the load on master fusion filter. Therefore, we propose a new data retrieval time formulation of our Multi-level Federated Local filter architecture [1] for structural and analytical investigation of data fusion methodologies in the design, development and simulation of fault-tolerant navigation system based on data fusion network architectures.

II. RELATED WORK

From 1996 to 1999 [2], European workgroup FUSION worked on fusion in several fields of it. The discussions within the GDR-PRCISIS [3] workgroup on information fusion, surrounding on the diversity of fusion problems encountered in signal and image processing encouraged the FUSION group to device the architectural specifications.

Data fusion is a tactic which combines the data from different sensors sources to cooperate each other to take the total effect in higher level than the independent sum of effects. The MultiSensor Data Fusion (MSDF) was first coined for military applications including battlefield surveillance, automatic multi-target tracking and recognition [4][5] and then are applied to civil industries [6][7][8] including guidance and control of autonomous vehicles and robotic systems. MSDF is also applied to estimation and identification theory, control engineering, statistics and decision theory, signal processing and pattern recognition, artificial intelligence and knowledge engineering. So the multidisciplinary nature of MSDF can be applied to wide range of applications.

Since the 1970s, the Kalman filter was developed for diverse applications in aircraft navigation, control and guidance. After that, various filter architectures and filtering algorithms based on Kalman were proposed for different data fusion methods to fuse multiple navigation sensor data to achieve the desired performance. The filter architectures can be classified as: Centralised, Cascaded, Federated, Distributed and Multi-level Federated Local filter architecture.

Centralised Filter Architecture:

In Centralised Filter architecture (Fig 1) the data from every navigation sensors are quantified which are further developed in a central data fusion filter to obtain the precise estimates of the navigation states. [9][10][11]

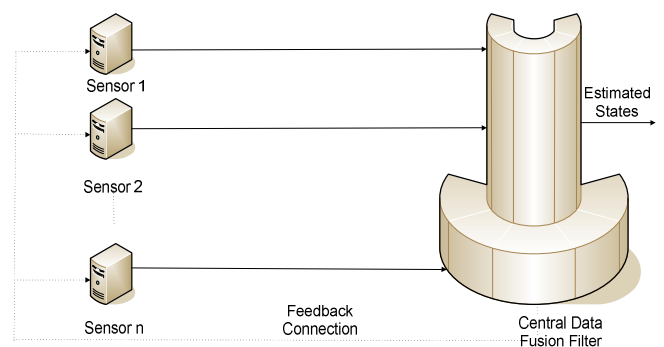


Figure 1: Centralised Filter Architecture

Cascaded Filter Architecture:

In Cascaded Filter architecture (Fig 2), the output of one filter is used as input to a succeeding filter. The estimates of the system states and their error covariance comprise the filter outputs. [12][13][14][15]

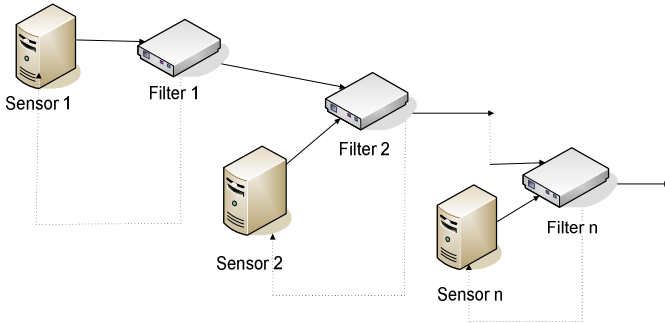


Figure 2: Cascaded Filter Architecture

Federated Filter Architecture:

The Federated Filter architecture (Fig 3) is a two-stage filtering architecture. Individual sensor systems from all parallel local filters combine with a common reference system. This is done for data propagation and evaluation of the local system states. [16][17]

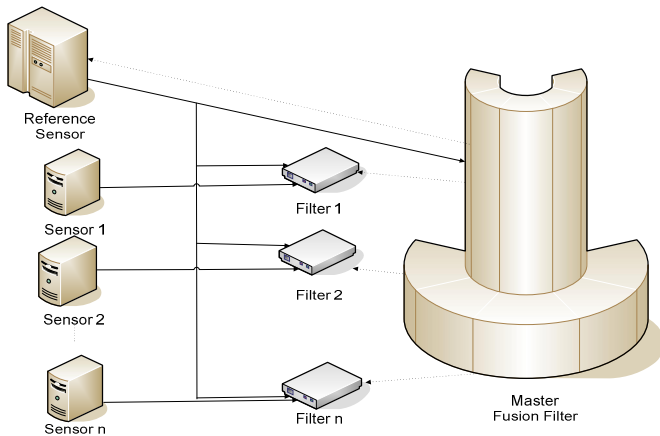


Figure 3: Federated Filter Architecture

Distributed Filter Architecture:

The Distributed Filter architecture (Fig 4) is not developed on any standard model. Considering the viewpoint of information use, there are two main data fusion approach to the design of distributed filters - Measurement Fusion and State Fusion. [18][19]

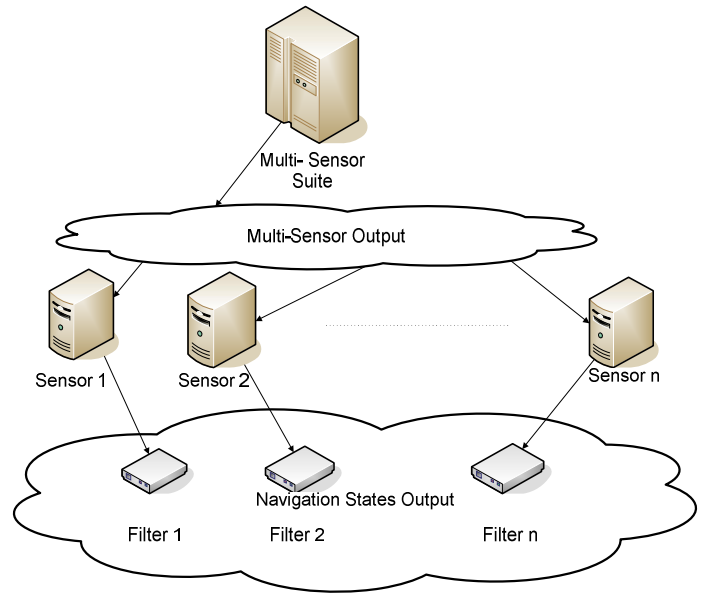


Figure 4: Distributed Filter Architecture

III. PERFORMANCE ANALYSIS OF EXISTING ARCHITECTURES

Over the past decades, several data fusion architectures have been developed and the majority of them are based on the parity vector/space techniques. [20] Another popular one is the test matrix method and parity equations comparison method. [21] These techniques are used to detect and segregate failures of redundant inertial sensor systems in a fused data configuration. The comparison tests a set of 15 parity equations each containing output values of four sensors while the test matrix method uses a 15X6 - dimensional matrix where row consists of coefficients of one parity equation and performs a test on a different subset of four sensors. [22]

These methods compute and compare each parity equation and employ a least-squares estimator for the estimation of the measured states. So it is a time-expensive process for a large number of redundant sensors.

IV. MULTI-LEVEL FEDERATED LOCAL FILTER ARCHITECTURE

Having adjacent and different levels, our Multi-level Federated Local filter scheme (Fig 5) can alleviate out the load from MFF. Additionally, it has a straight communication with the reference filter to compare the fused data.

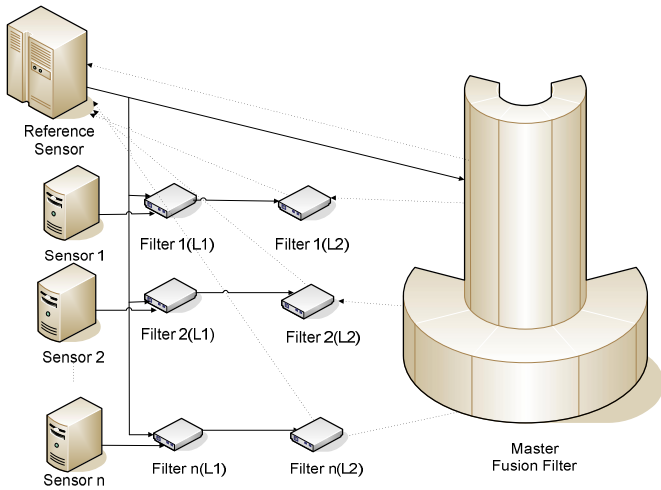


Figure 5: Proposed Architecture

We deduce the mathematical model of the architecture to calculate data retrieval time for the data fusion using the Dynamic Transformation Model. Dynamic Transformation Model analyzes traffic flow depending on environmental random movement for carrying out data fusion. The model calculates the data retrieval time from the number of stages of the local filter and its domain boundary.

Let N be the total no. of LF.

P_n = Perimeter of each LF.

P_m = Perimeter of MFF.

S = Scale factor stability

A = Alignment

N_R = Random noise

H = Bias uncertainty

$$P_n = N \sqrt{(P_m/N)^2}$$

R_n = Crossing rate of different LF levels

ρ = Data fusion density per LF

v = Average velocity of the light

$$R_n = (\rho v P_n / \pi)$$

F = Flattening of the LF surface

$$\text{So } R_n = (\rho v P_n / \pi) / F$$

Adding scaling factor we get,

$$R_n = 5 (\rho v P_n / \pi) / F$$

If we consider random noise the formulation will be

$$R_n = 5 (\rho v P_n / \pi) / F + N * N_R$$

Adding the alignment consideration, we get

$$R_n = 1/A [5 (\rho v P_n / \pi) / F + N * N_R]$$

Taking the bias uncertainty into count we have

$$R_n = 1/A [5 (H * \rho v P_n / \pi) / F + N * N_R]$$

L_t = Latency time for each level of filter

So the general n -level LF data retrieval time for the single MFF domain will be

$$DRT = \sum_{i=1}^n \frac{1}{A} [5 (H * \rho v P_n / \pi) / F + N * N_R] + n L_t$$

V. PERFORMANCE ANALYSIS

Data retrieval is one of the difficult steps in data fusion filtering. It consists of identifying and correlating noisy measurements, the genesis of which are unidentified because of several inescapable situations. The key models used in this fields are either deterministic (based on Classical Hypothesis), or probabilistic models (based on Bayesian Hypothesis).

The values taken here as the standard parameters are from the literature [23]. We found that our formulation yields better result than that of Centralised, Cascaded, Federated and Distributed Filter architectures.

Parameters	Value
Bias uncertainty (o/h)	10-40
Scale factor stability (ppm)	100-500
Alignment (arcs)	200
Random noise (o/h/ \sqrt{Hz})	1-5
Flattening (f)	1/298.257223563
Latency time (ms)	10

Considering the number of LF levels as 1, our formulation for data retrieval time yields 511, 459, 436, 441 and 389 ms for Centralised, Cascaded, Federated, Distributed and for the Multi-level Federated filter architectures respectively.

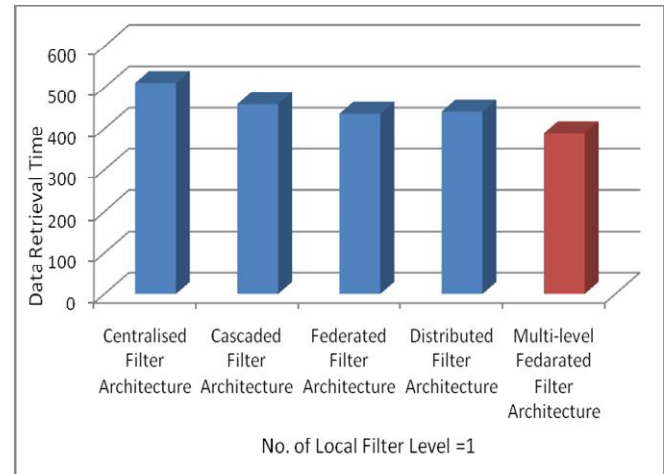


Figure 5: Comparison of Data Retrieval Time (No. of Filter Level =1)

Considering the number of LF levels as 2, our formulation for data retrieval time yields 657, 581, 558, 573 and 447 ms respectively for Centralised, Cascaded, Federated, Distributed and for the Multi-level Federated filter architectures.

Considering the number of LF levels as 3, our formulation for data retrieval time yields 748, 675, 641, 657 and 499 ms respectively for Centralised, Cascaded, Federated, Distributed and for the Multi-level Federated filter architectures.

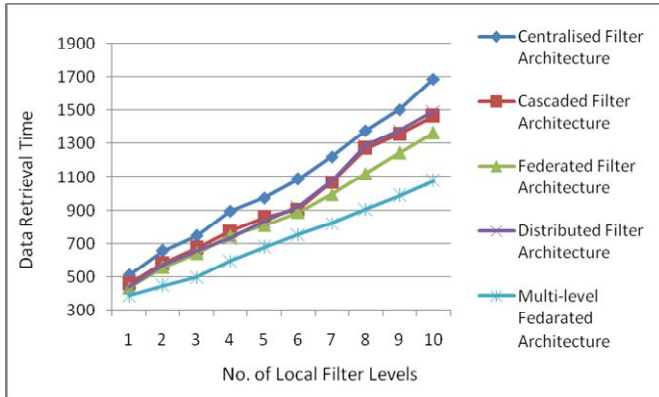


Figure 6: Comparison of Data Retrieval Time

VI. CONCLUSION

Merits and demerits are part of any architecture. This paper analyses the most noteworthy schemes with respect to Data Retrieval Time. Different schemes have different problems which can be addressed to upgrade the data fusion methodology as per analysis. We tried to reduce the Data Retrieval Time for our Multi-level Federated scheme [23] for improving the performance of Data Fusion in information processing.

REFERENCES

[1] Boudhayan Bhattacharya, Sharmistha Bhattacharjee and Dwijesh Dutta Majumder “Analysis of Filter Architectures Based on Different Data Fusion Management Scheme” Sent in INDICON 2010

[2] Bloch I., Maître H., “Fusion de données en traitement d’images: modèles d’information et décisions”, *Traitement du Signal*, vol. 11, no. 6, p. 435-446, 1994.

[3] Bar-Shalom Y, Fortmann T.E., *Tracking and Data Association*, Academic Press, San Diego, California, 1988.

[4] Blackman, S.S., *Multiple Targets Tracking with Radar Applications*. Artech House Inc. 1986

[5] Hall, D. L. and Llinas, J., *An Introduction to Multisensor Data Fusion*, *Proceedings of the IEEE* Vol. 85, No. 1, Jan. 1997, 6 -23

[6] <http://www.data-fusion.org/article.php>

[7] Luo, R. C. and Kay, M. G., *Multisensor Integration and Fusion in Intelligent System*, *IEEE Trans. On System, Man, and Cybernetics*, Vol. 19, No. 5, Sept/Oct 1989, 901-931.

[8] Kokar, M. and Kim, K., *Review of Multisensor Data Fusion: Architecture and Techniques*, *Proceedings of The International Symposium on Intelligent Control*, Chicago, Illinois, USA, Aug. 1993, 261-266

[9] Diesel, J. W., *Integration of GPS/INS for Maximum Velocity Accuracy*, *Journal of The Institute of Navigation*, Vol. 34, No. 3, Fall 1987.

[10] Diesel, J.W. *GPS/INS Integration for Civil Aviation*, *Proceedings of National Telesystems Conference*, 1991, 223 -228

[11] Hyslop, G.; Gerth, D.; Kraemer, J. *GPS/INS integration on the Standoff Land Attack Missile (SLAM)*, *IEEE Aerospace and Electronics Systems Magazine*, Vol. 5, No. 7, July 1990, 29 –34.

[12] Schlee, F.H.; Toda, N.F.; Islam, M.A. and Standish, C.J., *Use of an external cascade Kalman filter to improve the performance of a Global Positioning System (GPS) inertial navigator*, *Proceedings of the IEEE NAECON 1988*, 345-350.

[13] Wade, M. and Grewal, M. S., *Analysis of A Cascaded INS Calibration Filter*, *Proceedings of the IEEE 1988*, 366-373.

[14] Karatsinides, S. E., *Enhancing Filter Robustness in Cascaded GPS-INS Integrations*, *IEEE Trans. On Aerospace and Electronic Systems*, Vol. 30, No. 4, Oct., 1994, 1001-1008.

[15] Bell, W.B; Gorre, R.G; and Cockrell, L.D, *Cascading Filtered DTS Data into a Loosely Coupled GPS/INS System*, *Proceedings of IEEE PLANS’98*, 1998, 586-593.

[16] Carlson, N.A., *Federated Filter for Fault-Tolerant Integrated Systems*, *Proceedings of 1988 IEEE PLANS*, 1988, 110-119.

[17] Felter, S.C., *An overview of decentralized Kalman filter techniques*, *Proceedings of IEEE Southern Tier Technical Conference*, 1990, 79-87.

[18] Bar-Shalom, Y. and Fortmann, T. E., *Tracking and Data Association*, Academic Press, New York, 1988.

[19] Liggins, M. E., II; Chee-Yee Chong; Kadar, I.; Alford, M. G.; Vannicola, V. and Thomopoulos, S., *Distributed Fusion Architectures and Algorithms for Target Tracking*, *Proceedings of the IEEE*, Vol. 85, No. 1, Jan. 1997, 95-107.

[20] Evans, F.A. and Wilcox, J. C., *Experimental Strapdown Redundant Sensor Inertial Navigation System*, *Journal of Spacecraft and Rockets*, Vol. 7, No. 9, Sept., 1970, 1070-1074.

[21] Gilmore, J. P. and Mckern, R. A., *A Redundant Strapdown Inertial Reference Unit (SIRU)*, *Journal of Spacecraft and Rockets*, Vol. 9, No. 1, Jan., 1972, 39-47.

[22] Potter, J.E. and Deckert, J.C., *Minimax Failure Detection and Identification in Redundant Gyro and Accelerometer System*, *Journal of Spacecraft*, Vol. 10, No. 4, April, 1973, 236-243.

[23] Spitzer, C.R, *The Avionics Handbook*, CRC Press LLC, 2001

Unified Drain Current Model for Independently Driven Double Gate MOSFETs

Binit Syamal, C. K. Sarkar
Department of Electronics &
Telecommunication Engineering,
Jadavpur University
Kolkata-700032, India
Email: binit.syamal@yahoo.com

Pradipta Dutta
School of Technology
Department of Electronics &
Telecommunication Engineering,
KIIT University, Bhubaneswar
Orissa-751024, India
Email: cr_dutta@yahoo.co.in

N. Mohankumar
SKP Engineering College,
Thiruvannamalai-60661
Tamil Nadu, India
Email: nmkphdju@gmail.com

Abstract—A generic surface potential based current voltage (I-V) model for heavily doped asymmetric Double Gate MOSFET is presented. The model is derived from the 1-D Poisson equation with all the charge terms included and the channel potential is solved for the asymmetric operation of DG MOSFET based on the Newton Raphson Iterative method. A non charge sheet based drain current model based on the Pao-Sah's double integral method is formulated in terms of front and back gate surface potentials at the source and drain end. The model is able to clearly show the dependence of the front and back surface potentials and the drain current on the terminal voltages, gate oxide thicknesses, channel doping concentrations and the Silicon body thickness and a good agreement is observed with the 2-D numerical simulation results.

Index Terms—Asymmetric double gate MOSFET, Pao-Sah's double integral, Poisson's equation, Short Channel Effects

I. INTRODUCTION

As the microelectronics industry enters the 100 nm regime, the multi-gate MOSFETs are surely to substitute the bulk CMOS technology. The double gate MOSFETs with increased

electrostatic coupling between the gates provide a better scalability option due to its excellent immunity to short-channel effects, near 60mV/dec subthreshold slope, low Drain-Induced-Barrier-Lowering (DIBL) and the possibility of using lightly doped or undoped body [1]. The DG devices can be implemented with tied gates or independently controlled gate architectures [2]. In the independently driven DG MOSFET (ID-DG), the back-gate can control the effective threshold voltage and the front channel current via gate-to-gate coupling. Tied-gate circuit topology provides higher current density and drive capability in addition to a compact layout area. On the other hand, the independently driven DG MOSFETs results in reduced transistor count and improved performance for logic as well as analog applications.

A carrier based drain-current model for generic four-terminal DG MOSFETs valid for all symmetric, asymmetric, and independent-gate operation modes has been reported in [3] with consideration of only the inversion charges. The main advantage of multi-gate MOS devices is the possibility to use lightly doped body with threshold voltage tuning controlled by the metal gate work-function. Still it is not possible to implement metals of any work-function to get a desired threshold voltage and so one still has to rely on channel doping concentration for this purpose. In this paper, we report a surface potential based compact analytical model for long channel asymmetric DG MOSFETs with lightly/heavily doped Silicon channel. The short channel effects and the quantum mechanical effects have not been included for simplicity.

This work was supported by the Department of Science & Technology, Govt. of India under SERC scheme for its financial assistance in carrying out research activities.

B. Syamal & C. K. Sarkar are with the Nano Device Simulation Laboratory, Department of Electronics & Telecommunication Engineering, Jadavpur University, Kolkata-700032, India (phone: 00 91 9051689900; e-mail: binit.syamal@yahoo.com).

P. Dutta is with the School of Technology, Department of Electronics & Telecommunication Engineering, KIIT University, Orissa-751024, India (e-mail: cr_dutta@yahoo.co.in).

N. Mohankumar is with the Electrical Engineering Department, SKP Engineering College, Thiruvannamalai-60661, Tamil Nadu, India (e-mail: nmkphdju@gmail.com).

II. SURFACE POTENTIAL SOLUTION

The cross section of the asymmetric MOSFET is shown in Fig. 1 where x ($0 \leq x \leq t_{Si}$) & y ($0 \leq y \leq L$) denotes the coordinates along the thickness of the Silicon film and the length of the channel respectively. Based on the gradual channel approximation (GCA), the channel potential along the x direction can be obtained by solving the 1-D Poisson–Boltzmann equation with the depletion charge, inversion charge and the hole charge as shown in (1)

$$\frac{d^2\phi}{dx^2} = \frac{qN_a}{\epsilon_{Si}} \left[1 + e^{\frac{\phi - (2\phi_F + V)}{V_T}} - e^{-\frac{\phi}{V_T}} \right] \quad (1)$$

where N_a denotes the channel doping concentration, ϵ_{Si} is the Silicon permittivity, V_T is the thermal voltage and V is the channel voltage that varies from 0 at the source end to V_{ds} at the drain end. The boundary conditions at the front and back surface of the DG MOSFET can be obtained by applying the Gauss Law as

$$\epsilon_{Si} \frac{d\phi}{dx} \Big|_{x=0} = -\epsilon_{Si} E_{sf} = \epsilon_{ox} \frac{\phi_{sf} - (V_{gf} - V_{ffb})}{t_{oxf}} \quad (2a)$$

$$\epsilon_{Si} \frac{d\phi}{dx} \Big|_{x=t_{Si}} = -\epsilon_{Si} E_{sb} = \epsilon_{ox} \frac{(V_{gb} - V_{bfb}) - \phi_{bf}}{t_{oxb}} \quad (2b)$$

where ϕ_{sf} (ϕ_{bf}), V_{gf} (V_{gb}) and V_{ffb} (V_{bfb}) are the surface potential, gate voltage and flat band voltage at the front (back) gate respectively. As reported in [4], a normalized variable x' was defined to obtain an analytical expression of the surface potential in symmetric DG MOSFET with all the charge terms included in the Poisson's equation. To obtain a compact relation between the front surface potential ϕ_{sf} and the back surface potential ϕ_{bf} in case of the asymmetric architecture, we define three normalized variables l , m and n such that

$$x \cos \alpha = l, \quad x \cos \beta = m \quad \text{and} \quad x \cos \gamma = n \quad (3)$$

Using the relation $\frac{d^2\phi}{dx^2} = \cos \alpha \frac{d}{dl} \left(\frac{d\phi}{dx} \right)$ in (1) and integrating from m to 1, we get

$$-\left(\frac{d\phi}{dx} \right) = \frac{qN_a t_{Si}}{\epsilon_{Si}} \left[\begin{array}{l} (1-m) + \int_m^1 e^{\frac{\phi - (2\phi_F + V)}{V_T}} dl \\ - \int_m^1 e^{-\frac{\phi}{V_T}} dl \end{array} \right] + E_{sb} \quad (4)$$

Applying the relation $\left(\frac{d\phi}{dx} \right) = \left(\frac{d\phi}{dm} \right) \left(\frac{dm}{dx} \right) = \left(\frac{d\phi}{dm} \right) \cos \beta$ in (4)

and integrating from n to 1, we obtain the relation

$$-(\phi(n)) \Big|_{n=1} - \phi(n) \Big|_{n=n} = \frac{qN_a t_{Si}^2}{\epsilon_{Si}} \left[\begin{array}{l} \left(\frac{(1-n)^2}{2} \right) + \int_n^1 \int_n^1 e^{\frac{\phi - (2\phi_F + V)}{V_T}} dl dm \\ - \int_n^1 \int_n^1 e^{-\frac{\phi}{V_T}} dl dm \end{array} \right] + t_{Si} E_{sb} (1-n) \quad (5)$$

Applying 2(a) and 2(b) in (5), one can obtain an explicit model of electrostatic potential along the channel thickness in terms of the back surface potential as

$$\phi - \phi_{sb} = \frac{qN_a t_{Si}^2}{2\epsilon_{Si}} \left[\begin{array}{l} (1-n)^2 + f(n) e^{\frac{(\phi_{sb} - 2\phi_F - V)}{V_T}} \\ - g(n) e^{-\frac{\phi_{sb}}{V_T}} \end{array} \right] + E_{sb} t_{Si} (1-n) \quad (6)$$

where $f(n) = 2 \int_n^1 \int_n^1 e^{\frac{\phi - \phi_{sb}}{V_T}} dl dm$, $g(n) = 2 \int_n^1 \int_n^1 e^{-\frac{\phi - \phi_{sb}}{V_T}} dl dm$

Surface potential values from (6) cannot be solved by simple mathematical approaches. One can express (6) in the form of $\phi = f(\phi)$ so that its root can be calculated by

$\phi_{n+1} = f(\phi_n)$ with a fixed starting point ϕ_0 . Before evaluation of the potential variation, one need to find the values of the two functions $f(n)$ and $g(n)$. In this paper,

the initial point ϕ_0 is taken as ϕ_{sb} . After some complex mathematical steps, $f(n)$ and $g(n)$ can be expressed as

$$f(n) = \frac{1 - e^{-(k_1^2 - k_2^2)} + k_1 \sqrt{\pi} e^{-k_2^2} [\operatorname{erfi}(k_1) - \operatorname{erfi}(k_2)]}{a} \quad (7)$$

$$g(n) = \frac{-1 + e^{-(k_1^2 - k_2^2)} + k_1 \sqrt{\pi} e^{k_2^2} [\operatorname{erf}(k_1) - \operatorname{erf}(k_2)]}{a} \quad (8)$$

where $k_1 = \sqrt{a(1-l)} + \left(\frac{b}{2\sqrt{a}} \right)$ and $k_2 = \left(\frac{b}{2\sqrt{a}} \right)$,

$$a = \frac{qN_a t_{Si}^2}{2\epsilon_{Si} V_T} \left[1 + e^{\frac{(\phi_{sb} - 2\phi_F - V)}{V_T}} - e^{-\frac{(\phi_{sb})}{V_T}} \right] \quad \text{and} \quad b = \frac{E_{sb} t_{Si}}{V_T}$$

Here $\operatorname{erf}(k)$ and $\operatorname{erfi}(k)$ are the well-known error function and imaginary error function, respectively. At the front surface, $\phi = \phi_{sf}$ so that the front and back surface potential in an asymmetric DG MOSFET can be expressed as a function $F(\phi_{sf}, \phi_{sb}) = 0$ where

$$F(\phi_{sf}, \phi_{sb}) = (\phi_{sf} - \phi_{sb}) - \frac{qN_a t_{Si}^2}{2\epsilon_{Si}} \left[1 + f(0) e^{\frac{(\phi_{sb} - 2\phi_F - V)}{V_T}} \right] - E_{sb} t_{Si} \quad (9)$$

Applying the boundary conditions of (2), the Poisson equation in (1) can be integrated from the front surface within the channel to the back gate surface to obtain

$$E_{sf}^2 = \frac{(2qN_a)}{\epsilon_{Si}} [(\phi_{sf} - \phi_{sb}) + V_T e^{((-2\phi_F - V)/V_T)} (e^{\phi_{sf}/V_T} - e^{\phi_{sb}/V_T}) + V_T (e^{-\phi_{sf}/V_T} - e^{-\phi_{sb}/V_T})] + E_{sb}^2 \quad (10)$$

Equation (9) and (10) can be iteratively solved by Newton Raphson (NR) method to obtain ϕ_{sf} and ϕ_{sb} for a given values of V_{gf} and V_{gb} . The error tolerance is set at $|F(\phi_{sf}, \phi_{sb})| \leq 10^{-10} V$ which should vanish for an exact solution. The loop continues until ϕ_{sf} and ϕ_{sb} converges. The practical test shows that it requires six iterations when ϕ_{sf} and ϕ_{sb} changes their values from 0.2415V and 0.2122V to 0.3708V and 0.2828V respectively when V_{gf} changes from 0.3V to 0.5 V keeping $N_a = 10^{18} \text{ cm}^{-3}$, $t_{Si} = 5 \text{ nm}$, $t_{oxf} = t_{oxb} = 2 \text{ nm}$ and $V_{gb} = 0.2 V$

III. FORMULATION OF DRAIN CURRENT MODEL

A Non charge sheet based drain current model based on Pao-Sah's Double Integral under the assumption of GCA and constant mobility for long channel DG MOSFETs is given by [5] as

$$I_{ds} = \mu \frac{W}{L} \int_0^{\phi_{sf}} \int_{\phi_{sb}}^{\phi_{sf}} \frac{qn}{E} d\phi dV \quad (11)$$

where $n = N_a e^{(\phi - 2\phi_F - V)/V_T}$. The integration can be easily solved by incorporating a new variable $\alpha(V)$ as shown in [4]

$$\alpha(V) = E_{sf}^2 - G^2(\phi_{sf}, V) = E_{sb}^2 - G^2(\phi_{sb}, V) \quad (12)$$

where

$$G^2(\phi, v) = \frac{2qN_a V_T}{\epsilon_{Si}} \left[\left(e^{\frac{(\phi - 2\phi_F - V)}{V_T}} \right) - e^{\frac{(-2\phi_F - V)}{V_T}} \right] + e^{-\frac{\phi}{V_T}} + \frac{\phi}{V_T} - 1$$

As shown in [4], $\frac{qn}{E}$ in (11) can be expressed as

$$\frac{qn}{E} = - \left(\frac{\partial E}{\partial V} - \frac{1}{2E} \frac{d\alpha}{dV} \right) \epsilon_{Si} + \frac{qN_a}{E} e^{\frac{(-2\phi_F - V)}{V_T}} \quad (13)$$

Substituting (13) in (11) and following some mathematical derivations, the drain current of the asymmetric DG MOSFET can be expressed as

$$I_{ds} = \frac{\mu W \epsilon_{Si}}{L} + \frac{C_{oxf}}{\epsilon_{Si}} \left[V_{gf} \phi_{sf} - \frac{\phi_{sf}^2}{2} \right] + \frac{C_{oxb}}{\epsilon_{Si}} \left[V_{gb} \phi_{sb} - \frac{\phi_{sb}^2}{2} \right] + 2V_T \left[\frac{C_{oxf} \phi_{sf}}{\epsilon_{Si}} + \frac{C_{oxb} \phi_{sb}}{\epsilon_{Si}} \right] - \frac{2qN_a t_{Si}}{\epsilon_{Si}} \left[2V_T e^{\frac{(\phi_{sb})}{V_T}} + \phi_{sb} \right] \quad (14)$$

IV. RESULTS & DISCUSSIONS

Fig. 2 illustrates the variation of the surface potential with front gate voltage for different doping concentrations of 10^{14} cm^{-3} and $5 \times 10^{18} \text{ cm}^{-3}$ and different Silicon film thickness of 5 nm and 40 nm. It is clearly evident that for both lightly doped and heavily doped DG MOSFET, as the thickness of the channel increases from 5 nm to 40 nm, the back surface potential decreases considerably for a grounded back gate bias. For the lightly doped DG device, as the Silicon thickness increases from 5 nm to 40 nm, the front surface potential increases considerably that is more prominent in the subthreshold regime. This effect is nothing but the so called "Volume Inversion" effect that occurs in the lightly doped multigate MOS architectures. The effect of variation of back gate oxide thickness on the surface potentials are shown in fig. 3. It is evident that for heavily doped DG MOSFET, the front gate potential is less sensitive to back gate oxide thickness variation above 50nm. One the other hand, the back surface potential decreases considerably for decreasing back oxide thickness as obviously expected. The effect of back gate bias on the front and back surface potential is shown in fig. 4 along with the surface potential in a symmetric DG operation. As is expected, the back surface potential is more sensitive to the back gate bias compared to the front surface potential. The tied gate operation on the other hand shows increased potential that results in higher charge density in the channel.

The potential variation along the thickness of the channel is shown in fig. 5 for both symmetric and asymmetric operation. For the asymmetric operation, both back gate bias and back gate oxide thickness are changed. For the symmetric operation [4], the normalized distance along the thickness is

$2x/t_{Si}$ instead of x/t_{Si} as in our proposed model for asymmetric operation. The proposed model matches well with the simulation results that verify its accuracy.

Drain current variation with front gate voltage is shown in fig. 6 and fig. 7 with different back gate oxide thicknesses for a heavily doped and lightly doped DG MOSFET respectively. With a negatively biased back gate, as the back gate oxide thickness is increased from 2nm to 50nm, the drain current increases considerably especially in the weak inversion regime. The increase in drain current is more in case of the lightly doped channel due to the Volume Inversion phenomena. The model predicted $I_d - V_{ds}$ curve for heavily doped devices are shown in fig. 8. The back gate voltage is fixed at -0.2 V and a good agreement with the 2-D numerical simulation is observed.

V. CONCLUSION

We have proposed a surface potential based drain current model for a long channel asymmetric DG MOSFET that is valid for all range of channel doping concentrations. The predicted results are compared with device simulator Sentaurus TCAD and a good agreement is observed. Thus the surface potential based model can provide adequate insight into the physics of a generic four terminal long channel doped/ undoped asymmetric DG MOSFET and also provides a satisfactory device design guidelines.

REFERENCES

- [1] F. Balestra, S. Cristoloveanu, M. Benachir, J. Brini, and T. Elewa, "Double-gate silicon-on-insulator transistor with volume inversion: A new device with greatly enhanced performance," *IEEE Electron Device Lett.*, vol. EDL-8, pp.410, 1987
- [2] Y. X. Liu, M. Masahara, K. Ishii, T. Tsutsumi, T. Sekigawa, H. Takashima, H. Yamauchi, and E. Suzuki, "Flexible threshold voltage FinFETs with independent double gates and an ideal rectangular cross-section Si-Fin channel," *IEDM Tech. Dig.*, 2003, pp. 986-988.
- [3] Feng Liu, Jin He, Yue Fu, Jinhua Hu, Wei Bian, Yan Song, Xing Zhang, Member, and Mansun Chan, "Generic Carrier-Based Core Model for Undoped Four-Terminal Double-Gate MOSFETs Valid for Symmetric, Asymmetric, and Independent-Gate-Operation Modes", *IEEE Trans. Electron Devices*, vol. 55, no. 3, pp. 816-826, Oct. 2008.
- [4] Feng Liu, Jin He, Jian Zhang, Yu Chen, and Mansun Chan, "A Non-Charge-Sheet Analytic Model for Symmetric Double-Gate MOSFETs With Smooth Transition Between Partially and Fully Depleted Operation Modes", *IEEE Trans. Electron Devices*, vol. 55, no. 12, pp. 3494-3502, Oct. 2008.
- [5] C. T. Sah and H. C. Pao, "The effects of fixed bulk charge on the characteristics of metal-oxide-semiconductor transistors", *IEEE Trans. Electron Devices*, vol. ED-13, no. 4, pp. 393-409, Apr. 1966.

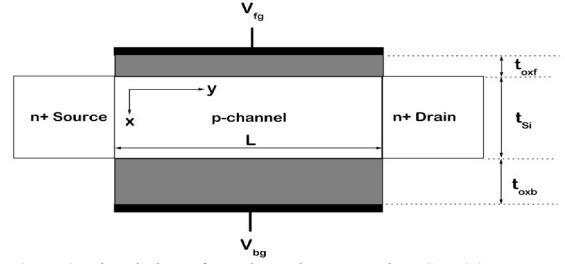


Fig. 1. Cross Sectional view of a n-channel asymmetric DG MOSFET

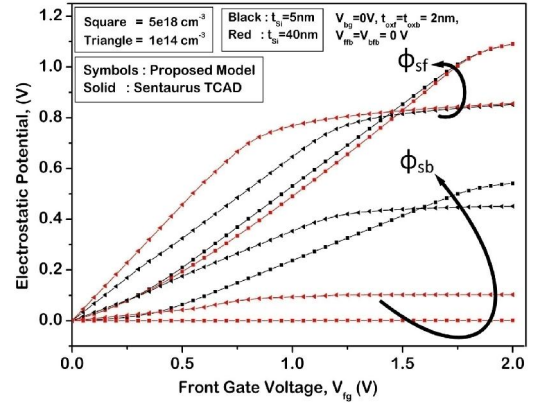


Fig. 2. Model predicted front and back surface potential vs. front gate voltage for different values of silicon channel thickness and channel doping concentrations

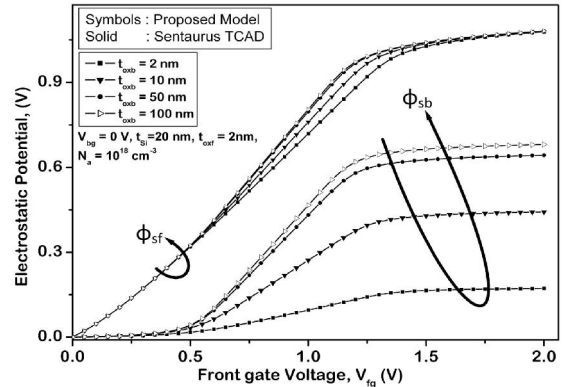


Fig. 3. Model predicted front and back surface potential vs. front gate voltage for different values of back gate oxide thickness at a grounded back gate voltage

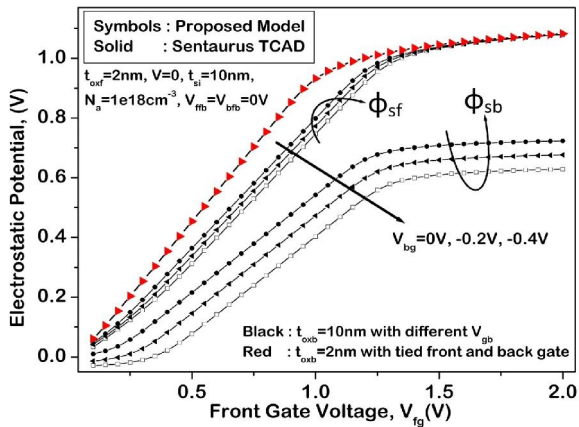


Fig. 4. Model predicted front and back surface potential vs. front gate voltage for different values of back gate voltage of -0.4V and 0V for a heavily doped asymmetric DG MOSFET

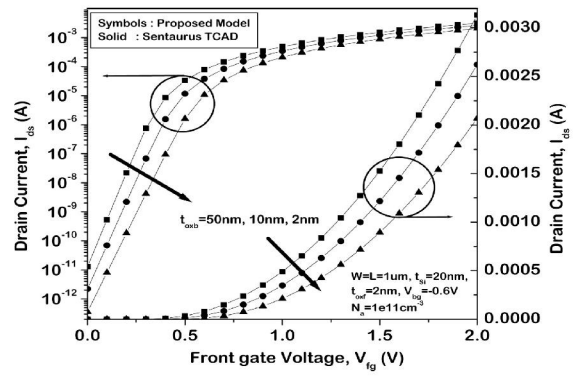


Fig. 7. Model predicted drain current vs. front gate voltage for different values of back gate oxide thickness in a lightly doped DG MOSFET

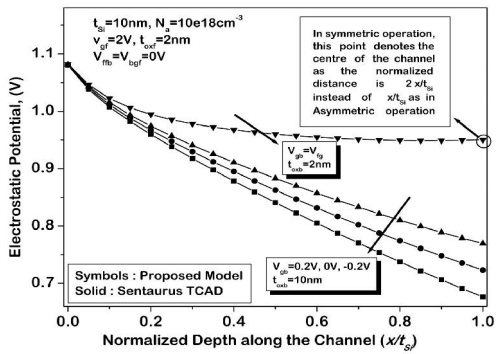


Fig. 5. Model predicted potential distribution along the channel thickness at the source end for different values of back gate voltage in a heavily doped asymmetric DG MOSFET

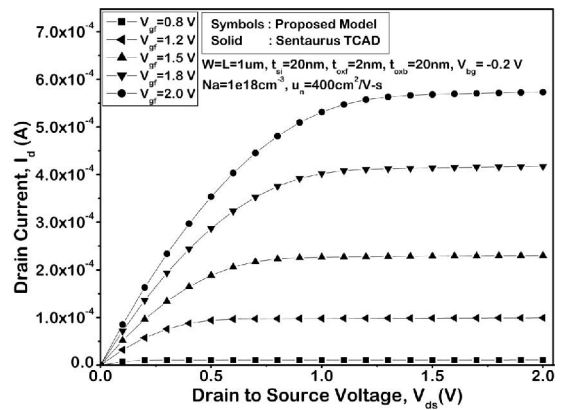


Fig. 8. Model predicted drain current vs. drain voltage for different values of front gate voltage in a heavily doped long channel DG MOSFET at a fixed back gate voltage of -0.2V

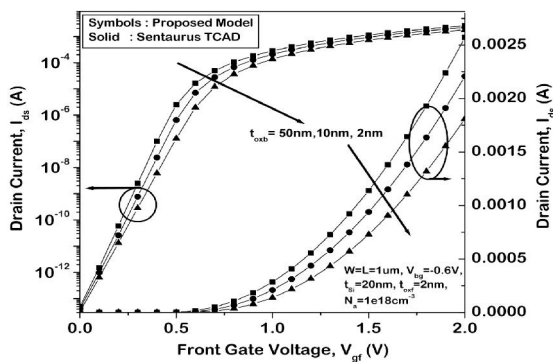


Fig. 6. Model predicted drain current vs. front gate voltage for different values of back gate oxide thickness in a heavily doped DG MOSFET